UNIVERSIDADE DE LISBOA

Faculdade de Ciências
Departamento de Química e Bioquímica

Effect of palmitoylated synaptic proteins and biologically relevant calcium concentrations on the compartmentalization of $PI(4,5)P_2$ in membrane model systems and in the plasma membrane of PC12 cells

Maria João Martins Sarmento

Mestrado em Bioquímica
(ramo Bioquímica Médica)

2011

UNIVERSIDADE DE LISBOA

Faculdade de Ciências
Departamento de Química e Bioquímica

Effect of palmitoylated synaptic proteins and biologically relevant calcium concentrations on the compartmentalization of $PI(4,5)P_2$ in membrane model systems and in the plasma membrane of PC12 cells

Maria João Martins Sarmento

Mestrado em Bioquímica
(ramo Bioquímica Médica)

Dissertação de Tese de Mestrado orientada por

Dr. Fábio Fernandes e co-orientada por Dra. Ana Coutinho

2011

Acknowledgments/ Agradecimentos

After concluding this work, I wish to acknowledge everyone that somehow helped and supported its realization.

In the first place, I want to thank to Professor José Manuel Gaspar Martinho for allowing me to execute this project in the Centro de Química-Física Molecular (CQFM) of the Instituto Superior Técnico (IST). I specially want to express my gratitude to Professor Manuel Prieto for receiving me in his group (Molecular Biophysics Group) and for all the support and willingness demonstrated. I also want to acknowledge Professor Joaquim M. S. Cabral for allowing me to perform all the cellular work at the Institute for Biotechnology and Bioengineering (IBB/ IST) and Dr. Catarina Madeira for all the technical support and useful help kindly provided.

My most thankful acknowledgment is for Dr. Fábio Fernandes, my supervisor in this work. I really want to thank all the support and dedication, for being available at all times and, above all, for the huge patience he had with me. Also, I want to direct a special word to Dr. Ana Coutinho that encouraged and supported me during all the year.

For the great work environment, I want to thank all the laboratory colleagues and friends. They were an exceptional help and supported me in all the possible ways. I particularly want to express my gratitude to Sandra Pinto for helping me with the cell biology studies.

Financial support from FCT must be acknowledged, for the concession of an investigator grant in the context of the project “Relationship between PI(4,5)P2 compartmentalization and palmitoylated synaptic proteins in membrane model systems and in the plasma membrane of neuron and non-neuron like cells.” (PTDC/QUI-BIQ/112067/2009).

To all my friends, I warmly want to express my sincere gratitude for supporting and encouraging me all the way along. Particularly, I want to thank Joana and Samuel for their help, not only this year but also in previous ones, for their kind support, their confidence in me, for their gigantic patience and most of all, for making laugh when I needed to. Also, I want to direct a really special word to Francisco, for putting up with me during difficult times, for his care and patience, for his encouragement and kind support. The simple presence of these 3 persons really meant something to me during this year.

Finalmente, e como não podia deixar de ser, quero agradecer todo o apoio da minha família. Aos meus pais, João e Aida, pelo apoio e confiança incondicionais que sempre demonstraram, pelo respeito por todas as minhas opções, por aturarem com o mau feitio nos piores momentos e com a parvoíce nos melhores, por tudo o que sempre fizeram, e continuam a fazer, por mim e por todo o amor: muito obrigado. Não tinha chegado até aqui sem eles. Para terminar, quero agradecer a uma pessoa muito especial que esteve ao meu lado desde que me lembro: o meu irmão Pedro. Obrigado por todo o apoio e compreensão, pelas gargalhadas frequentes e pela confiança incondicional.

Table of Contents

Abstract

Phosphatidylinositol 4,5-bisphosphate ($PI(4,5)P_2$) is a minor component of the plasma membrane of eukaryotic cells that is essential for several cellular mechanisms, including organization of the actin cytoskeleton, membrane trafficking, endocytosis and exocytosis. The regulation of these processes is thought to involve the local enrichment of $PI(4,5)P_2$ in the plasma membrane at particular timings.

In the first part of this work, we aimed to better characterize the mechanisms responsible for $PI(4,5)P_2$ clustering in the plasma membrane of neuronal-like (PC12) and non-neuronal (HEK293) cells. Using FRET microscopy carried out with PH-domains labelled with fluorescent proteins (PH-CFP and PG-YFP), we detected a highly clustered distribution of $PI(4,5)P_2$ in PC12 cells and some indication of clustering below the confocal resolution for HEK293 cells. Moreover, FRET efficiency decreased after inhibition of protein palmitoylation, emphasizing the importance of the interaction between palmitoylated proteins and $PI(4,5)P_2$ for its lateral membrane organization.

Additionally, since we were also interested in studying $PI(4,5)P_2$ distribution in giant unilamellar vesicles (GUVs), we optimized a GUV immobilization method based on the interaction of biotinylated lipids with an avidin-coated surface. Three different biotinylated lipids were studied: DOPE-Cap-biotin, DPPE-Cap-biotin and DPPE-biotin. Since $PI(4,5)P_2$ has been shown to partition into lipid rafts, studies with POPC:Chol:PSM (1:1:1) GUVs presenting a coexistence of liquid ordered/liquid disordered phases were performed. Our results showed that the immobilization conditions and the type of immobilizing lipid significantly influence the distribution of lipid domains within GUVs, potentially generating artefacts in lipid phase coexistence studies.

By imaging GUVs with a fluorescent analogue of $PI(4,5)P_2$, we observed a Ca^{2+} induced clustering of the fluorescent lipid at concentrations (>100 μM) known to occur in the proximity of calcium channels after synaptic stimulation. Then, $PI(4,5)P_2$ can potentially act as a lipidic calcium sensor, regulating not only local plasma membrane charge and curvature but also synaptic protein organization.

Keywords: $PI(4,5)P_2$ distribution, exocytosis, protein palmitoylation, calcium, GUV immobilization

Resumo

O 4,5-bisfostato de fosfatidilinositol ($PI(4,5)P_2$) é um componente minoritário do folheto externo da membrana plasmática das células eucariotas. Este lípido constitui cerca de 1% da quantidade total de fosfolípidos presentes na membrana, quantidade esta que é mantida em estado estacionário através de contínuas fosforilações e desfosforilações deste fosfoinositol.

O $PI(4,5)P_2$ está envolvido em diversos processos fisiológicos que são essenciais à manutenção celular. Por exemplo, é o precursor de 3 segundos mensageiros (1,4,5-trisfosfato de inositol (IP_3), diacilglicerol (DAG) e 3,4,5-trisfosfato de fosfatidilinositol ($PI(3,4,5)P_3$)) e funciona ainda ele próprio como segundo mensageiro, controlando a função de diversas proteínas de membrana e activando diversos enzimas, como os envolvidos no metabolismo dos fosfoinositóis. Por outro lado, existem na célula várias proteínas que apresentam na sua estrutura domínios com grande afinidade para moléculas de $PI(4,5)P_2$, como por exemplo os domínios homólogos da *pleckstrina* (domínios PH). As interacções destes domínios com o fosfoinositol desempenham um importante papel na regulação de diferentes processos a nível celular, como sejam a organização do citosqueleto de actina, o tráfego membranar, a endocitose e a exocitose.

Em neurónios, pensa-se que o $PI(4,5)P_2$ seja um factor chave na regulação da sinapse. A fusão de vesículas com a membrana plasmática é mediada por um conjunto de proteínas chamadas *soluble NSF (N-ethylmaleimide-sensitive factor) attachment protein receptors* (SNAREs) que partilham o mesmo motivo SNARE na sua estrutura. Em neurónios e células de tipo neuronal, o complexo SNARE responsável pela fusão é constituído por 3 proteínas SNARE, duas presentes na membrana plasmática (sintaxina-1 e a *synaptosomal-associated protein of 25 kDa* (SNAP-25)) e uma presente na membrana das vesículas (sinaptobrevina or *vesicle-associated membrane protein 2* (VAMP2)). Tanto a sintaxina como a sinaptobrevina apresentam um segmento transmembranar e, por isso, estão inseridas na membrana. Por outro lado, a SNAP-25, embora não tenha qualquer segmento transmembranar, está ancorada na membrana plasmática através de múltiplas palmitoilações. Em células PC12, tanto a sintaxina-1 como a SNAP-25 co-localizam-se parcialmente com microdomínios de $PI(4,5)P_2$.

Apesar da estrutura do $PI(4,5)P_2$ não favorecer a curvatura negativa da membrana que potencia a fusão, o seu enriquecimento nas zonas de ligação de

vesículas à membrana é essencial ao início da fusão dependente de cálcio. Adicionalmente, o $PI(4,5)P_2$ inibe a fusão de lipossomas mediada por SNAREs, inibição essa que pode ser ultrapassada através da inclusão da proteína CAPS (*Ca^{2+}-dependent activator protein for secretion*) nas vesículas. Este resultado sugere que o $PI(4,5)P_2$ regula a fusão de vesículas sinápticas inibindo-a directamente, ao mesmo tempo que recruta proteínas necessárias à transmissão mediada por SNAREs possivelmente através de uma mecanismo dependente da concentração de cálcio intracelular.

Neste projecto pretendia-se elucidar o papel da palmitoilação das proteínas e de diferentes concentrações de cálcio na distribuição do $PI(4,5)P_2$ na membrana plasmática. Para isso, foram seguidas duas estratégias distintas e complementares.

Na primeira parte deste trabalho estudou-se a distribuição de $PI(4,5)P_2$ na membrana plasmática de células neuronais (PC12) e não neuronais (HEK293). Para isso foram realizados estudos de microscopia confocal de fluorescência e FRET por imagem, recorrendo a construções de domínios PH ligados a proteínas fluorescentes (o dador PH-CFP e o aceitante PH-YFP) como sensores da densidade lateral de $PI(4,5)P_2$ nas membranas plasmáticas. Em células HEK293, embora não tenham sido observadas heterogeneidades na distribuição lateral do $PI(4,5)P_2$ na membrana acima da resolução confocal, as eficiências de FRET entre PH-CFP e PH-YFP eram quase independentes da concentração de aceitante. Desta forma, conclui-se que deverá existir uma organização das moléculas de $PI(4,5)P_2$ abaixo do nível de resolução do microscópio (< 250 nm). Quando as células HEK293 foram expostas ao inibidor de palmitoilação 2-bromo-palmitato (2BP), observou-se uma ligeira diminuição na eficiência de FRET, o que revela a importância da interacção do $PI(4,5)P_2$ com proteínas palmitoiladas na sua distribuição intracelular, mesmo em células não neuronais. No caso das células PC12 diferenciadas através da exposição (3 dias) ao factor de crescimento neural (NGF), foi possível observar a segregação de moléculas de $PI(4,5)P_2$ em agregados que apresentavam eficiência de FRET elevada. Contudo, os agregados não tinham todos a mesma densidade, sendo que os *clusters* com maior intensidade de fluorescência apresentavam menor eficiência de FRET. A fonte desta discrepância é desconhecida e deverá ser estudada em maior detalhe no futuro.

A influência da palmitoilação na localização da proteína SNAP-25 em células PC12 foi também estudada. Expondo as células PC12 diferenciadas a 2BP, foi possível observar a re-localização da SNAP-25-GFP da membrana para o citosol. Contudo, possivelmente devido à sua interacção com a sintaxina-1 na membrana

plasmática, só cerca de metade da proteína SNAP-25-GFP deixou de se ligar à membrana plasmática. No futuro, espera-se que esta ferramenta seja útil no estudo dos efeitos da palmitoilação da SNAP-25 na distribuição de $PI(4,5)P_2$ em células PC12.

Na segunda parte deste projecto, estudou-se a distribuição lateral de $PI(4,5)P_2$ na membrana de vesículas unilamelares gigantes (GUVs), na presença de diferentes concentrações de cálcio. Inicialmente, e com o intuito de obter dados de microscopia confocal de elevada qualidade, foi necessário optimizar um método de imobilização das vesículas durante o tempo de aquisição dos dados. O método escolhido tem por base a interacção de lípidos biotinilados com uma superfície revestida com avidina. Duas misturas lipídicas foram estudadas, POPC:Chol:PSM (1:1:1), que apresenta coexistência de fases líquido ordenado (lo)/líquido desordenado (ld), e DOPC:DPPC (1:1) que apresenta coexistência fases gel/fluido. Três lípidos biotinilados diferentes (DOPE-Cap-biotin, DPPE-Cap-biotin e DPPE-biotin) foram também utilizados. Note-se que sistemas modelo que apresentam coexistência de fases lo/ld têm grande relevância para estudos sobre a distribuição de $PI(4,5)P_2$ na membrana plasmática, uma vez que já foi observada a partição de $PI(4,5)P_2$ para jangadas lipídicas ricas em colesterol e esfingomielina.

Através da utilização de microscopia confocal de fluorescência foi possível estudar a influência do método de imobilização na forma das vesículas gigantes e na distribuição dos domínios lipídicos. Quando se utilizaram baixas concentrações de lípido biotinilado, a forma das GUVs não era afectada significativamente. Para concentrações mais elevadas de lípido biotinilado, a taxa de colapso das vesículas aumentava significativamente e as vesículas apresentavam frequentemente deformações em relação à sua forma esférica.

A interacção das vesículas com a superfície sólida da câmara, mesmo na ausência de lípidos biotinilados e de avidina, induzia uma redistribuição de domínios lipídicos, havendo uma preferência de interacção das vesículas gigantes com a superfície através da fase mais organizada (fase gel ou lo). Quanto aos lípidos biotinilados estudados, estes apresentavam claramente uma preferência para diferentes fases lipídicas dependente da sua estrutura química (tal como seria de esperar), o que também influencia a distribuição lateral dos domínios lipídicos. Foi também desenvolvido um método para quantificar a partição de lípidos biotinilados entre 2 fases lipídicas coexistentes, cuja aplicação do método ao lípido DOPE-Cap-biotina permitiu a recuperação de um coeficiente de partição líquido ordernado/líquido

disordenado de 0,26. Desta forma, concluiu-se que os estudos de separação de fases em GUVs que fazem uso da popular estratégia de medir as áreas de cada fase apenas no hemisfério superior da vesícula (mais afastado da lamela), estão susceptíveis a artefactos gerados pelo tipo de lípido imobilizador usado ou pela interacção da própria vesícula com a superfície imobilizadora. Conclui-se então que para minimizar estes artefactos nestes estudos, será útil estudar cada vesícula gigante na sua totalidade. Adicionalmente, uma vez que o lípido biotinilado que induziu menores diferenças entre a composição de cada hemisfério foi o DPPE-biotina, deverá ser o fosfolípido preferencialmente utilizado em estudos de GUVs imobilizados que apresentem coexistência de fases lo/ld.

Finalmente, é conhecido de estudos anteriores que concentrações elevadas de Ca^{2+} (1 mM) afectam a distribuição lateral do $PI(4,5)P_2$. Contudo, o efeito de concentrações mais fisiológicas deste catião (100 nM a 100 μM) é ainda desconhecido. Actualmente, considera-se que após um estímulo, a concentração de cálcio nas sinapses na vizinhança imediata dos canais de cálcio activados pode aumentar até aos 100 μM, a partir de um estado basal de 100 nM. Neste trabalho, estudámos o efeito de concentrações fisiológicas de cálcio na distribuição de uma sonda fluorescente análoga de $PI(4,5)P_2$ (TopFluor-$PI(4,5)P_2$). Através do estudo das propriedades de emissão de fluorescência da sonda em membranas fluidas, foi possível observar que a baixas concentrações (<1%), a sonda aparentava difundir-se livremente na membrana, provavelmente sob a forma monomérica. A maiores concentrações do análogo fluorescente, foi detectada a formação de complexos de TopFluor-$PI(4,5)P_2$ na membrana, através da realização de um estudo de *self-quenching* de fluorescência. Contudo, estes complexos dever-se-ão à presença do fluoróforo TopFluor no fosfolípido derivatizado, uma vez que não foram observados com outro análogo fluorescente de $PI(4,5)P_2$. Desta forma, para os estudos com o cálcio, incorporaram-se baixas quantidades (razão molar 1:500) de TopFluor-$PI(4,5)P_2$ nas GUVs para garantir que estávamos a observar unicamente interacções mediadas pelo grupo inositol. Através das imagens de microscopia confocal, foi verificada a formação de grandes agregados de $PI(4,5)P_2$ na presença de 100 μM e 1 mM de cálcio.

Estes resultados são importantes para o estudo da função do $PI(4,5)P_2$, especialmente nos mecanismos de exocitose. Após o estímulo sináptico, a entrada de cálcio deverá levar a uma reorganização massiva da distribuição do $PI(4,5)P_2$. Este fenómeno terá o potencial de não só alterar as propriedades de carga e curvatura locais da membrana plasmática nas zonas activas de sinapses, como de modificar a

distribuição e actividade das proteínas responsáveis pela maquinaria sináptica. O $PI(4,5)P_2$ poderá ser, desta forma, um sensor lipídico de cálcio, permitindo à célula um nível adicional de regulação da actividade sináptica.

Abbreviations

2BP, 2-bromopalmitate

A431 cells, human epithelial carcinoma cells

AF594-WGA, alexa fluor 594-wheat germ agglutinin

ANTH domain, AP180 N-terminal homology domain

AP, adaptor proteins

Arp2/3, actin-related protein 2/3

BFP, blue fluorescent protein

CAPS, Ca^{2+}-dependent activator protein for secretion

CFP, cyan fluorescent protein

Chol, cholesterol

DAG, diacylglycerol

DHHC motif, aspartate-histidine-histidine-cystein motif

DMEM, Dulbecco's modified Eagle's medium

DOPC, 1,2-dioleoyl-*sn*-glycero-3-phosphocholine

DOPE-Cap-biotin, 1,2-dioleoyl-*sn*-glycero-3-phosphoethanolamine-*N*-(cap biotinyl)

DPPC, 1,2-dipalmitoyl- *sn*-glycero-3-phosphocholine

DPPE-biotin, 1,2-dipalmitoyl-*sn*-glycero-3-phosphoethanolamine-*N*-(biotinyl)

DPPE-Cap-biotin, 1,2-dipalmitoyl-*sn*-glycero-3-phosphoethanolamine-*N*-(cap biotinyl)

ENTH domain, epsin *N*-terminal homology domain

ERM proteins, ezrin/radixin/moesin proteins

FBS, fetal calf serum

FCS, fluorescence correlation spectroscopy

FERM domain, band 4.1-ezrin-radixin-moesin domain

FITC, fluorescein isothiocyanate

FLIM, fluorescence lifetime imaging microscopy

FRET, Förster resonance energy transfer

GAP-23, growth associated protein of 43 kDa

GFP, green fluorescent protein

GUV, giant unilamellar vesicle

HEK293, human embryonic kidney 293

IP_3, inositol trisphosphate

IPP 5-Ptase, inositol polyphosphate 5-phosphatase

IRF, instrument response function

ld, liquid disordered

LDCV, large dense core vesicle

lo, liquid ordered

LUV, large unilamellar vesicle

MARCKS, myristyolated alanine-rich C kinase substrate

NBD-DPPE, 1,2-dipalmitoyl-*sn*-glycero-3-phosphoethanolamine-N-(7-nitro-2-1,3-benzoxa-diazol-4-yl)

NGF, nerve growth factor

PA, phosphatidic acid

PAT, palmitoyl transferase

PBS, phosphate buffered saline

PC12 cell, adrenal pheochromocytoma cell

PH domain, pleckstrin homology domain

$PI(3,4,5)P_3$, phosphatidylinositol 3,4,5-trisphosphate

PI(4)P, phosphatidylinositol 4-monophosphate

PI(4,5)P_2 4-Ptase, phosphatidylinositol 4,5-bisphosphate 4-phosphatases

PI(4,5)P_2, phosphatidylinositol 4,5-bisphosphate

PI, phosphoinosite

PI3KI, type I phosphatidylinositol 3-kinase

PI4K, phosphatidylinositol-4-monophosphate kinases

PIKfyve, phosphatidylinositol-3-phosphate 5-kinase

PIP4KII, type II phosphatidylinositol-5-phosphate 4-kinase

PIP5KI, type I phosphatidylinositol-4-phosphate 5-kinase

PKC, protein kinase C

PLC, phospholipase C

PLD, phospholipase D

POPC, palmitoyl-2-oleoyl-*sn*-glycero-3-phosphocholine

PSM, *N*-palmitoyl-*D-erythro*-sphingosylphosphorylcholine

PTEN, phosphatase and tensin homologue on chromosome 10

PX domain, phox homology domain

Rho-DOPE, 1,2-dioleoyl-*sn*-glycero-3-phosphoethanolamine-*N*-(lissamine rhodamine B sulfonyl)

ROI, region of interest

SBT, spectral bleedthrough

SLB, supported lipid bilayer

SNAP-25, synaptosomal-associated protein of 25 kDa

SNARE, NSF (N-ethylmaleimide-sensitive factor) attachment protein receptor

TCSPC, time-correlated single photon counting

TCSPT, time-correlated single-photon timing

TMR, transmembrane region

TopFluor-PI(4,5)P_2, 1-oleoyl-2-{6-[4-(dipyrromethene boron difluoride) butanoyl] amino} hexanoyl-*sn*-glycero-3-phosphoinositol-4,5-bisphosphate

t-PnA, *trans*-parinaric acid

t-SNARE, target membrane SNARE

VAMP2, vesicle-associated membrane protein 2 (or synaptobrevin)

v-SNARE, vesicle membrane SNARE

WASP, Wiskott–Aldrich syndrome protein

YFP, yellow fluorescent protein

1. Introduction

In the 1950s, Hokin and co-workers discovered that pancreatic secretion upon cell stimulation was linked to the phosphorylation of plasma membrane lipids (Hokin and Hokin, 1953). Five years later, they found that acetylcholinergic stimulation of cortical sympathetic ganglions also leads to this kind of lipid modification, particularly on phosphoinositides (PIs) and phosphatidic acid (PA) (Hokin and Hokin, 1958). These discoveries quickly drew in the interest of the scientific community around the PI family of phospholipids, since it became clear that PIs could play a central role in the regulation of membrane trafficking processes.

In the past decades, an enormous quantity of studies focused on PIs and their functions in cells (Haucke, 2005;Dumas et al., 2010). One of the most studied PI is phosphatidylinositol 4,5-bisphosphate ($PI(4,5)P_2$). This lipid has been associated to a great variety of vital processes in cells, and is a good example of PIs functional multiplicity and biological relevance.

1.1. Phosphatidylinositol 4,5-bisphosphate

1.1.1 Structural characteristics

The structure of the most common $PI(4,5)P_2$ form present in mammalian cell membranes is presented in figure 1.

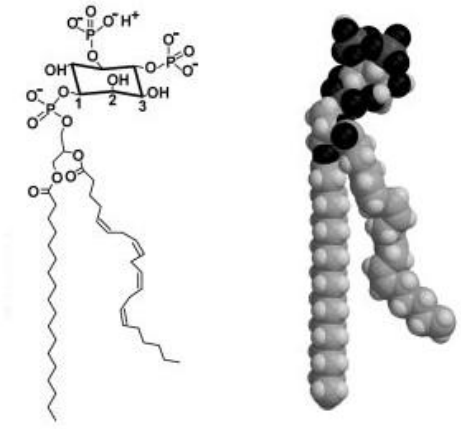

Figure 1. Predominant structure of $PI(4,5)P_2$ in mammalian cell membranes. Stearic acid is found at the *sn*1 position and arachidonic acid is found at *sn*2. Adapted from (McLaughlin et al., 2002).

From figure 1, we can see that $PI(4,5)P_2$ has a large head group and typically one highly unsaturated carbon chain. These two characteristics are expected to naturally favour the lipid localization to less rigidified areas of the membrane (McLaughlin et al., 2002).

Another important property is that the net charge of $PI(4,5)P_2$ can be altered by numerous factors, such as pH, ionic force or lipid-protein interactions. For example, at pH 7.0, the phosphates in the 4 and 5 positions, due to their *pK* values, should be protonated and unprotonated, respectively (van Paridon et al., 1986). Although we would expect a net charge of -4 at pH 7.0, at high ionic strenghts it is -3, as a result of the interaction of the lipid with cations in solution (Toner et al., 1988) or proteins (Wang et al., 2001). Thus, depending on the local environment, $PI(4,5)P_2$ can exhibit a net charge of -3, -4 or -5 (McLaughlin et al., 2002).

1.1.2 Metabolism

$PI(4,5)P_2$ is a minor component of the inner leaflet of the plasma membrane (Kwiatkowska, 2010). It constitutes around 1% of the total membrane phospholipids (Ferrell and Huestis, 1984). The total quantity of this PI in the plasma membrane remains at a steady-state as a result of continuous and sequential phosphorylation and dephosphorylation (figure 2).

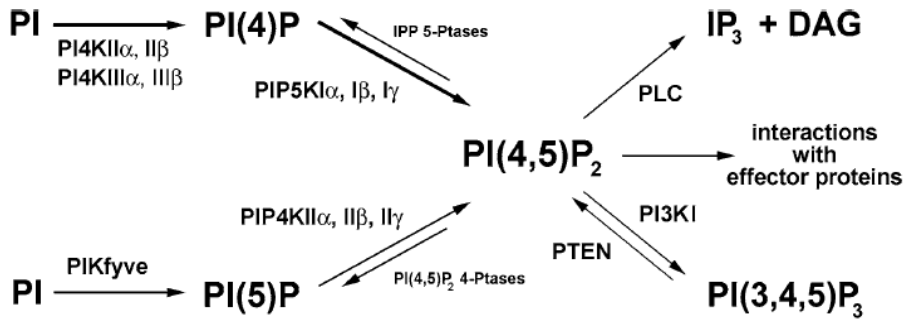

Figure 2. General eukaryotic metabolism of $PI(4,5)P_2$. Adapted from (Kwiatkowska, 2010).

As shown in figure 2, eukariotic cells have three pathways for $PI(4,5)P_2$ synthesis: two phosphorylations, catalyzed by type I phosphatidylinositol-4-phosphate 5-kinase

(PIP5KI) and type II phosphatidylinositol-5-phosphate 4-kinase (PIP4KII), and a dephosphorylation catalyzed by phosphatase and tensin homologue on chromosome 10 (PTEN). However, they do not equally contribute to $PI(4,5)P_2$ concentration. In fact, the major route for its synthesis is the phosphorylation of phosphatidylinositol 4-monophosphate (PI(4)P) by the PIP5KI (Toker, 1998), since the substrate is present in the plasma membrane in larger quantities (Kwiatkowska, 2010).

The balance between synthesis and degradation is maintained by the hydrolysis catalyzed by phospholipase C (PLC) and the type I phosphatidylinositol 3-kinase (PI3KI)-driven phosphorylation, besides the contribution of different phosphatases (Cockcroft and De Matteis, 2001). Along with the control of $PI(4,5)P_2$ levels, these two reactions generate three important second messengers, inositol triphosphate (IP_3), diacylglycerol (DAG) and phosphatidylinositol 3,4,5-trisphosphate ($PI(3,4,5)P_3$) (Berridge and Irvine, 1984).

The cellular location of all these reactions depends on the location of the correspondent enzymes. The great majority of these processes occur in the cytosolic face of the plasma membrane and are tightly regulated. At a smaller scale, some of them can take place along the secretory pathway, mostly in the Golgi apparatus (Payrastre et al., 2001).

1.1.3 Cellular functions

$PI(4,5)P_2$ is implicated in many physiological processes that are crucial to the cells. As already mentioned, it is the precursor of three second messengers, IP_3, DAG and $PI(3,4,5)P_3$, each of them with distinct and important functions. IP_3 stimulates the release of Ca^{2+} stored in the endoplasmic reticulum (Berridge, 2009), whereas DAG is related with membrane anchoring and activation of the protein kinase C (PKC) (Hurley and Misra, 2000). $PI(3,4,5)P_3$ regulates the localization and function of several proteins, including the phagocytosis-implicated protein ARF6 (Czech, 2000).

On the other hand, $PI(4,5)P_2$ can act as a second messenger itself, affecting a great variety of processes. It can control the activity of integral membrane proteins, such as transporters and ion channels (Kwiatkowska, 2010), and activate several enzymes including the ones involved in the metabolism of phosphoinositides. For example, the voltage-gated K^+ channel (Zhang et al., 2003) and the phospholipase D

(PLD), which generates the phosphatidic acid necessary to the PIP5PK activation (Liscovitch et al., 1994), are both PI(4,5)P_2-activated.

Notwithstanding, much of the PI(4,5)P_2 functional multiplicity arises from its capacity of binding several protein domains. In other words, it functions as an anchor that targets proteins to the plasma membrane, controlling their activity in time and space. Over the past twenty years, several distinct domains were shown to bind PI(4,5)P_2: the pleckstrin homology (PH) domain of PLCδ_1, the band 4.1-ezrin-radixin-moesin (FERM), the AP180 N-terminal homology (ANTH), the epsin N-terminal homology (ENTH) and the phox homology (PX) domains (Lemmon, 2003). Beyond these, electrostatic interactions can also occur between the PI(4,5)P_2 negative head-group and the unstructured polybasic region presented in some proteins (Lemmon, 2003). Together, these lipid-protein interactions play a key role in living cells, regulating the actin cytoskeleton attachment and reorganization, membrane trafficking, endocytosis and exocytosis (McLaughlin et al., 2002).

It was already shown that a decrease in PI(4,5)P_2 levels result in a depolymerization and release of the actin cytoskeleton from the membrane (Raucher et al., 2000). As show in the figure below, the remodelling and maintenance of the cytoskeleton is regulated by the presence of this phosphoinositide. In fact, it can for example bind the Wiskott–Aldrich syndrome protein (WASP) that, through the activation of the actin-related protein 2/3 (Arp2/3) complex, is responsible for the remodeling and branching of the actin filaments (Sechi and Wehland, 2000).

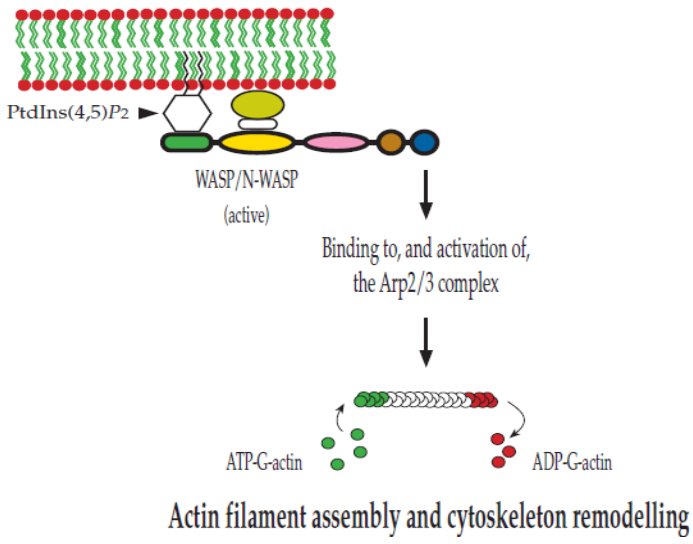

Figure 3. PI(4,5)P_2-WASP interaction and its effect on actin polymerization. Adapted from (Sechi and Wehland, 2000).

A great number of other proteins interact directly with PI(4,5)P_2 to regulate the cellular cytoskeleton. Ezrin/radixin/moesin (ERM) proteins, vinculin and talin also anchor the actin filaments to the membrane (Logan and Mandato, 2006), while pleckstrin and the myristyolated alanine-rich C kinase substrate (MARCKS) is related to lamellipodia and membrane ruffles formation (Honda et al., 1999). In addition, profilin, cofilin, gelsolin, destrin, α-actinin and filamin take action in actin capping and severing.

As pointed out before, PI(4,5)P_2 is also associated to membrane trafficking. Its functions are not well clarified, but it has already been related to several steps of clathrin-mediated endocytosis and exocytosis. In the first case, PI(4,5)P_2 was shown to bind several endocytic proteins along the process. Initially, it interacts with clathrin adaptor proteins such as AP-1, AP-2 and AP180, during the recruitment of the clathrin coat (Ford et al., 2001). Latter in the mechanism, it was shown to be related with the fission of endocytic pits and clathrin uncoating, through the GTPase dynamin (Jost et al., 1998) and the phosphatase synaptojanin-1 (Cremona et al., 1999), respectively.

As well as in endocytosis, PI(4,5)P_2 plays different roles throughout exocytosis. It interacts with specific proteins during each phase of the process: vesicle docking, priming and fusion (Lang et al., 2008). Although PI(4,5)P_2 regulation of exocytosis is poorly understood, it is already known that, for example, PI(4,5)P_2 binds synaptotagmin, a protein associated with the Ca^{2+}-triggered exocytosis, rabphilin3, the effector of rab3 proteins responsible for controlling the SNARE complex formation (Chung et al., 1998) and the SNARE protein syntaxin-1, as is described further down in this work (Aoyagi et al., 2005).

1.1.4 Imaging PI(4,5)P_2 in vivo – Pleckstrin Homology (PH) domains

Pleckstrin homology domains represent the major family of PI binding domains, with more than 250 known members. They present around 120 aminoacid residues and were first described in 1993 in pleckstrin, the major substrate of PKC in platelets (Halet, 2005).

Despite the extremely low sequence homology (7-23%), PH domains exhibit a much conserved tertiary structure based on seven β-strands that shape two orthogonal β-sheets and one C-terminal α-helix, forming an electrostatically polarized binding pocket. The binding to phosphoinositides involves basic residues located in the β-

strands and inter-strands loops, establishing multiple hydrogen bonds with the PIs phosphate groups. The great variability in the length and sequence of the loops is responsible for the diversity of specificity and affinity of PIs recognition by PH domains (Lemmon and Ferguson, 2000;Halet, 2005)

To report PI(4,5)P_2 distribution *in vivo*, the most commonly used domain is the already mentioned PH domain of PLCδ_1 (PLCδ_1-PH, see figure 4) fused with a fluorescent protein (Halet, 2005). PLCδ_1-PH was shown to be necessary and sufficient for the interaction of PLC with the plasma membrane, i.e., it represents a non-catalytic binding site that recruits the enzyme to PI(4,5)P_2-enriched membrane regions (Lemmon et al., 1996). However, since it binds PI(4,5)P_2 through its IP_3 headgroup, PLCδ_1-PH shows 10 to 20-fold higher affinity to IP_3 than to PI(4,5)P_2 (Gamper and Shapiro, 2007). Notwithstanding, due mostly to PI(4,5)P_2 higher concentration in cells, in most cell lines PLCδ_1-PH-GFP is a good PI(4,5)P_2 sensor, better than an IP_3 reporter (Balla, 2007).

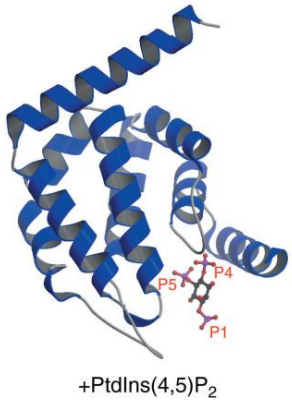

Figure 4. PLCδ_1-PH as the binding pocket for PI(4,5)P_2 molecules. Adapted from (Lemmon, 2003).

In addition, the interaction between PLCδ_1-PH-GFP and PI(4,5)P_2 was observed to be highly dynamic. In this way, PI(4,5)P_2 is believed to remain accessible to endogenous proteins, non-interfering significantly with the physiology of the cell if the protein is expressed at a reasonable level (Halet, 2005).

1.2. Lateral organization of $PI(4,5)P_2$ *in vitro*

The most intriguing question about $PI(4,5)P_2$ is how can it regulate so many mechanisms having such a low and constant concentration in cells. In fact, $PI(4,5)P_2$ regulation of biological processes generally seems to depend on localized membrane variations of its concentration. Here, the lateral organization of $PI(4,5)P_2$ in fluid membranes is discussed, based on studies carried out with membrane model systems.

1.2.1 Membrane model systems

In living cells there are many factors that contribute to modify the biophysical properties of membranes and their interaction with proteins. In this context, it is very helpful to use simplified artificial models of cell membranes, whose conditions can be closely controlled. Despite all the variants that can be altered or introduced depending on the experiment, there are two main types of model systems typically used to mimic cellular membranes in microscopy studies: giant unilamellar vesicles (GUVs) and supported lipid bilayers (SLBs), as shown in figure 5.

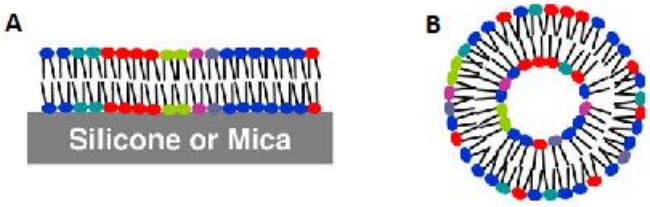

Figure 5. Model systems used to mimic cellular membranes. A) supported lipid bilayer; B) GUV (images are not represented to scale; GUV diameter is typically around 10-100 μm). Adapted from (Peetla et al., 2009).

In the supported lipid bilayer model, the membrane lays down on a solid surface, which is usually a polar substrate such as silicon, mica or even glass (Peetla et al., 2009). The lipid molecules are not in direct contact with the surface, since they have between them an aqueous sheet with a length of 1-2 nm that ensures the lateral and rotational motility of the lipids. However, it remains some friction with the solid surface, and lipid diffusion in SLBs is more than two times slower than in vesicles. Moreover,

the water layer is not always sufficiently thick to accommodate the big extramembrane domains of transmembrane proteins, what can result in movement restrictions, immobilization or even denaturation of the protein (Loose and Schwille, 2009). For this reason, hydrated polymer cushions (Wagner and Tamm, 2000) or hydrogels (Sackmann, 1996) are often used between the SLB and the substrate, adding complexity to the system. Nevertheless, the use of a solid surface guarantees that the membrane maintains its well-defined geometry and does not deform even in case of protein binding. Other advantages are facilitated microscopic observation and the possibility of performing real time measurements of lipid dynamics with single molecule techniques (Loose and Schwille, 2009).

GUVs are lipid vesicles with an internal aqueous compartment that can float freely in aqueous solutions (Peetla et al., 2009). As a result of their cell-like size (10-100 µm) and spherical closed bilayer geometry, they are the most biomimetic membrane model in use. In addition, they do not present the lipid movement restrictions observed in SLBs (Kahya, 2010). However, contrary to SLBs, they can suffer deformations and their movement increases the difficulty of performing accurate microscopic measurements.

To overcome the disadvantages of both models it was necessary to combine the structural ideal characteristics of GUVs with the technical approaches that could easily be performed in SLBs. The most common way to reach this purpose is to immobilize GUVs in a solid surface, e.g. through DNA hybridization or taking advantage of the biotin-avidin/streptavidin interaction properties (Chan and Boxer, 2007).

1.2.2 PI(4,5)P_2 clustering

As pointed out before, the total cellular PI(4,5)P_2 concentration does not change much over time. On the other hand, the cellular levels of PI(4,5)P_2 ligands are greater than the PI(4,5)P_2 concentration itself (Levental et al., 2009). Notwithstanding, it regulates several important signaling pathways in time and space through local variations of its concentration. In other words, the regulation of these processes must be achieved by localized enrichment of PI(4,5)P_2 in the plasma membrane at particular sites and timings. Here, we will describe these local deviations of homogeneity in membrane composition as clusters.

One of the mechanisms suggested to explain $PI(4,5)P_2$ membrane clustering is the formation of hydrogen bonds between the head-groups of $PI(4,5)P_2$ molecules. This implies a spontaneous aggregation of the molecules dependent of pH, which should occur regardless the membrane composition (Redfern and Gericke, 2005). However, it was clearly demonstrated that $PI(4,5)P_2$ does not form domains in fluid-phase large unilamellar vesicles (LUVs) composed of 1-palmitoyl-2-oleoyl-*sn*-glycero-3-phosphocholine (POPC) in a pH range from 4,8 to 8,4 (Fernandes et al., 2006). This means that, although hydrogen bonds could thermodynamically favor the clustering, they are not the major factor leading to $PI(4,5)P_2$ localized enrichment.

Nevertheless, clustering of $PI(4,5)P_2$ molecules was already observed in human epithelial carcinoma cells (A431). $PI(4,5)P_2$ seemed to partition to cholesterol/sphingomyelin-enriched membrane rafts (Pike and Casey, 1996) and, in the presence of a cholesterol removing agent (methyl-β-cyclodextrin), $PI(4,5)P_2$ compartmentalization was abolished (Pike and Miller, 1998). In this way, cholesterol appears to play a crucial role in PI domains formation. On the other hand, the *sn*-2 acyl chain of $PI(4,5)P_2$ is highly polyunsaturated and is not expected to partition spontaneously to lipid rafts. In fact, in lipid monolayers it is segregated from cholesterol-enriched rafts, partitioning preferentially to the fluid phase (Levental et al., 2009). This suggests that in living cells there must be other underlying mechanisms driving $PI(4,5)P_2$ molecules to cluster in more ordered areas of the membrane.

One hypothesis is the localized synthesis of $PI(4,5)P_2$ that could increase its concentration in microscopic regions of the plasma membrane (Payrastre et al., 2001). This is supported by the discovery of the co-localization of phosphatidylinositol-4-monophosphate kinases (PI4K) with rafts (Botelho et al., 2000). However, due to lateral diffusion, the molecules are expected to diffuse away much faster than they can be produced (McLaughlin et al., 2002). Once more, this process alone should not be able to drive localized enrichment of $PI(4,5)P_2$.

Another factor to be considered is the presence of several proteins with $PI(4,5)P_2$ affinity, which are able to electrostatically sequester $PI(4,5)P_2$ (Laux et al., 2000) even in model systems (Rauch et al., 2002). That is the case of the MARCKS protein or the growth associated protein of 43 kDa (GAP-23). To be able to concentrate the lipid in a membrane domain, proteins have to be themselves concentrated in the domain and show high affinity to $PI(4,5)P_2$. When these proteins bind $PI(4,5)P_2$ in a membrane domain, they promote a decrease in its local diffusion coefficient up to 10-fold, causing the lipid to accumulate till ten times more than the free molecules (McLaughlin et al.,

2002). Combining the protein effect with the localized synthesis, it is possible to efficiently compartmentalize PI(4,5)P_2 in membranes, allowing cells to control several processes in a fast way, without changing PI(4,5)P_2 global concentration.

1.3. Neuronal exocytosis

Exocytosis is the process by which an intracellular vesicle merges with the plasma membrane. It occurs in eukaryotic cells and plays two main functions: the addition of membrane components to the plasma membrane and the release of the vesicle contents to the extracellular space.

There are two main types of exocytosis. Constitutive exocytosis occurs in every eukaryotic cell in the absence of any stimulus. Its principal function is to maintain the lipid and protein levels in the plasma membrane and extracellular environment. The second type is the regulated exocytosis and is limited to cells with specific functions, only taking place in response to a stimulus (Lin and Scheller, 2000).

Ca^{2+}-triggered exocytosis, e.g. neurotransmitter release in neurons (figure 6), is a good example of regulated exocytosis.

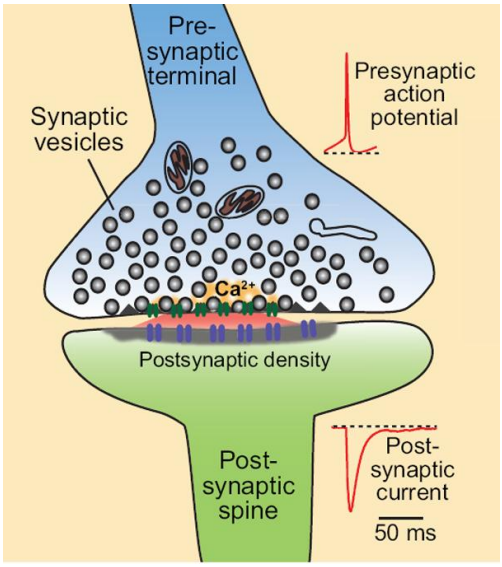

Figure 6. Schematic representation of synapse in neuronal cells. Adapted from (Pang and Sudhof, 2010).

Cells spend a lot of energy to keep the intracellular calcium levels at a low range (~100 nM, while outside the cells is 2 mM), pumping Ca^{2+} ions to internal storage organelles as the endoplasmic reticulum or to the extracellular space. A low cytosolic Ca^{2+} concentration is essential for neurons as this allows for a fast and effective response to the influx of Ca^{2+} after stimulation (Clapham, 1995;Greer and Greenberg, 2008).

In pre-synaptic terminals, the process of synaptic vesicle fusion begins with a transient event in which the plasma membrane quickly depolarizes (membrane potential is changed from -70 mV to +40 mV), followed by an also fast repolarization – the action potential. Membrane depolarization leads to calcium influx by opening of voltage-gated Ca^{2+} channels, increasing the local intracellular concentration of this ion, which in turn results in a downstream synchronized vesicle fusion with the plasma membrane and the consequent release of neurotransmitters (Clapham, 1995;Neher and Sakaba, 2008).

1.3.1 Studying synapses in vivo – PC12 cells

Adrenal pheochromocytoma cells (PC12) were first cloned from a solid pheochromocytoma tumor of a white rat (Greene and Tischler, 1976). They are small (6-14 µm diameter), round and present a doubling time of 48-96 hours (Fujita et al., 1989). PC12 is the most commonly used cell line to study regulated exocytosis, since they can be easily cultured, pharmacologically manipulated, and acquire a sympathetic ganglion neuron-like phenotype after exposure to the nerve growth factor (NGF) (Westerink and Ewing, 2008). When treated with NGF, PC12 cells stop division and start to extend ramifications called neurites, as shown in figure 7. Removal of NGF leads to degeneration of neurites and re-establishment of cell cycle and division, indicating the reversible character of this differentiation.

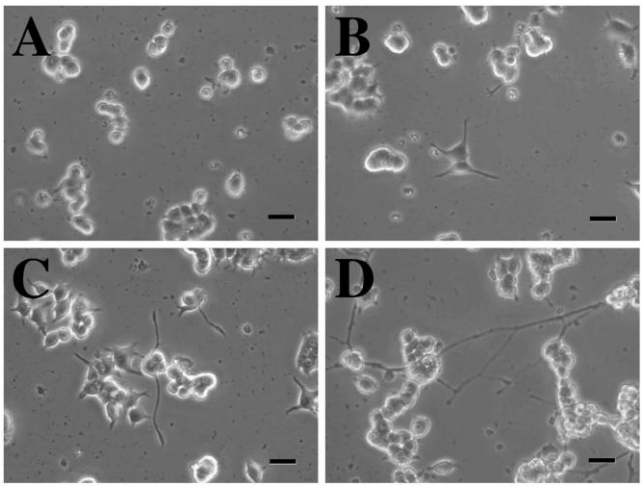

Figure 7. Differentiation of PC12 cells after exposure to NGF during A) 0h, B) 24h, C) 48h and D) 96h. Adapted from (Vancha et al., 2004).

PC12 cells actually present some other interesting and useful characteristics beyond the neuronal morphology. They synthesize and store dopamine and sometimes noradrenalin that are released upon Ca^{2+}-dependent depolarization. They present the protein machinery responsible for the synapse in neurons and also develop electrical excitability, closely mimicking the behaviour of neurons (Westerink and Ewing, 2008). These features establish undifferentiated and differentiated PC12 cells as good models to study neuronal chemical transmission and other synapse-related processes.

1.3.2 Synaptic machinery – the SNARE complex

Given that for fusion of two distinct membranes to occur a high energy barrier must be overcomed, it soon became clear that this process do not occur spontaneously and that there must be other factors facilitating the process. On the other hand, concerning synaptic exocytosis, the high degree of specificity suggests the intervention of several proteins controlling fusion. In fact, clostridial toxins were shown to strongly inhibit neurotransmitters release and the interest in their substrates has been increasing over the past 20 years. These are called soluble NSF (N-ethylmaleimide-sensitive factor) attachment protein receptors (SNAREs) and play a crucial role in exocytosis (Schiavo et al., 1992).

SNAREs are a superfamily of small membrane proteins that share a segment in the cytosolic domain with 60-70 aminoacid residues, called SNARE motif. In neurons

and neuron-like cells, three SNARE proteins constitute the basic machinery catalyzing the fusion of synaptic vesicles with the plasma membrane: syntaxin-1 and the synaptosomal-associated protein of 25 kDa (SNAP-25) present in the target/plasma membrane (also called *t*-SNAREs) and synaptobrevin or vesicle-associated membrane protein 2 (VAMP2) in the vesicle membrane (*v*-SNARE) (Halemani et al., 2010).

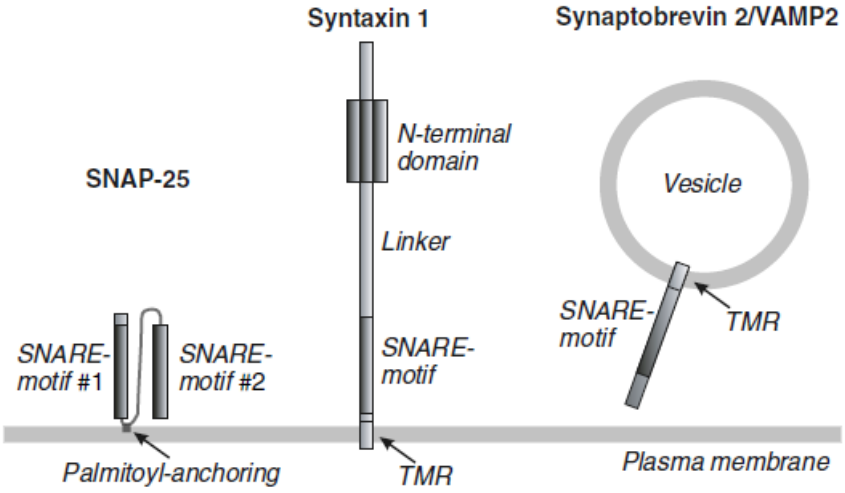

Figure 8. Representation of proteins from the core SNARE complex, their location and sequential motifs. Adapted from (Lang, 2007).

As shown in figure 8, both syntaxin-1 and VAMP2 are attached to the membrane by a transmembrane region (TMR) and have only one SNARE motif. In contrast, SNAP-25 presents two SNARE motifs and no TMR, being the anchoring to the membrane guaranteed by several post-translational palmitoylations.

The fusion reaction requires the formation of a stable complex composed by the three SNARE motifs from the *t*-SNAREs and the one from synaptobrevin (Sutton et al., 1998). This complex is called the core SNARE complex, is resistant to clostridial toxins and its assembly is completely sequential. Initially, as synaptobrevin does not interact with any of the *t*-SNAREs individually, it is necessary that syntaxin-1 and SNAP-25 interact to form a binary complex capable of functioning as a receptor for synaptobrevin. In the ternary complex, the four helices form a parallel and twisted bundle stabilized by 16 layers of interaction (figure 9a). All these layers are hydrophobic, with the exception of the central ionic one, highly conserved and composed by three glutamines from the *t*-SNAREs (one from each SNARE motif) and one arginine from the SNARE motif of synaptobrevin (Lin and Scheller, 2000;Halemani

et al., 2010). This discovery gave rise to an alternative classification for SNARE proteins: *t*-SNAREs are considered *Q*-SNAREs because they contribute with glutamines to the central layer of the complex, and *v*-SNAREs are said to be *R*-SNAREs as they contribute with an arginine (Fasshauer et al., 1998). At this point, as the SNARE motifs of syntaxin-1 and synaptobrevin are adjacent to the respective TMR, the parallel arrangement of the helices imply that the SNARE complex must put the two membranes in great proximity as shown in figure 9b, suggesting that the assembly of the complex could provide the energy needed for fusion (Rizo and Rosenmund, 2008).

SNARE proteins are the basic machinery for fusion, since they are able to promote membrane fusion when reconstituted in lipid vesicles (Weber et al., 1998). However, in living cells, a multitude of other proteins are expressed to guarantee the tight control and high efficiency that is required. Munc13, Munc18-1, complexin and synaptotagmin-1 are some of these proteins (Rizo and Rosenmund, 2008), as presented in figure 9c.

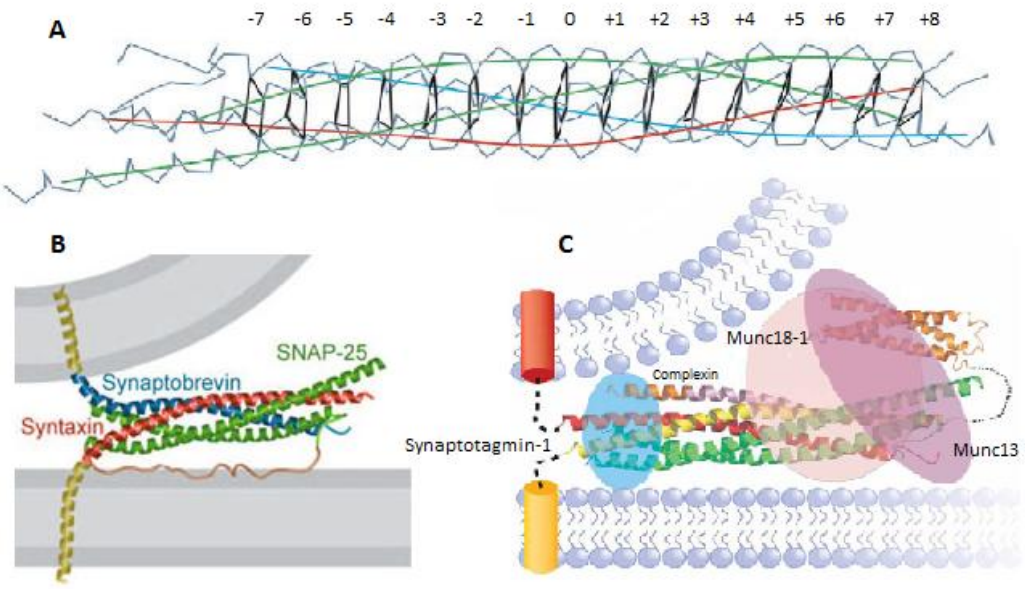

Figure 9. SNARE complex. A) Representation of the 16 layers of interaction between the SNARE motifs. Adapted from (Fasshauer et al., 1998); B) Assembled complex and membranes proximity. Adapted from (Dun et al., 2010) ; C) Positions of other proteins involved in the fusion reaction. Adapted from (Rizo and Rosenmund, 2008).

1.3.3 SNAP-25 palmitoylation

As pointed out before, SNAP-25 anchoring to the plasma membrane is achieved by multiple palmitoylations in the linker region between the two SNARE motifs. In this manner, this post-translational modification is essential to SNAP-25's function.

SNAP-25 has a cystein (Cys)-enriched domain between residues 84-92 that contain four closely spaced Cys residues. The thioester linkage of palmitate to these Cys residues (S-palmitoylation) is carried out by enzymes from the palmitoyl transferase (PAT) family, which share the same aspartate-histidine-histidine-cystein (DHHC) motif in a Cys-rich region. PATs are membrane proteins with several known localizations within the cell, including the endoplasmic reticulum, the Golgi apparatus and the plasma membrane (Prescott et al., 2009).

Palmitoylation increases SNAP-25 lipid affinity, playing an important role in the sorting of the protein to the cytosolic face of the plasma membrane (Greaves and Chamberlain, 2007) and, consequently, in the synaptic process. In fact, SNAP-25 mutants that lack the Cys-enriched domain or in which Cys were replaced by alanines failed to form SNARE complexes and do not promote regulated exocytosis. This seems to indicate that palmitoylation is fundamental to locally concentrate SNAP-25 molecules in the membrane, leading to the formation of enough SNARE complexes to support Ca^{2+}-dependent exocytosis (Koticha et al., 2002).

1.4. Membrane distribution of *t*-SNAREs

t-SNAREs were found to be highly organized in the plasma membrane of PC12 cells. Syntaxin-1a and SNAP-25 are segregated in clusters with high local concentration, and both proteins seem to overlap in more that 86% of the clusters. These clusters have around 50 nm and are usually composed of 30 to 40 syntaxin molecules (Rickman et al., 2010). Since these clusters are preferential sites for vesicle docking and membrane fusion (Lang et al., 2001), it is important to understand what regulates their formation and composition. Although the SNARE protein machinery is essential to membrane fusion, it is now becoming clear that the lipid environment around SNARE proteins plays an important role concerning synapse vesicle release efficiency and regulation.

1.4.1 Role of cholesterol

In membrane model systems, the inclusion of cholesterol was shown to promote clustering of syntaxin-1 even in lipid bilayers that do not favour the formation of liquid ordered domains (Murray and Tamm, 2009) (figure 10).

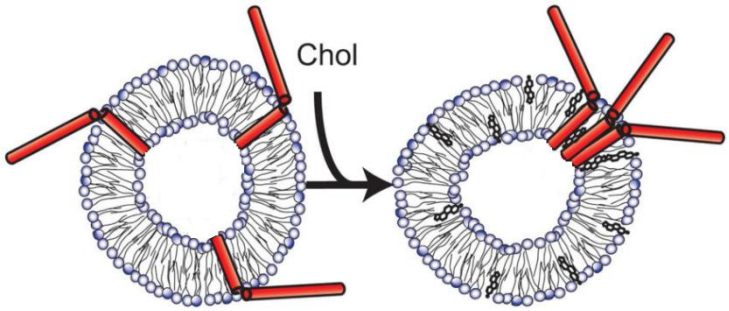

Figure 10. Model for cholesterol-induced cluster formation of syntaxin. Adapted from (Murray and Tamm, 2009).

In PC12 cells, *t*-SNARE clusters also seem to depend on the presence of cholesterol-enriched rafts. When cholesterol is removed from the plasma membrane, clusters disintegrate and exocytosis decreases, suggesting that cholesterol guarantees the high concentration of SNAREs needed to efficient fusion to occur (Lang et al., 2001).

On the other hand, cholesterol appears to have an effect in SNAP-25 targeting to the plasma membrane. Due to the presence of several palmitates in SNAP-25 structure, cholesterol may modulate its activity through a differential insertion of the palmitate groups in the membrane (Rickman et al., 2010).

1.4.2 Relationship between PI(4,5)P_2 location and exocytic sites

Because syntaxin-1 has a juxtamembrane region with basic aminoacid residues, in living cells it interacts with acidic phospholipids as PA and several PIs, including PI(4,5)P_2. Protein-lipid interactions were proposed to structurally and electrostatically contribute to reduce the energy barrier for fusion in the specific sites of exocytosis (Lam et al., 2008).

In the plasma membrane of PC12 cells, $PI(4,5)P_2$ molecules seem to be organized in microdomains and these domains partially co-localize with syntaxin-1 clusters and docked large dense core vesicles (LDCVs) (Aoyagi et al., 2005), as shown in figure 11.

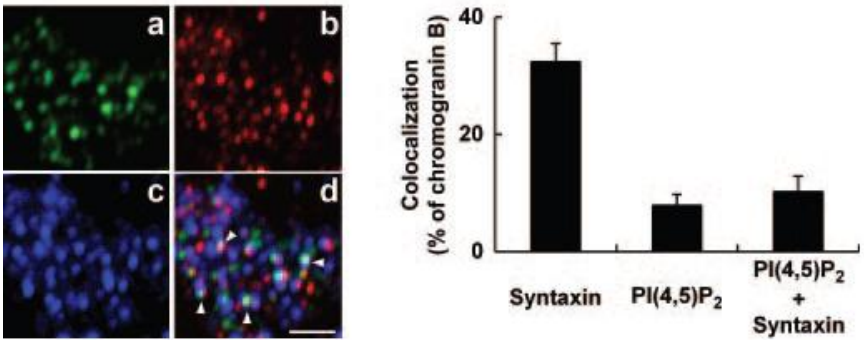

Figure 11. Part of the docked LDCVs is co-localized with $PI(4,5)P_2$ microdomains and syntaxin clusters. Immunostaining for A) chromogranin B present in LDCVs of PC12 cells, B) $PI(4,5)P_2$ and C) syntaxin-1; D) Overlap image. Bar, 2 µm. Adapted from (Aoyagi et al., 2005).

The biophysical properties of $PI(4,5)P_2$ do not favour the membrane negative curvature that is necessary for fusion. However, it is highly concentrated in the vesicle docking sites, at around 6 mol%, and it is essential for the priming step of Ca^{2+}-dependent fusion, in which synaptic vesicles are converted to a ready-releasable state. Moreover, $PI(4,5)P_2$ was observed to inhibit SNARE-dependent liposome fusion, but this inhibition was abolished with the inclusion a priming protein like the Ca^{2+}-dependent activator protein for secretion (CAPS). This suggests that $PI(4,5)P_2$ regulates fusion by directly inhibiting it and, at the same time, recruiting the priming proteins that facilitate the SNARE-dependent synaptic transmission upon Ca^{2+} stimulation (James et al., 2008).

1.5. Main objectives and work organization

The main focus of this project was to elucidate the role of synaptic protein palmitoylation and different calcium concentrations in the distribution of $PI(4,5)P_2$ in the plasma membrane. To address these questions, two distinct and complementary strategies were implemented.

In the first part of this work, *in vivo* experiments were carried out with neuron-like (PC12) and non-neuronal (HEK293) cells. Making use of PH-domains specificity to $PI(4,5)P_2$ molecules, FRET microscopy experiments between PH-CFP (donor) and PH-YFP (acceptor) were performed to evaluate $PI(4,5)P_2$'s distribution in the plasma membrane in the absence and in the presence of the palmitoylation inhibitor 2BP. The efficiency of this inhibitor at the cellular level was assessed by following the alterations in SNAP-25 localization at the plasma membrane, using confocal fluorescence microscopy.

The second set of experiments aimed to understand what is the basic effect of physiological concentrations of calcium ions in the distribution of $PI(4,5)P_2$ in fluid lipid membranes. A self-quenching fluorescence study of the fluorescent analogue TopFluor-$PI(4,5)P_2$ was first performed in POPC LUVs to characterize the behaviour of this fluorescent lipid probe. Then, POPC GUVs incorporating the fluorescent phosphoinositide were imaged by confocal microscopy in the presence of different calcium concentrations to assess its influence on $PI(4,5)P_2$ lateral distribution.

In addition, a GUV immobilization method based on the interaction of biotinylated lipids with an avidin coated surface was also optimized. This was necessary to allow the acquisition of confocal data with higher quality and the future use of single molecule methods.

2. Materials and Methods

2.1. Materials and chemical reagents

1-Palmitoyl-2-oleoyl-*sn*-glycero-3-phosphocholine (POPC), 1,2-di-oleoyl-*sn*-glycero-3-phosphocholine (DOPC), 1,2-dipalmitoyl-*sn*-glycero-3-phosphocholine (DPPC), *N*-palmitoyl-*D*-*erythro*-sphingosylphosphorylcholine (PSM), 1,2-dioleoyl-*sn*-glycero-3-phosphoethanolamine-*N*-(cap biotinyl) (DOPE-Cap-biotin), 1,2-dipalmitoyl-*sn*-glycero-3-phosphoethanolamine-*N*-(biotinyl) (DPPE-biotin), 1,2-dipalmitoyl-*sn*-glycero-3-phosphoethanolamine-*N*-(cap biotinyl) (DPPE-Cap-biotin), 1,2-dioleoyl-*sn*-glycero-3-phosphoethanolamine-*N*-(lissamine rhodamine B sulfonyl) (Rho-DOPE, ε(559 nm, chloroform) = $95x10^3$ $M^{-1}cm^{-1}$, (Pinto et al., 2008)), 1,2-dipalmitoyl-sn-glycero-3-phosphoethanolamine-*N*-(7-nitro-2-1,3-benzoxa-diazol-4-yl) (NBD-DPPE, ε(458 nm, chloroform) = $21x10^3$ $M^{-1}cm^{-1}$, (de Almeida et al., 2005)) and 1-oleoyl-2-{6-[4-(dipyrromethene boron difluoride) butanoyl] amino} hexanoyl-*sn*-glycero-3-phosphoinositol-4,5-bisphosphate (TopFluor-PI(4,5)P_2, ε(495 nm, methanol) = $80x10^3$ $M^{-1}cm^{-1}$ (*Invitrogen*)) were obtained from Avanti Polar Lipids (Alabaster, AL). Avidin from egg white, extrAvidin-FITC conjugate (ε(494 nm) = $84x10^3$ $M^{-1}cm^{-1}$ (*Invitrogen*)) and 2-bromopalmitate (2BP) were from Sigma Chemical Co. (St. Louis, MO). *Trans*-parinaric acid (*t*-PnA, ε(299 nm, ethanol) = $89x10^3$ $M^{-1}cm^{-1}$ (de Almeida et al., 2005)), the membrane probe Alexa Fluor 594-wheat germ agglutinin (λ_{ex}= 590 nm; λ_{em}= 617 nm) and cell culture reagents were obtained from Invitrogen (Breda, The Netherlands). All organic solvents were UVASOL grade from Merck (Darmstadt, Germany).

Lipid stock solutions were all prepared in chloroform, with the exception of TopFluor-PI(4,5)P_2 and *t*-PnA that were prepared in chloroform/methanol (2:1) and ethanol, respectively.

2.2. Cell lines

PC12 cells were used as neuron models. As a non-neuronal control, HEK293 (Human Embryonic Kidney 293) cells were utilized, since they do not present neuron-like properties such as all the machinery of synapse.

2.3. DNA constructs

All pcDNA3 plasmid constructs containing PH domains were obtained by material transfer agreement from the laboratory of Dr. K. Jalink (Netherlands Cancer Institute). CMV-SNAP-25-GFP was a kind gift of Dr. R. Jahn (Max Planck for Biophysical Chemistry). pEGFP-N1 vector was from Clontech (Mountain View, CA). Venus-N1 (Nagai et al., 2002) and monomeric Cerulean C1 (Rizzo et al., 2004) were PCR amplified and inserted into the ptagRFP-N vector (Evrogen, Moscow) via AgeI/NotI, and NheI/NotI respectively. CMV-Cerulean-Venus construct (C11V) was prepared by using a primer for inserting downstream of Cerulean a EcoRI site, and cloning Cerulean into CMV-Venus via NheI/EcoRI.

2.4. Biochemical methods

2.4.1 Cell culture and maintenance

PC12 and HEK293 cells were grown in adherence in flasks coated with poly-*L*-lysine (Sigma Chemical Co., St. Louis, MO) and maintained in Dulbecco's modified Eagle's medium (DMEM) with 10% fetal calf serum (FBS) and 1% penicillin-streptomycin (Sigma Chemical Co., St. Louis, MO), at 37 ºC in an humidified atmosphere with 5% CO_2.

2.4.2 DNA amplification and purification

To transform DH5α bacteria, 40 µL of competent cells were first incubated with ~0.5 µg of DNA, on ice for 30 minutes. Heat-shock (45 seconds at 42 ºC) was performed, followed by further incubation on ice during 1 minute. Bacteria were then grown in antibiotic-free LB medium for 1h at 37 ºC at 250 rpm, allowing them to express antibiotic resistance. Subsequently, cells were plated into LB-agar supplemented with 100 µg/mL of the proper antibiotic, and left at 37 ºC overnight. A colony of transformed bacteria was grown in LB medium supplemented with the appropriate antibiotic at 37 ºC (250 rpm) overnight and used to purify the DNA.

Purification was carried out using the Zyppy^{TM} Plasmid Miniprep Kit from Zymo Research (Irvine, CA). DNA concentration was determined by absorbance measurements at 260 nm (Ɛ=0.02 µg/mL) in a Shimadzu UVPC-3100 spectrophotometer (Shimadzu, Kyoto, Japan). 1x1 cm quartz cuvettes from Hellma Analytics (Müllheim, Germany) were used.

2.4.3 Transfection using cationic liposomes

Cells were seeded in eight-well µ-Slides from Ibidi (Munich, Germany) coated with poly-*L*-lysine at 30 000 cells per well to achieve around 80% of confluence. Transfection was performed using Lipofectamine 2000 (Invitrogen, Carlsbad, CA) for 5h at 0.5 µg plasmid DNA per well. Following transfection, cells were incubated in DMEM without phenol-red for 2-5 days.

2.4.4 Differentiation of PC12 cells

After transfection, PC12 cells were differentiated replacing the growth medium by NGF 100 ng/mL in DMEM with 2% FBS. Cells were exposed to NGF during at least 3 days and the growth medium supplemented with NGF was renewed each 2 days.

2.4.5 Membrane labelling

To label the plasma membrane, Alexa Fluor 594-wheat germ agglutinin (Invitrogen, Carlsbad, CA) was used at a concentration of 5 µg/mL (in PBS). Before measurements, cells were incubated with the probe at 37 ºC during 10 min and then washed with PBS.

2.4.6 Palmitoylation inhibition

Inhibition of palmitoylation was performed 24h after transfection using the palmitate analogue 2-bromopalmitate (2BP). Cells were exposed to a concentration of 50 µM (or 150 µM before FRET experiments) of 2BP and the time of exposure depended on the experiment.

2.5. FRET microscopy in living cells

2.5.1 FRET fundamental concepts

Förster Resonance Energy Transfer (FRET) occurs when a fluorophore in the excited state (donor molecule) displays non-radiative transfer of energy to a molecule in the ground state (the acceptor), through a long range dipole-dipole coupling mechanism (Sun et al., 2011). For FRET to occur, there are three essential conditions that must be achieved: i) donor and acceptor have to be in proximity (1-10 nm); ii) there must be spectral overlap between the spectra of donor emission and acceptor absorption, as shown in figure 12; iii) the absorption transition dipole moment of the acceptor cannot be perpendicular to the emission transition moment of the donor (Pietraszewska-Bogiel and Gadella, 2010).

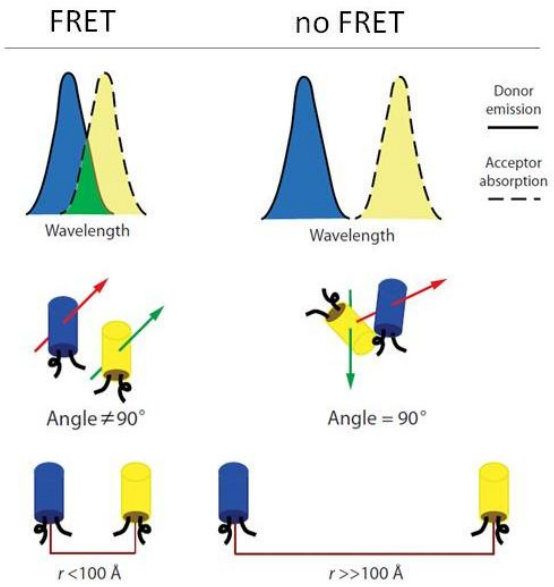

Figure 12. Required conditions for occurrence of FRET. Adapted from (Vogel et al., 2006).

The FRET efficiency (E) is the fraction of donor molecules that transfer energy to acceptor molecules and, for transfer to a single acceptor, is described by the following equation:

$$E = \frac{1}{1 + \left(\frac{r}{R_0}\right)^6} \qquad \text{Eq. 1}$$

where r is the distance between donor and acceptor molecules and R_0 is the distance at which FRET efficiency is 50% (named Förster distance). The value of R_0 is characteristic of each donor-acceptor pair. Note that FRET efficiency is dependent on the inverse of the sixth power of the distance that separates the two fluorophores.

As pointed out before, in addition to fluorophores proximity, a spectral overlap and a good orientation of the dipole moments are also required:

$$R_0^6 = Cn^{-4} Q_D \kappa^2 J \quad (units\ nm^6) \qquad \text{Eq. 2}$$

where C is a constant (8,79x10^{-11} M cm nm^2). The Förster radius depends on the refraction index (n), the quantum yield of the donor (Q_D), the relative orientation of the donor emission and acceptor absorption dipoles (κ^2), and the degree of overlap between the donor emission and acceptor absorption spectra (J).

$$J = \frac{\int F_D(\lambda)\, \varepsilon_A\, \lambda^4\, d\lambda}{\int F_D(\lambda)\, d\lambda} \quad (units\ M^{-1}cm^{-1}nm^4) \qquad \text{Eq. 3}$$

where $F_D(\lambda)$ is the emission spectrum of the donor, ε_A ($M^{-1}cm^{-1}$) is the absorption spectrum of the acceptor and λ is the wavelength (in nm) (Pietraszewska-Bogiel and Gadella, 2010;Sun et al., 2011).

2.5.2 FRET pairs

There are several aspects that must be taken into account when selecting the adequate FRET pair to be used in an experiment. First, considering equation 1, one can see that a greater R_0 value will increase the probability of a FRET event. Increased R_0 values can be accomplished by choosing a donor with a higher quantum yield, an acceptor with a superior extinction coefficient and/or a FRET pair with a higher spectral overlap (see equations 2 and 3) (Sun et al., 2011).

Apart from these parameters, there are also some experimental concerns to be considered. For instance, under certain conditions in FRET microscopy, an easily bleachable donor will lead to an overestimation of FRET efficiency. Moreover, despite the necessary spectral overlap, excitation spectra must be as far as possible from each other to enable the selective excitation of the donor.

The *in vivo* study of protein interactions became more accessible with the discovery and extraction of the Green Fluorescent Protein (GFP) from the jellyfish *Aequorea Victoria* in 1962 (Shagin et al., 2004). In fact, the GFP mutants now available exhibit many different spectral properties, converting fluorescent proteins in a powerful tool when used as FRET donors and acceptors. Furthermore, these proteins can be easily expressed in several cell lines, do not need a cofactor to become fluorescent and can be fused with host proteins, creating a fluorescent fusion protein with the biochemical function of the host (Truong and Ikura, 2001).

One of the first donor/acceptor pairs used to perform FRET studies in live cells was the Blue Fluorescent Protein (BFP)/ GFP pair. However, BFP presents the lowest quantum yield of all GFP mutants and is the most bleachable. In addition, its excitation peak is in the ultraviolet range of the spectrum, where the cellular autofluorescence and scattering become major sources of noise. To overcome these problems, new

mutants were developed. One of the most common FRET donor/acceptor pair in use is the Cyan Fluorescent Protein (CFP)/Yellow Fluorescent Protein (YFP) (figure 13). This pair allows the detection of FRET at longer distances, since the calculated R_0 value is 5,2 nm, while for the BFP/GFP pair is only 4 nm (Truong and Ikura, 2001).

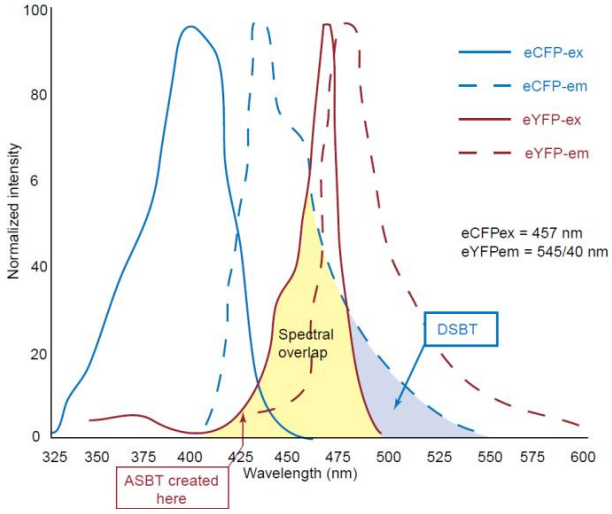

Figure 13. Representation of the spectral overlap and the resulting SBT components for the CFP/YFP FRET pair. DSBT and ASBT are the donor and acceptor SBT contaminants, respectively. Adapted from (Wallrabe and Periasamy, 2005).

2.5.3 FRET microscopy methodologies

Energy transfer is a dark process that cannot be measured directly. Taking this into account, all FRET measurements are based in the detection of changes in photophysical properties of donors and/or acceptors, such as the fluorescence intensity (I) or the fluorescence lifetime (τ):

$$E = 1 - \frac{Q_{DA}}{Q_D} = 1 - \frac{I_{DA}}{I_D} = 1 - \frac{\tau_{DA}}{\tau_D} \qquad \text{Eq. 4}$$

where the indexes refer to the respective property of the donor in the absence (D) and presence (DA) of the acceptor.

Over the last decades, several fluorescence microscopy methods were developed to determine FRET in living cells: intensity and spectral based methods (relying on the

measurement of both donor and sensitized emission), acceptor photobleaching, FRET-Fluorescence Lifetime Imaging Microscopy (FRET-FLIM) and anisotropy FRET imaging. Here, only intensity based methods and FRET-FLIM will be described in the context of this work The detailed description of the other methods can be found elsewhere (Pietraszewska-Bogiel and Gadella, 2010;Sun et al., 2011).

2.5.3.1 Intensity based FRET microscopy

One of the most applied methods to measure sensitized emission in living cells is the filter cube method, mostly because it is very fast and easy to perform, it is non-destructive and can be carried out in a conventional confocal fluorescence microscope (Chen et al., 2006). In this method, three different samples must be prepared: one only with the donor, another with the acceptor and a third one with both donor and acceptor. Three images of all the samples are then acquired using different fluorescent filter cubes:

i) Donor channel (I_{DD}): donor molecules are excited and the emission is collected in the wavelength window corresponding to the donor fluorescence;

ii) FRET channel (I_{DA}): donor fluorophores are excited as in the donor channel, but the emission is collected in the acceptor fluorescence wavelength range;

iii) Acceptor channel (I_{AA}): acceptor molecules are excited and the emission signal is detected selecting the acceptor fluorescence wavelength range.

In most cases, FRET signal data cannot be directly used. As a result of the required spectral overlap, especially when working with fluorescent proteins, spectral bleedthrough (SBT) is often contained in the signal. Usually, there are two main sources of bleedthrough: i) the donor SBT, which results from the detection of the donor emission in the FRET channel, and ii) the acceptor SBT, when the acceptor molecules are directly excited at the donor excitation wavelength, as exemplified in figure 13 (Wallrabe and Periasamy, 2005).

Therefore, the pixel intensities of I_{DD}, I_{DA} and I_{AA} non-corrected images have three potential sources: the donor (I_{dd}), the sensitized acceptor (F_c or I_{DA} fraction due to FRET) and the directly excited acceptor (I_{aa}) intensities. To separate these contributions and correct for the SBT effects, four cross-talk parameters must be calculated:

i) From the images of the sample with only the acceptor it is possible to evaluate the acceptor SBT (a, b):

$$a = \frac{I_{DA}}{I_{AA}} \qquad b = \frac{I_{DD}}{I_{AA}} \qquad \text{Eq. 5 and 6}$$

ii) From the images of the sample with only the donor it is possible to obtain the SBT parameters for the donor emission (c, d):

$$c = \frac{I_{AA}}{I_{DD}} \qquad d = \frac{I_{DA}}{I_{DD}} \qquad \text{Eq. 7 and 8}$$

The I_{DD}, I_{DA} and I_{AA} images of the samples with both donor and acceptor can then be characterized by the following equations:

$$I_{DD} = I_{dd} + \frac{b}{a}F_c + bI_{aa} \qquad \text{Eq. 9}$$

$$I_{DA} = dI_{dd} + F_c + aI_{aa} \qquad \text{Eq. 10}$$

$$I_{AA} = cI_{dd} + \frac{c}{d}F_c + I_{aa} \qquad \text{Eq. 11}$$

Solving this equation system, the corrected pixel intensity values can be obtained as shown below.

$$I_{aa} = \frac{dI_{AA} - cI_{DA}}{d - ca} \qquad \text{Eq. 12}$$

$$I_{dd} = \frac{aI_{DD} - bI_{DA}}{a - bd} \qquad \text{Eq. 13}$$

$$F_c = I_{DA} - aI_{aa} - dI_{dd} \qquad \text{Eq. 14}$$

F_c values (sensitized emission intensities) are not readily convertible to FRET efficiencies. Also, these values are dependent on the instrument and imaging setup, and results obtained in different imaging conditions cannot be directly compared. To overcome this problem, sensitized emission intensities can be converted to quenched

donor intensities through a proportionality constant called G factor. It represents the ratio between the sensitized acceptor emission and the quenched donor emission due to FRET, and it is constant for a given FRET pair and imaging setup. As the unquenched donor intensity is obtained from eq. 13, the FRET efficiency can then be calculated (Chen et al., 2006).

2.5.3.2 *G* factor determination through a FRET-FLIM approach

The fluorescence lifetime is an intrinsic property of each fluorophore and it defines the average time a molecule remains in the excited state before emitting a photon:

$$I(t) = \alpha\, e^{-t/\tau} \qquad \text{Eq. 15}$$

where $I(t)$ refers to the fluorescent intensity at time t, α is the pre-exponential factor and τ is the fluorescence lifetime.

Two methodologies can be used to determine fluorescent lifetimes: i) the time domain approach, where the fluorophore is excited with a pulsed light source and the resulting fluorescent emission is acquired as a function of time (used in the present work); ii) the frequency domain approach, in which the fluorophore is excited with a modulated light source and the lifetime is obtained by determining the phase shift and amplitude attenuation of the emission relative to the excitation (Pietraszewska-Bogiel and Gadella, 2010).

In FRET-FLIM microscopy, energy transfer can be identified by measuring the decrease in the donor's lifetime due to quenching, in the presence of acceptor molecules. After estimating the lifetime values of the donor in the absence and presence of the acceptor, FRET efficiencies can be easily calculated from equation 4. FLIM-based methods are very robust and reliable due to the possibility of acquiring FRET efficiencies without need for additional corrections and reference measurements. In fact, inner filtering, moderate photobleaching of the donor, detector's sensibility and differences in protein concentration in cells (in the case of fluorescent proteins) do not affect the measured lifetime values. On the other hand, since only the donor emission is monitored, factors that affect the quantum yield of the acceptor can be rejected. Moreover, as it is a non-destructive and non-phototoxic method (at short accumulation

times and low excitation power), it can be applied to live cells, in contrast with other methods like acceptor photobleaching. The disadvantages associated with FLIM are the requirement for specialized instrumentation, and the need to detect a relatively large number of photons to obtain accurate results. This does have the potential of inducing acceptor photobleaching.

Here, we used this methodology to determine the *G* factor required to convert sensitized emission values in FRET efficiencies. Three samples have once again to be prepared, one with only the donor, another with the acceptor and a third one with a protein construct including both the donor and acceptor (connected by a linker). First, measurements are performed as described previously for the filter-cube method and the F_c value is obtained using equation 14. Sequentially, the lifetime of the donor in the absence and presence of the acceptor is determined, allowing for the calculation of a FRET efficiency for the donor-acceptor construct. The relationship between the F_c value and the FRET efficiency is given by the following equation (Zal and Gascoigne, 2004):

$$E = \frac{F_c/G}{I_{dd} + F_c/G} \qquad \text{Eq. 16}$$

where F_c/G is the quenched donor emission and $I_{dd} + F_c/G$ is the *predicted* donor emission in the absence of FRET. The *G* factor is then calibrated as the value for which FRET efficiency is equal to the value obtained from the FLIM data.

2.5.3.3 Experimental conditions

To perform filter cube FRET microscopy, three samples were prepared: HEK293 or PC12 cells transfected with i) PH-CFP (or Cerulean); ii) PH-YFP (or Venus) and iii) PH-CFP and PH-YFP (or a Cerulean-Venus construct) in a ratio of 1:1. Cells were placed on a Leica TCS SP5 (Leica Microsystems CMS Gmbh, Mannheim, Germany) inverted confocal microscope (DMI6000). Excitation lines provided by an argon laser were focused into the sample by an apochromatic water immersion objective (63x, NA 1.2; Zeiss, Jena Germany). The emission was detected after passing through a dichroic mirror. A 111,4 µm diameter pinhole in front of the image plane blocked out-of-focus signals. Excitation with 458 nm argon laser line was used for the donor channel (PH-CFP or Cerulean) and FRET channel, while excitation with a 496 nm argon laser

line was used for the acceptor channel (PH-YFP or Venus). Emission was collected between 465 and 500 nm in the donor channel and between 505 and 600 nm in FRET and acceptor channels.

FRET detection through FLIM required the measurement of the donor fluorescence lifetime. Time-correlated single photon counting FLIM (TCSPC-FLIM) was performed using a multiphoton Ti:Sapphire laser (Spectra-Physics Mai Tai BB, 710-990 nm, 100 femtoseconds, 80 MHz). A photomultiplier tube was coupled to the X-port of the microscope and the emitted photons were processed by an SPC board that addresses simultaneously the *xy* location of the collected photons (Becker and Hickl GmbH, PMC-100-4 SPC-830). Moreover, the laser power was adjusted to give an average photon counting rate of ~$1x10^4$-$1x10^5$ photons/s and cell images were acquired during 30-200 seconds to achieve reasonable photon statistics. For FRET efficiency determination, lifetimes of the donor in the absence and presence of the acceptor were obtained setting the Ti:Sapphire laser at 780 nm and the emission was detected after passing through a 470-500 nm band-pass filter (for Venus fluorescence exclusion). Fluorescence lifetimes were obtained by analyzing the fluorescence decays by iterative re-convolution with the instrument response function (IRF) using the SPCImage software (Becker & Hickl, Berlin, Germany).

A detailed description of TCSPC can be found later in this text (section 2.6.6).

2.6. Studies using membrane model systems

2.6.1 Preparation of giant unilamellar vesicles

Giant unilamellar vesicles were obtained by electroformation in Pt wires as previously described (de Almeida et al., 2007). Briefly, lipid solutions were prepared in chloroform (from lipid stock solutions) to a final lipid concentration of 1 mM with the following compositions: DOPC:DPPC (1:1) and POPC:Chol:PSM (1:1:1), both with NBD-DPPE and Rho-DOPE in a probe/lipid ratio of 1:250 and 1:500 , respectively, and with the desired amount of biotinylated lipid. 2 µL of each lipid solution were spread over each Pt electrode. Electroformation was performed at 58 ºC during 75 minutes, in 1 mL of 200 mM sucrose solution (in MilliQ water) preheated at the same temperature. For electroformation to be successful, the temperature has to be necessarily higher than the melting temperature (T_m) of the lipid that presents the higher T_m in the mixture.

After electroformation, the Pt wires were gently shaken in the sucrose solution to release the vesicles to the solution.

For the studies with TopFluor-PI(4,5)P_2, POPC solutions were prepared in chloroform to a final lipid concentration of 1 µM. The stock solution of TopFluor-PI(4,5)P_2 was prepared in a chloroform:methanol mixture (2:1) at 27,8 µM. Independent samples were prepared with 1:500 molar ratio of TopFluor-PI(4,5)P_2. In this case, Rho-DOPE was also used at a probe/lipid ratio of 1:500, and DOPE-Cap-biotin was added to a final biotinylated lipid/total lipid ratio of $1:10^6$. The following procedure was executed as described above. Calcium was added directly to the chambers from freshly prepared $CaCl_2$ stock solutions (in 200 mM glucose) immediately before the experiment. The final calcium concentrations were varied between 0 and 1 mM.

GUVs were observed using confocal fluorescence microscopy.

2.6.2 Immobilization of GUVs using the avidin-biotin method

150 µL of the GUV solution containing one of the studied biotinylated lipid (DOPE-biotin, DPPE-biotin or DPPE-Cap-biotin) were transferred to the wells of an eight-well µ-Slide from Ibidi (Munich, Germany), with or without avidin-coating. 250 µL of a 200 mM glucose solution were then added to the vesicles in the chambers in order to achieve an enrichment of vesicles close to the coverslip surface (as a result of density differences inside and outside the vesicles).

For avidin coating of the slides, 200 µL of a 0,5 mg/mL avidin solution was added to each well and left overnight at room temperature. Vesicles were only added to the slides after extensive washing with MilliQ water to remove excess avidin. Before measurements, slides were left immobile in the dark during at least 20 min, allowing time for GUVs to attach to the surface.

GUVs were observed using confocal fluorescence microscopy.

2.6.3 Preparation of large unilamellar vesicles

Different lipid solutions were prepared (from lipid stock solutions) in chloroform to a final lipid concentration of 2 mM with the following compositions: POPC, DOPC:DPPC (1:1) and POPC:Chol:SM (1:1:1). A biotinylated lipid was included at a molar ratio of 1:100. The lipid solutions were dried under a N_2 flux, left in vacuum overnight and resuspended in 1 mL of pH 7,4 HEPES buffer (10 mM HEPES, 150 mM NaCl, 3,4 mM EDTA) preheated at 50 ºC. *t*-PnA was added at a probe/lipid ratio of 1:200 and freeze-thaw cycles were performed to re-equilibrate and homogenize the samples. Large unilamellar vesicles were then obtained by extrusion of the solutions at 50 ºC with an Avanti Mini-Extruder (Alabaster, AL) using 100 nm pore size polycarbonate membranes.

Regarding the experiments with TopFluor-PI(4,5)P_2, POPC liposomes were prepared to a final lipid concentration of 0,2 mM, with 0, 0.1, 0.25, 0.5, 1 and 2 mol% of the fluorescent phosphoinositide. Extrusion was performed at room temperature.

2.6.4 Confocal fluorescence microscopy

All measurements were performed on a Leica TCS SP5 (Leica Microsystems CMS Gmbh, Mannheim, Germany) inverted confocal microscope (DMI6000). Excitation lines provided by an argon laser were focused into the sample by an apochromatic water immersion objective (63x, NA 1.2; Zeiss, Jena Germany). A 111,4 µm diameter pinhole in front of the image plane blocked out-of-focus signals.

(a) Immobilization studies

For each GUV, two different sets of images were acquired: i) a meridional slice, where it is possible to directly observe the interaction of GUVs with the surface (figure 29a,d; page 55); ii) *xy* slices separated by 0,4 µm along the z-axis, that can be converted in GUV hemisphere projections (figure 29b, c, e and f; page 55). Usually, *xy* slice images were obtained at 400 Hz, while the meridional ones were taken at a 100 Hz frequency. Projections were constructed using the maximum intensity projection

(MIP) method (Boucheny et al., 2009). For the controls without PE-biotin, a faster image acquisition had to be performed. Every slice was acquired in two different channels. In the first one, excitation was performed at 458 nm and emission was collected between 480-530 nm to image NBD-DPPE molecules (ordered phases). In the Rho-DOPE channel, the sample was excited at 514 nm, while emission was acquired at a 530-650 range. With respect to the meridional slices, surface reflexion was also measured by exciting and collecting emission at the same wavelength (NBD excitation wavelength, in this case).

From the study of these giant vesicles, we expected to evaluate the effect of the immobilization method in two different GUV's properties:

i) Vesicles shape

To evaluate if immobilization alters the GUV's shape, we used the meridional slice of each giant vesicle, combining the three channels in the same image as shown in figure 29a and d (page 55). Using ImageJ (Wayne Rasband, NIH, USA) to fit an ellipse to each image, it is possible to quantify how close each vesicle is from a perfect circular shape. To do this, we used a parameter called ellipticity ($Ellip$):

$$Ellip = 1 - \frac{(M-m)}{M} \qquad \text{Eq. 17}$$

where M and m are the major and minor axis of the ellipse, respectively. This means that the closer the ellipticity is to 1, the more similar the vesicle is to a perfect circular shape. As GUVs do not have all the same size, ellipticity values, as all the others studied parameters, are presented as a function of the interaction length of the vesicle with the surface (S_{int}) normalized to the vesicle radius (r_{GUV}) (figure 14).

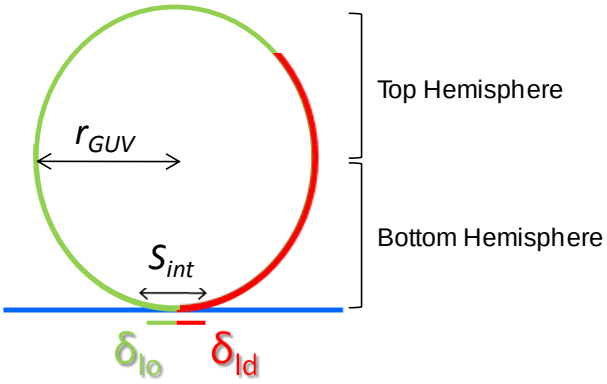

Figure 14. Schematic representation of a GUV and the correspondent analyzed sections: top hemisphere, bottom hemisphere and interaction length (S_{int}). δ_{lo} and δ_{ld} are the liquid ordered and liquid disordered lengths, respectively, that compose the interaction surface. r_{GUV} is the radius of the liposome.

ii) Domain distribution

To evaluate how the immobilization method influences the domain distribution in each giant vesicle, we analyzed each GUV in three different sections (figure 14):

1) Top hemisphere;
2) Bottom hemisphere;
3) Interaction surface.

Often, when performing confocal fluorescence microscopy measurements on GUV samples, only the projection corresponding to the top hemisphere is used for data analysis. However, the immobilization method could induce perturbations that might result in domain redistribution within the entire vesicle. To address this hypothesis, we used the *xy* hemisphere projections (see figure 29b, c, e and f; page 55) to calculate the fraction of liquid ordered (or gel) phase in each hemisphere, $f(lo)$:

$$f(lo) = \frac{A_{lo}}{A_{lo}+A_{ld}} \qquad \text{Eq. 18}$$

where A values represent the area of liquid ordered and liquid disordered phases. An equivalent equation was used to calculate the fraction of gel phase in g/f GUVs ($f(g)$).

Additionally, a more pronounced effect is expected to be observed closer to the avidin-coated surface. At this level, we calculated the fraction of lo (or gel) in the interaction surface ($f(\delta_{lo})$ or $f(\delta_g)$), as shown in figure 14 and equation 19.

$$f(\delta_{lo}) = \frac{\delta_{lo}}{S_{int}}$$ Eq. 19

The interaction lengths and areas of lipid domains were determined using ImageJ.

(b) PI(4,5)P_2 distribution studies

Images were acquired at 400 Hz in two sequential scans:

i) TopFluor-PI(4,5)P_2 scan: excitation at 488 nm and emission collection between 495 and 530 nm (in this range, no fluorescence of Rho-DOPE is collected);
ii) Rho-DOPE scan: excitation performed at 514 nm and emission collected at 570-700 nm (at this excitation wavelength, only residual TopFluor excitation occurs).

xy slices separated by 0,4 µm along the z-axis can then be converted in GUV projections using the maximum intensity projection (MIP) method (Boucheny et al., 2009).

2.6.5 Steady-state fluorescence spectroscopy

Fluorescence steady-state measurements were carried out with a SLM-Aminco 8100 Series 2 spectrofluorimeter (Rochester, NY; with double excitation and emission monochromators, MC-400) in a right-angle geometry. The light source was a 450-watt Xe arc lamp and the reference was a Rhodamine B quantum counter solution. 5x5-mm quartz cuvettes from Hellma Analytics were used. Temperature was controlled to 25 ºC by a thermostatted cuvette holder and magnetic stirring was used.

Measurements of *t*-PnA fluorescence intensity were performed exciting the fluorophore at 305 nm and collecting the emission at 405 nm. *t*-PnA spectra were not recorded to avoid bleaching of the sample. Excitation and emission spectral bandwidths were 2 and 16 nm, respectively, in order to minimize the bleaching and optimize emission acquisition.

2.6.6 Time-resolved fluorescence measurements

Fluorescence decay measurements were carried out making use of the Time-Correlated Single-Photon Timing (TCSPT) technique. In this technique, the sample is excited by a pulsed radiation source with a high repetition rate. Experimental conditions are adjusted so that, for each excitation pulse, the probability of detecting a photon emitted by the sample is less than 1%. After each laser pulse, a voltage ramp is started in a time-amplitude converter. The voltage ramp stops when the first emitted photon is detected. The measured voltage is then proportional to the time between the sample excitation and the detection of the first emitted photon. Sequentially, a multichannel analyzer converts the voltage to a temporal channel, using an analog-digital converter. Through the accumulation of several pulses it is possible to acquire a histogram of photon counts as a function of time. This histogram represents the probability of a photon emission event as a function of the elapsed time since the excitation of the sample.

The excitation pulse was obtained from a Ti:Sapphire solid state laser system. It consists in a diode-pumped solid state Nd:YVO_4 Milennia Xs (Spectra Physics, Mountain View, CA), which in turn pumps a Tsunami (Spectra Physics, Mountain View, CA) Ti:Sapphire laser with modes interconnection. The exit pulses of this laser present a temporal duration below 100 fs, a repetition rate of ~80 MHz and a tune range of 700-1000 nm, and are chosen by a pulse selector (Angewand Physik and Electronik) to reduce the repetition rate to 4 MHz.

2.6.6.1 Data analysis

The fluorescence intensity decay of a fluorophore, $I(t)$, is in some cases described by a monoexponential curve:

$$I(t) = I_0 \exp(-t/\tau) \qquad \text{Eq. 20}$$

where I_0 is the fluorescence intensity at $t = 0$ and τ is the lifetime of the fluorophore that, as pointed out before, represents the average time a fluorophore remains in the excited state before returning to the ground state through fluorescence emission.

However, in most cases the decay is not this simple and has to be described by more than one exponential:

$$I(t) = \sum_{i=1}^{n} \alpha_i \exp(-t/\tau_i) \quad \text{Eq. 21}$$

where α_i is the i pre-exponential factor or normalized amplitude ($\sum_{i=1}^{n} \alpha_i = 1$) and τ_i is the i^{th} component lifetime. Then, the average lifetime $\langle\tau\rangle$ of a fluorophore with a multi-exponential intensity decay can be described by:

$$\langle\tau\rangle = \frac{\sum_{i=1}^{n} \alpha_i \tau_i^2}{\sum_{i=1}^{n} \alpha_i \tau_i} \quad \text{Eq. 22}$$

The relationship between the steady-state fluorescence intensity of a sample, I, and its fluorescence intensity decay, $I(t)$, is given by the following equation:

$$I = \int_0^{\infty} I(t)dt \quad \text{Eq. 23}$$

By taking equation 23 into account, one can conclude that the lifetime weighted with the amplitude (α_i) of each i component of the decay, $\bar{\tau}$, is proportional to the area below the decay curve. This means that $\bar{\tau}$ is proportional to the quantum yield of the studied fluorophore and, for this reason, is frequently designated by lifetime-weighted quantum yield:

$$\bar{\tau} = \sum_{i=1}^{n} \alpha_i \tau_i \quad \text{Eq. 24}$$

To analyze the intensity decay curves acquired by TCSPT, one must consider they do not directly represent the emission kinetics that would be obtained if the sample was excited with a pulse of infinitesimal duration. The experimental decay curves, $I_{exp}(t)$, are indeed distorted by the finite duration pulse of the instrumental response function, $L(t)$, and can be described by the following convolution integral:

$$I_{exp}(t) = \int_0^t L(t').I(t-t')dt = L \otimes I \quad \text{Eq. 25}$$

The analysis was carried out using a nonlinear, least-square iterative convolution method based on the Marquardt algorithm (Marquardt, 1963). Briefly, the intensity decay of the sample is first calculated, $I_{calc}(t)$, through a convolution of the instrumental response function of the system with the empirical function $I(t)$ described by equation 23:

$$I_{calc}(t) = L \otimes I \qquad \text{Eq. 26}$$

Then, α_i and τ_i that best describe the emission kinetics are optimized by performing a nonlinear regression by the least-squares method. The sum of the squared deviations between $I_{exp}(t)$ and $I_{calc}(t)$ are iteratively minimized applying the Marquardt algorithm (Marquardt, 1963), using a homemade software. The goodness of the fit was judged from the experimental χ^2-value, weighted residuals and autocorrelation plot. In every analysis, χ^2 value was less than 1.3 and both residuals and autocorrelation were randomly distributed around zero.

2.6.6.2 Experimental conditions

TopFluor-PI(4,5)P_2 was excited at 460 nm, and fluorescence emission was acquired at 503 nm. The emission wavelength was selected by a Jobin Yvon HR320 monochromator (Horiba Jobin Ivon Inc.). The excitation pulse profile was obtained with a Ludox scattering solution (aqueous solution of colloidal silica (Sigma-Aldrich Co., St. Louis, MO). Decay curves were stored in 1024 channels and the used time scale was 29.3 ps/channel. Tipically, around 20 000 and 50 000 counts were obtained in the histogram peak channel of the sample and the instrumental response function, respectively. 5x5-mm quartz cuvettes from Hellma Analytics were used.

2.7. Image analysis

All analysis of confocal imaging data was carried out using ImageJ (Wayne Rasband, NIH, USA) and homemade software developed by Dr. Fábio Fernandes in a Matlab environment (Mathworks, Natick, MA).

3. Results and discussion

3.1. Clustering of PI(4,5)P_2 in the plasma membrane of non-neuronal (HEK293) and neuron-like (PC12) cells

To understand how PI(4,5)P_2 is organized in the plasma membrane of living cells, we aimed to compare its distribution in HEK293 and PC12 cells. To assess this issue, cells were co-transfected with PH-CFP and PH-YFP constructs in a 1:1 DNA ratio (plus the samples with only PH-CFP donor and PH-YFP acceptor) and filter-cube FRET microscopy (Chen et al., 2006) was performed as described in section 2.5.3.3. This experiment was based on the fact that, for larger densities of PI(4,5)P_2 in the membrane, the larger will be the energy transfer from PH-CFP to PH-YFP due to increased proximity of these proteins at high PI(4,5)P_2 density sites (figure 15). Naturally, FRET efficiencies between different cells will differ significantly depending on protein expression levels.

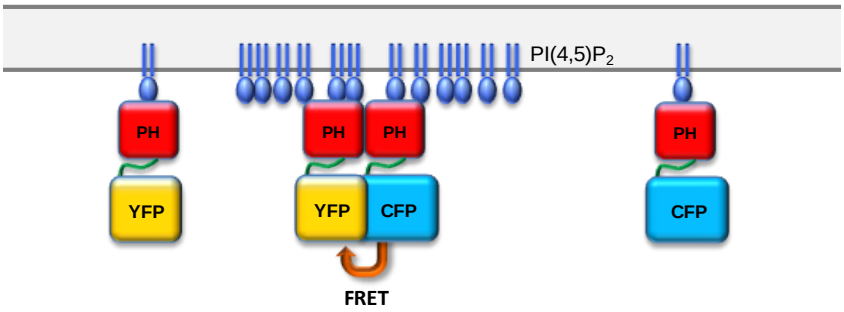

Figure 15. Representation of the FRET experiment designed to determine PI(4,5)P_2 distribution in the plasma membrane of HEK293 and PC12 cells.

3.1.1 Confirmation of PLCδ_1-PH-GFP sorting to the plasma membrane of PC12 cells

In order to ensure that fusion of fluorescent proteins with PLCδ_1-PH did not affect the localization of the protein domain in the plasma membrane of living cells, non-differentiated adherent PC12 cells were alternatively transfected with GFP and PH-

GFP plasmids. One day after transfection, confocal fluorescence images were acquired, using the 488 nm line of an Argon laser for excitation and collecting fluorescence emission between 500 and 600 nm (figure 16).

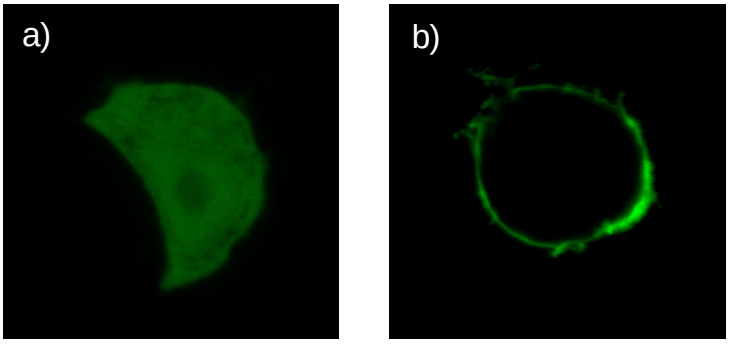

Figure 16. Non-differentiated PC12 cells after 1 day of transfection with a) GFP and b) PH-GFP constructs. Excitation was performed at 488 nm, and emission was detected in the 500-600 nm range.

As shown in figure 16a, GFP localizes in the cytosol of PC12 cells as expected, and the PH domain construct is sorted to the plasma membrane (Figure 16b), as a consequence of binding to $PI(4,5)P_2$. Very high overexpression levels of PH-domains can induce interruption of plasma membrane-cytoskeleton contacts and cell rounding (Halet, 2005). In these conditions, and because of the rapid on–off rate of binding to PH domains, $PI(4,5)P_2$ is still sensitive to PLC-mediated hydrolysis as well as to 5-phosphatases, and as such, sequestration of the $PI(4,5)P_2$ pool by PH domains is functionally not so relevant (Balla, 2007). Moderate expression levels of these proteins are well tolerated by cells, as shown by the creation of transgenic mice expressing PH-domain GFP reporters without functional defects (Nishio et al., 2007).

3.1.2 Determination of the G factor for FRET analysis through the filter cube method

To perform filter-cube FRET studies, we first determined the *G* factor required for conversion of sensitized emission values (F_c) to FRET efficiencies.

Three samples of transfected HEK293 cells were prepared: one with the modified cyan fluorescent protein Cerulean, another with the modified yellow fluorescent protein Venus, and a third one with a Cerulean-Venus construct with an 11 aminoacid-linker

(C11V). I_{DD}, I_{DA} and I_{AA} images were acquired as described in section 2.5.3.3 (page 29). To analyze these images, a homemade software was developed. Briefly, a region of interest (ROI) with no cells is chosen in the I_{DA} image, and the mean intensity value (I_B) is calculated in all channels for those pixels. To correct for the background (mostly dark current), the value of I_B is subtracted to all the pixels in the correspondent image channel. Then, from the samples with only donor and only acceptor, bleedthrough parameters *a*, *b*, *c* and *d* are determined by selecting a new ROI containing significant protein fluorescence and applying equations 5-8 (page 26-27). These parameters are kept constant during the analysis of the sample with both donor and acceptor. In this manner, after removing the background intensity, it is possible to obtain the corrected I_{dd}, F_c and I_{AA} images, making use of equations 12-14 (page 27).

Finally, the lifetimes of Cerulean alone and linked to the acceptor Venus were measured by FLIM as previously described, to obtain the FRET efficiency value. Applying equation 16 (page 29), it was possible to determine the G factor to be used in the following experiments. The recovered G value was 1.14.

To use this G value in subsequent experiments, it has to be taken into account that it depends on the FRET pair and the experimental image setup. This means that each image in subsequent experiments had to be acquired in the same imaging conditions. Moreover, to perform the FRET experiments, PH-CFP and PH-YFP were used, instead of Cerulean and Venus. They were not used to determine the G value because only the C11V construct was available at the time. Although Cerulean and Venus are only slightly modified CFP and YFP proteins, respectively, and despite displaying identical spectral properties, they present some significant differences. In fact, Cerulean has a quantum yield 1.5 times higher than CFP (Rizzo et al., 2004). Since the *G* factor is expected to be directly proportional to acceptor quantum yield and inversely proportional to donor quantum yield, the *G* factor for CFP-YFP FRET transfer is expected to be 0.76. Here, we will present the FRET data calculated using the measured *G* factor from Cerulean and Venus, as the *G* factor of 0.76 for CFP-YFP is only an estimative. As such, the obtained FRET efficiencies from the filter cube method are underestimating the real FRET efficiencies. However, estimatives for FRET efficiencies can be directly calculated from our data as seen in figure 17.

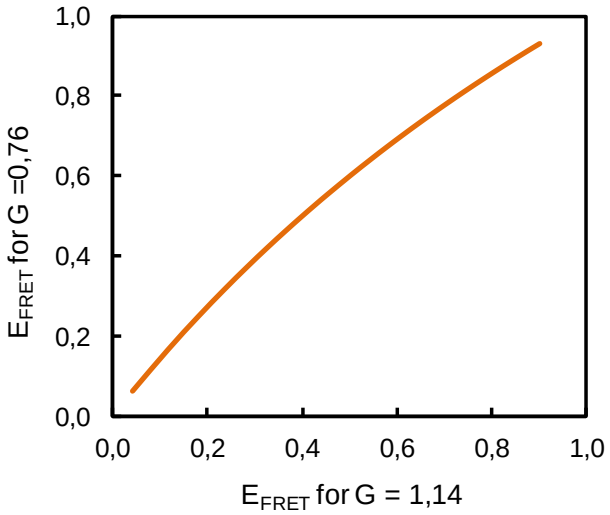

Figure 17. Relationship between FRET efficiencies obtained using a *G* factor of 1.14 (Cerulean-Venus) to the values obtained using the expectable *G* factor of 0.76 for CFP-YFP, in the conditions of our measurements.

Experiments for quantification of the actual CFP-YFP *G* factor are currently under way and have not been included in this thesis. The use of FRET-FLIM alone in the FRET studies with PH-CFP and PH-YFP would not require these type of controls. However, the expression levels of PH domain constructs are very low in PC12 transfected cells and only a small fraction of transfected cells were bright enough for FLIM measurements.

On the other hand, comparisons between different cell types will not be a problem, as the measured value of *G* can be used to analyze FRET in both HEK293 and PC12 cells.

3.1.3 HEK293 cells

We first started with the HEK293 cells, since they lack all the synaptic machinery and, consequently, were expected to present a more homogeneous distribution of $PI(4,5)P_2$ molecules within their plasma membrane. Only cells transfected with both PH-CFP and PH-YFP were analyzed. Transfection was detected by inspection of the fluorescence signals in the different detection channels.

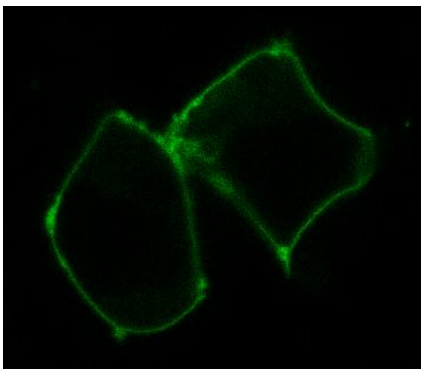

Figure 18. PI(4,5)P_2 distribution in the plasma membrane of HEK293 cells, reported by PH domains localization and FRET efficiency (from PH-CFP to PH-YFP). I_{DA} image (FRET channel) obtained by excitation of PH-CFP at 458 nm and emission collection at 505-600 nm – an apparently homogeneous distribution can be observed (no clusters above the microscope resolution).

In figure 18, it is possible to observe the apparent homogeneous distribution of PI(4,5)P_2 reported by sensitized fluorescence emission of PH-YFP. Although some areas of the membrane seem to present a higher fluorescence intensity, they do not actually correspond to higher FRET efficiency values as this is an artifact caused by membrane ruffling and deformation (Balla, 2007).

SBT parameters were obtained from samples with only donor (PH-CFP) or acceptor (PH-YFP). To guarantee the same transfection conditions, these samples were always prepared together with the sample containing both donor and acceptor. Once again, a homemade software was developed to analyze the data and determine FRET efficiency. After removing the background intensity and obtaining the I_{dd}, F_c and I_{aa} images, the software was set up to calculate the FRET efficiency in each pixel of a chosen membrane ROI (equation 16, page 29) and build a histogram with those values (figure 19). The most frequent FRET efficiency value (E_{mode}) was then used in all the comparisons. The average values of E were almost always very close to E_{mode}. However, we believe that the use of E_{mode} is more accurate in describing the state of the system as artifacts are more likely to arise when accounting dim pixels (which often correspond to FRET efficiencies in the edge of the histogram; figure 19) with the same weight than bright pixels.

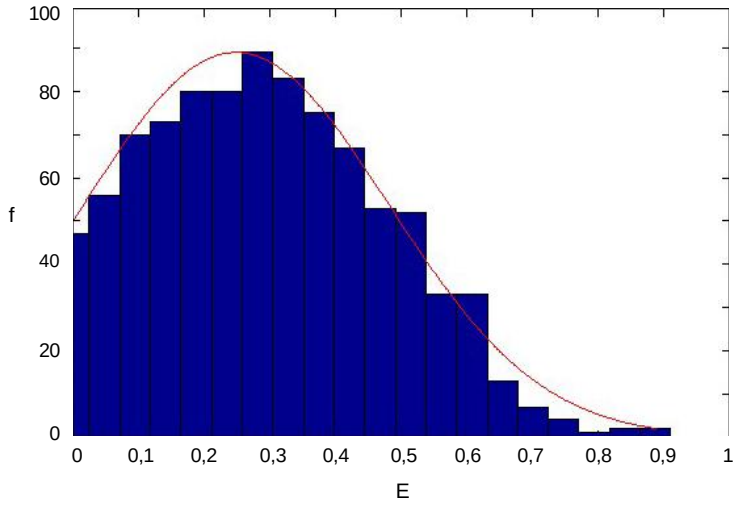

Figure 19. Histogram of FRET efficiency distribution in an HEK293 cell. f is the number of pixels. The red line represents a Gaussian fit to the experimental results. E_{mode} is the FRET efficiency value that corresponds to the maximum frequency observed. In this particular case, $E_{mode}$is 0.25.

Quantitatively, E_{mode} values were obtained from several HEK293 cells and are presented in figure 20 as function of the acceptor's fluorescence intensity (I_{aa}) in each analyzed cell; the calculated average E_{mode} is 0,28±0,05 (*n* =14). The low correlation between protein expression levels (I_{aa}) and E_{mode} values suggests that PH domains are possibly clustering under the resolution of the microscope. Additional experiments will be necessary to fully resolve this issue.

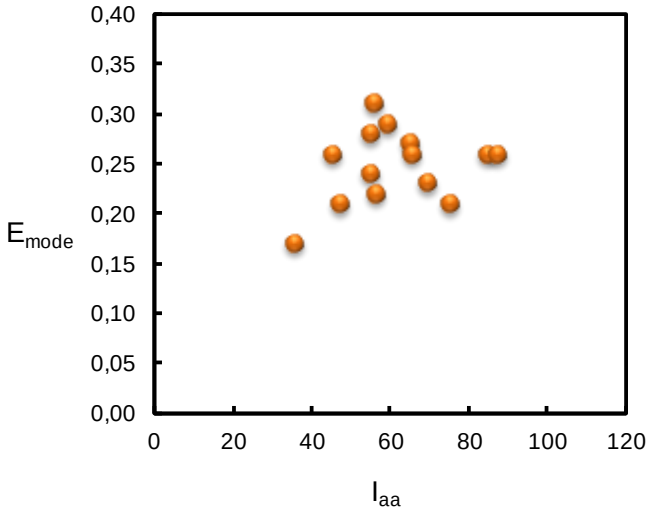

Figure 20. Variation of the determined E_{mode} with I_{aa}, i. e., effect of acceptor's concentration in the determined FRET efficiency values.

3.1.4 PC12 cells

NGF-induced differentiation of PC12 cells induces significant changes in protein expression levels and SNARE distribution throughout the cell (Westerink and Ewing, 2008). In this context, it is essential to distinguish non-differentiated from differentiated cells. To prove that this can be easily done through direct observation of the cells, PC12 cells were transfected with a PH-GFP construct and exposed to NGF during four days. Confocal fluorescence images were obtained by exciting the sample at 488 nm and collecting emission at 500-600 nm (figure 21).

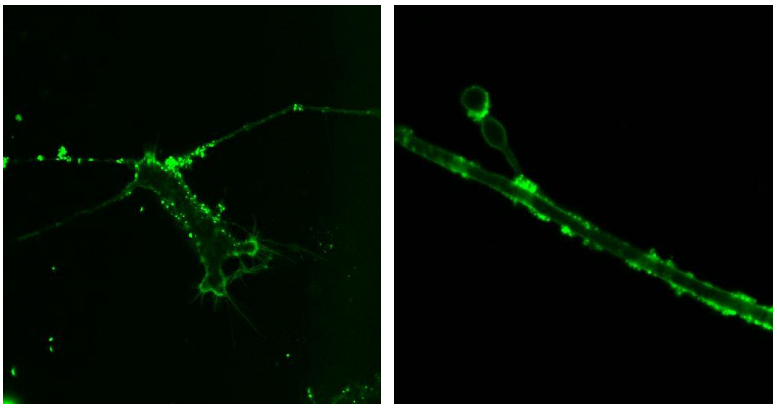

Figure 21. PC12 cells expressing PH-GFP, after 4 days of NGF-induced differentiation. Cells were excited at 488 nm and emission was acquired between 500 and 600 nm.

The growth of neuritis can be clearly visualized in PC12 cells differentiated with NGF after 4 days of exposure. PH domain distribution in the plasma membrane is also more heterogeneous than in non-differentiated cells (figure 16b).

Therefore, the same procedure was followed to repeat the FRET experiment in differentiated PC12 cells, after 3 days of exposure to NGF. Typical results are shown in figure 22.

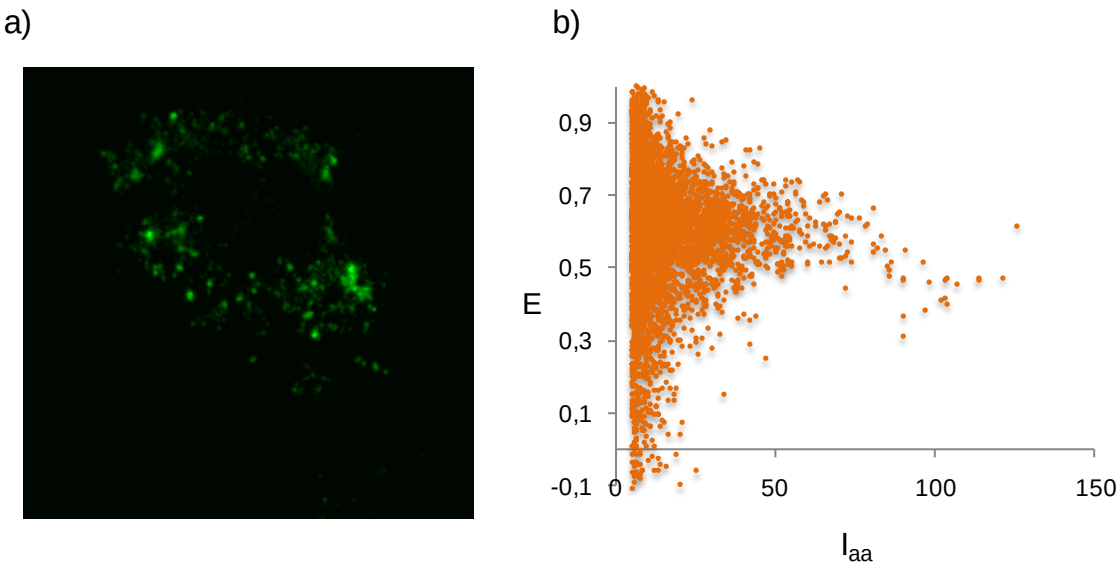

Figure 22. PI(4,5)P_2 distribution in the plasma membrane of PC12 cells after 3 days of differentiation using NGF, reported by PH domains localization and FRET efficiency (from PH-CFP to PH-YFP). a) I_{DA} image (FRET channel) obtained by excitation of the donor PH-CFP at 458 nm and emission collection at 505-600 nm – clusters of PH domains are observed; b) variation of FRET efficiency values within the same cell, as a function of the acceptor's intensity I_{aa} ($E_{mode} = 0{,}65$).

In this case, a punctate distribution of PH domains is visible in the confocal image (figure 22a). The average E_{mode} for PC12 cells was 0,59±0,06, which is clearly above the value obtained for HEK293 cells. Taking into account that PH-YFP expression levels in PC12 cells (as reported by I_{aa}) are significantly lower than for HEK293 cells, it is clear that clustering does take place in the spatial scales where FRET is significant (<100 nm), and that inside the observed puncta, PI(4,5)P_2 molecules are clustered at much higher densities than in HEK293 cells.

The fluorescence intensity in the PC12 puncta is heterogeneous, and PH domain concentration is expected to present significant variability at different sites of the membrane. In figure 23, the histogram of average I_{aa} values for each puncta is presented, showing this heterogeneity.

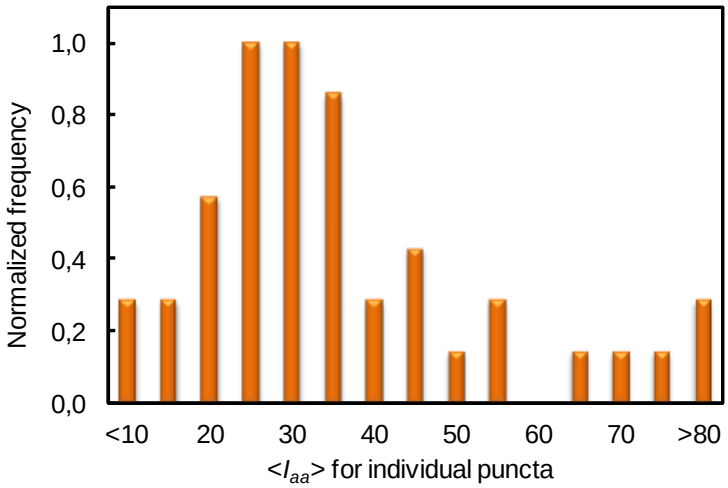

Figure 23. Normalized frequency of average I_{aa} values for individual puncta in differentiated PC12 cells. Puncta intensity is variable.

We also analyzed the influence of puncta fluorescence intensity on FRET efficiencies by applying different filters to the I_{aa} values. Sequentially we eliminated from the distribution of E_{mode} values, pixels with an I_{aa} value lower than 20, 40 and 80. In figure 24, distributions of pixels with a given E value normalized to 1 are presented.

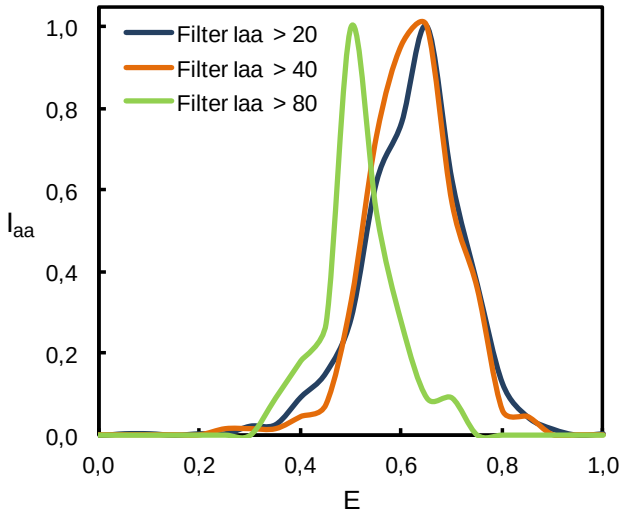

Figure 24. Normalized distributions of pixels with a given E value in PC12 cells . Three distinct I_{aa} filters were applied, eliminating from the analysis pixels with an I_{aa} value lower than 20 (blue), 40 (orange) and 80 (green). The more pixels are eliminated, the higher is the fraction of pixels with high I_{aa} values, i.e., different filters select for different puncta in PC12 cells.

Most of the puncta observed in the confocal microscope presented identical FRET efficiencies independently of the acceptor concentration (as measured by I_{aa}). Once

more, this is an indication that PI(4,5)P_2 molecules seem to form clusters with a similar high density at different sites in the plasma membrane. If these species were homogeneously distributed, FRET should increase for higher densities of acceptor molecules. However, for the brighter puncta ($\langle I_{aa} \rangle$ > 80), FRET efficiency is slightly lower suggesting that the distribution of PH domains is different (figure 24).

Manipulation of PC12 cells is significantly more challenging than working with HEK293 cells. Namely, transfection efficiency and resistance to the transfection agent are much lower in PC12 cells. As a consequence the number of cells studied in each experiment was much smaller than for HEK293, and additional work will be necessary to confirm this result in a larger cellular population.

3.2. Protein palmitoylation and PI(4,5)P_2 distribution in HEK293 and PC12 cells

In order to evaluate the effect of protein palmitoylation in the membrane distribution of PI(4,5)P_2, we exposed HEK293 and PC12 cells expressing PH-CFP and PH-YFP to the palmitoylation inhibitor 2BP at 150 µM during 24h. 2BP was already shown to irreversibly inhibit protein palmitoylation both *in vivo* and *in vitro* (Webb et al., 2000;Jennings et al., 2009;Draper and Smith, 2009). Filter-cube FRET microscopy was performed as previously described; FRET efficiency results obtained in HEK293 cells co-transfected with PH-CFP and PH-YFP are presented in the figure bellow.

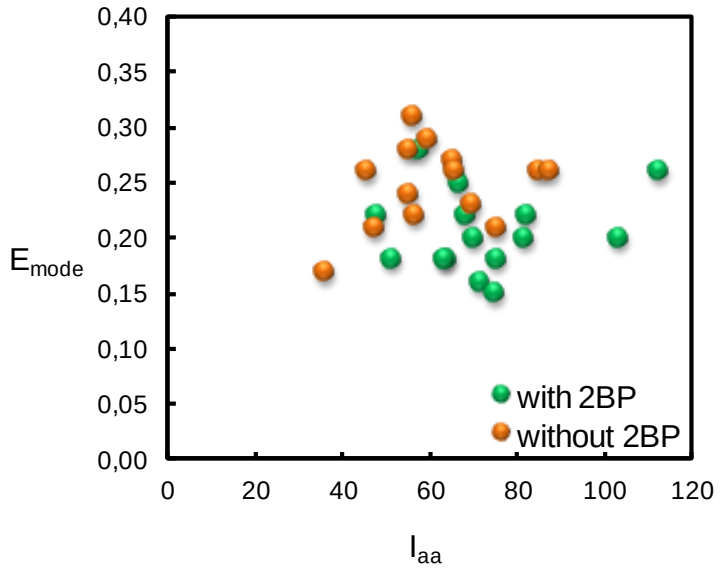

Figure 25. FRET efficiency values obtained in HEK293 cells co-transfected with PH-CFP and PH-YFP, with (green; E_{mode}= 0,23±0,05) and without (orange; E_{mode}= 0,28±0,05) a 24h exposure to 2BP 150 µM.

Although an effect of palmitoylation was not expected, the exposure to 2BP seemed to generally decrease the FRET efficiency in HEK293 cells. In fact, the average E_{mode} decreased from 0,28±0,05 to 0,23±0,05. This reinforces the idea that PI(4,5)P_2 molecules are slightly organized in the membrane, and palmitoylated proteins contribute to localized enrichment of this lipid below the resolution of the confocal microscope.

It was not possible to address the influence of palmitoylation inhibition in differentiated PC12 cells, due to experimental difficulties concerning high cell death rates caused by transfection and also by exposure to 2BP. The protocol for palmitoylation inhibition has since then been optimized and experiments with PC12 cells will be carried out in the future.

3.2.1 Influence of palmitoylation on the localization of SNAP-25 in non-differentiated PC12 cells

Since almost no differentiated PC12 cells survived to 2BP exposure, we decided to use non-differentiated PC12 to address which is the effect of palmitoylation inhibition in SNAP-25 localization. To perform the experiment, non-differentiated PC12 cells were first transfected with a SNAP-25-GFP construct. Two days after transfection, cells were incubated with 2BP only at 50 µM, to inhibit protein palmitoylation, during 0, 2, 4, 6 and 26 hours. After the respective incubation time, the inhibitor was removed and Alexa Fluor 594-wheat germ agglutinin (AF594-WGA) was added to the chambers during 10 min at 37 ºC to label the plasma membrane. Wheat gern agglutinin (WGA) is a 38 kDa carbohydrate-binding protein that selectively binds to N‑acetylglucosamine and N‑acetylneuraminic acid (sialic acid) residues, which are predominantly found on the external leaflet of the plasma membrane. For this reason WGA fluorescent conjugates are frequently used as markers of plasma membranes.

Hereafter, cells were washed with serum- and antibiotics-free medium and fluorescence intensity images were obtained by confocal fluorescence microscopy. Two images of each cell were acquired, corresponding to two different sequential scans. In the first scan, the excitation was performed with a 476 nm laser line and emission was collected between 490 and 570 nm to detect GFP fluorescence. The second scan aimed to excite AF594-WGA with a 514 nm laser line, collecting the respective fluorescence emission in the 610-700 nm range, to detect Alexa Fluor 594

fluorescence. Figure 26 shows representative examples of the images obtained from both scans with different incubation times with 50 µM 2BP.

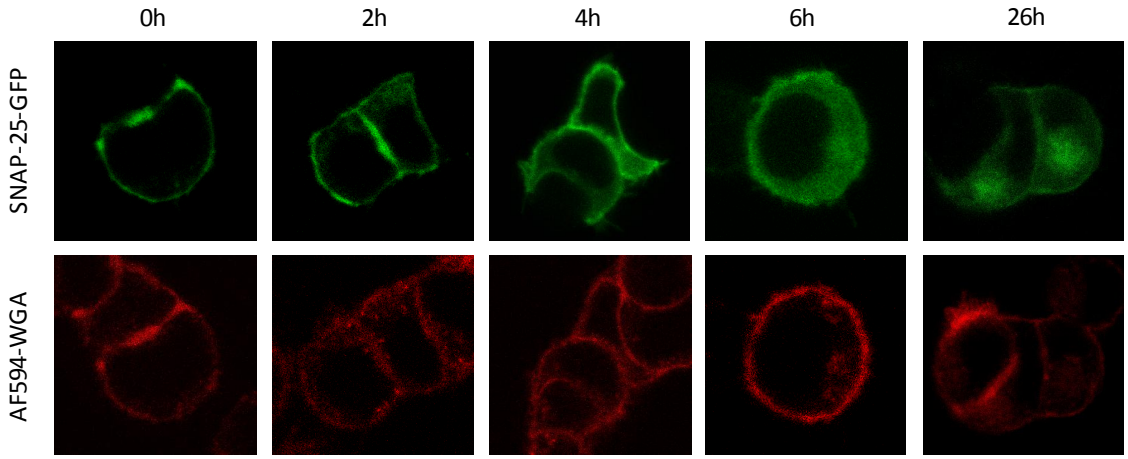

Figure 26. Effect of palmitoylation inhibition on SNAP-25-GFP location in non-differentiated PC12 cells. Cells were exposed to 2BP at 50 µM during 0, 2, 4, 6 and 26 hours. Two sequential scans were performed at a 100 Hz frequency. SNAP-25-GFP scan (green): excitation at 476 nm and emission collection between 500 and 600 nm; AF594-WGA scan (red): excitation at 514 nm and emission acquired between 610 and 700 nm

With the two scan images, SNAP-25-GFP fluorescence in the membrane can be distinguished from the cytosol, using a digital filter mask obtained from the AF594-WGA image. After choosing an area without cells – a dark ROI –, a homemade software was set up to calculate the mean dark counts in both channels. Subtracting the values to the correspondent image, images corrected for dark counts can be obtained. The second step concerned the distinction of membrane and intracellular pixels. Initially, a new ROI had to be selected to frame an area with transfected cells – due to the low transfection efficiency of PC12 cells, it was frequent to observe cells labelled with AF594-WGA, but with no GFP signal. Although AF594-WGA was supposed to label only the plasma membrane, a small fluorescence signal was also present in the cytoplasm, as shown in figure 26. In this way, a carefully chosen threshold had to be applied to ensure that pixels from the cytoplasm were not included in the plasma membrane mask. After this, pixels with an AF594-WGA fluorescence intensity value above the threshold were considered to correspond to areas occupied by the plasma membrane, and those with no fluorescence or intensity below the threshold were considered cytosolic. Making the pixel correspondence to the SNAP-25-GFP image, it was then possible to calculate the total fluorescence intensity of SNAP-25-GFP molecules bound to the membrane and inside the cell. Consequently, the fraction of SNAP-25 bounded to the plasma membrane at each 2BP incubation time

was obtained, allowing us to monitor the change in protein localization induced by the inhibition of palmitoylation (figure 27).

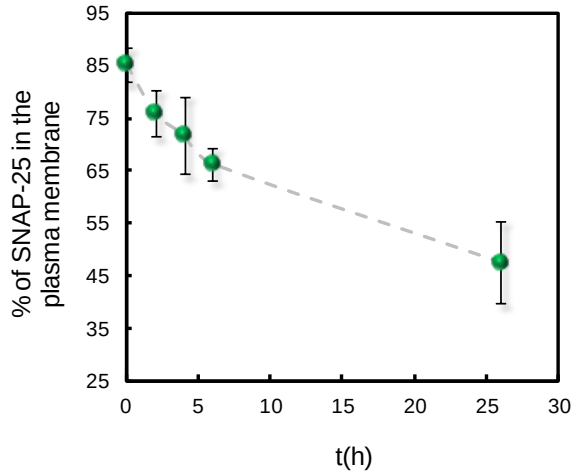

Figure 27. Percentage of SNAP-25-GFP on the plasma membrane of PC12 cells, under different periods of exposure to the palmitoylation inhibitor 2BP (50 μM).

As shown in figure 27, in non-treated PC12 cells, almost all SNAP-25 , (85%) was anchored to the plasma membrane. 2BP exposition of PC12 cells progressively drove the protein to detach from the membrane and concentrate in the cytosol, while some protein bound to intracellular organelles. After 26h of exposure to 2BP, the percentage of SNAP-25 molecules attached to the plasma membrane decreased around 40%, confirming that palmitoylation plays an important role in its sorting to the membrane. This is in disagreement with biochemical studies using radioactive palmitate that showed that chemical removal of the palmitate did not release the protein from the membrane fraction of the cells (Lane and Liu, 1997;Gonzalo and Linder, 1998;Vogel et al., 2000).

Still, 2BP was not able to completely abolish SNAP-25's membrane localization, and even after 26h of treatment we still observed 47% of the protein anchored to the membrane. Considering that 50 μM of the inhibitor was more than enough to block all newly-synthesized PAT enzymes, and that the palmitoylation turnover of SNAP-25 in the membrane was reported to be around 3 hours (Lane and Liu, 1997), the anchoring of SNAP-25 to the plasma membrane must be maintained by another mechanism. Syntaxin incorporated in the plasma membrane has been suggested to be responsible for SNAP-25 membrane anchoring before palmitoylation (Vogel et al., 2000). These results further support this hypothesis. Additionally, it is likely that as a consequence of

SNAP-25 overexpression, the syntaxin-pathway for membrane targeting is not able to sustain such large degree of transport and a significant fraction of the protein remains cytosolic. The rearrangement of $PI(4,5)P_2$ under a fully depalmitoylated SNAP-25 population will be studied in the future.

3.3. Studies in membrane model systems

In parallel with the live cells studies, experiments using membrane model systems were also carried out with the final goal of characterizing the distribution of PI(4,5)P_2 molecules on a simpler system whose composition we can fully control. We chose to use GUVs as our membrane model since they are the model system that best mimics the cellular plasma membrane, as explained before (see section 1.2.1. in the Introduction chapter). However, to acquire confocal images and GUV projections with high enough quality to address PI(4,5)P_2 distribution, it is essential that vesicles remain fully immobile during data acquisition. This is also particularly important for single molecule measurements such as Fluorescence Correlation Spectroscopy (FCS) studies. Since it is our goal in the future to conduct such measurements in this system, it was important to optimize a procedure for GUV immobilization.

Immobilization of GUVs is most often achieved by including biotinylated lipids in the liposomes (Walde et al., 2010). These will then be able to bind with great affinity to an avidin-coated surface. However, the effect of this type of immobilization on the properties of GUVs has not been addressed in detail. Possible effects of the used immobilization method on liposome shape or especially on lipid domain distribution remain unexplored. Here, were aimed to i) understand how immobilization can influence GUV properties and, ii) optimize the immobilization procedure in order to minimize those effects.

3.3.1 Optimization of an immobilization procedure for GUVs

To carry out these experiments, GUVs were prepared with two different lipid compositions: POPC:Chol:PSM (1:1:1) and DOPC:DPPC (1:1), corresponding to liquid ordered/liquid disordered (lo/ld) and gel/fluid (g/f) phase coexistence, respectively. In the lo/ld mixture we expected to observe GUVs with ~85% of lipids in lo phase at 23 ºC (de Almeida et al., 2003), while only ~25% of gel phase is expected to coexist with the fluid phase in g/f GUVs at the same temperature (Schmidt et al., 2009).

The partition coefficient (K_p) of Rho-DOPE between lo/ld phases in POPC:Chol:PSM (1:1:1) is 0.28 (de Almeida et al., 2005), meaning that this probe exhibits 3.6 times preference to ld phase. For this reason, Rho-DOPE was used as a

label of liquid disordered phases at a ratio to total lipid content of 1:500. NBD-DPPE on the other hand has a K_p between gel/fluid phases of 3,68 (Silva et al., 2007), meaning that the probe has a preference for the gel phase. This lipid probe was used as a label for rigid phases at a 1:250 probe/lipid ratio. The concentration used for this lipid in the liposomes was 2-fold higher than for Rho-DOPE due to quantum yield differences between the Rhodamine and the NBD fluorophores.

Three different biotinylated lipids were incorporated in the vesicles to achieve immobilization: DOPE-Cap-biotin (figure 28a), DPPE-Cap-biotin (figure 28b) and DPPE-biotin (figure 28c), at a biotinylated lipid:total lipid ratio that varied from $1:10^7$ to $1:10^5$. Controls without biotinylated lipid were also prepared for each lipid mixture.

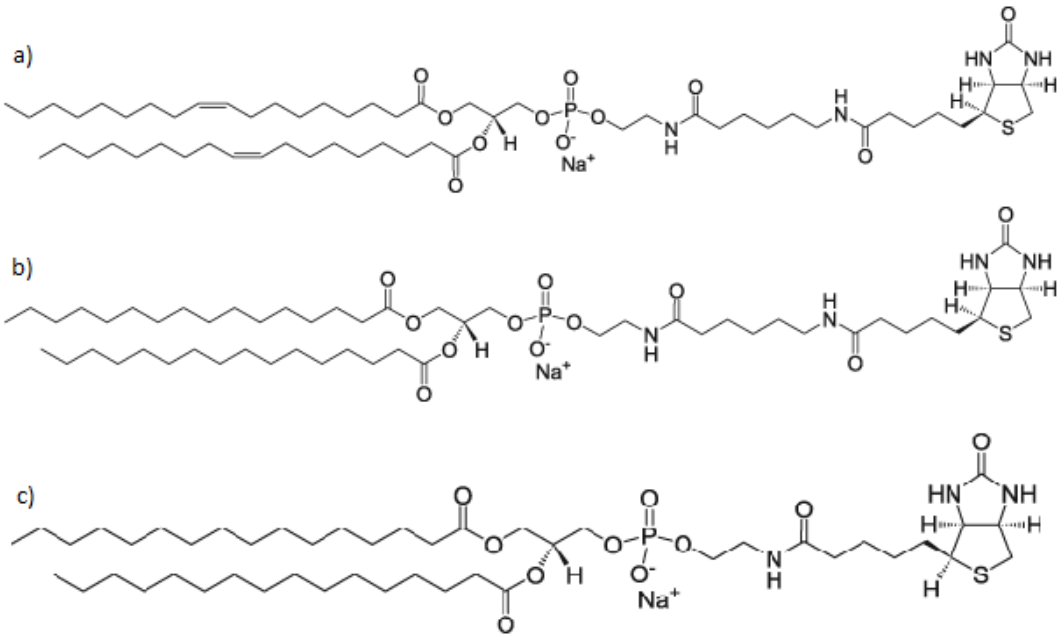

Figure 28. Biotinylated lipids structures. a) DOPE-Cap-biotin; b) DPPE-Cap-biotin; c) DPPE-biotin.

Examples of the images acquired as previously described (see section 2.6.4) are presented in figure 29.

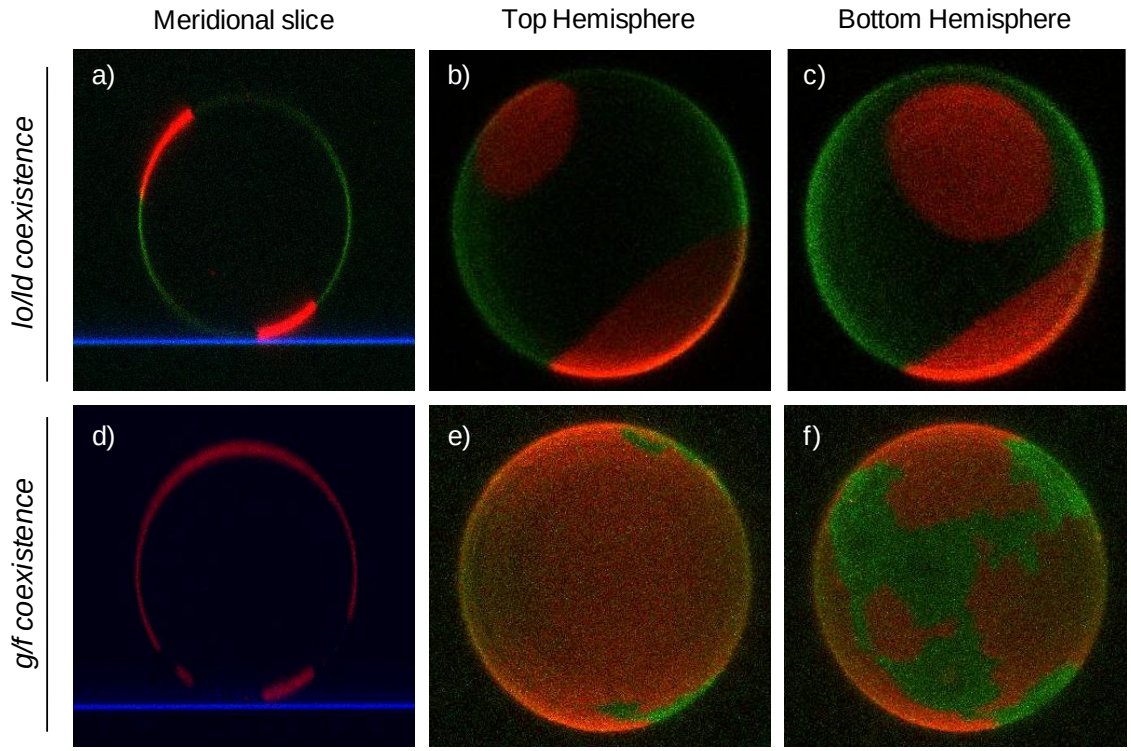

Figure 29. Example of acquired images from GUVs: the meridional slice image (a, d); the top hemisphere projection (b, e); the bottom hemisphere projection (c,f). These specific vesicles were composed of (a, b, c) POPC:Chol:PSM (1:1:1) and (d, e, f) DOPC:DPPC (1:1), with DOPE-Cap-biotin (1:10^6) and DPPE-Cap-biotin (1:10^6), respectively. For each slice, excitation was first performed at 458 nm, and emission was collected at 480-530 nm (NBD-DPPE channel in green) and, in the meridional slice, 458 nm (reflection channel in blue). A second excitation was then performed to image Rho-DOPE fluorescence (red), exciting molecules at 514 nm and acquiring emission at 530-650 nm. NBD-DPPE and Rho-DOPE were present at 1:250 and 1:500 probe/lipid molar ratio.

3.3.1.1 POPC:Chol:PSM (1:1:1) – Liquid ordered/liquid disordered phase coexistence GUVs

We started by incorporating different amounts of DOPE-Cap-biotin in the lipid mixtures to optimize the concentration of biotinylated lipid to be used in the following experiments. We had to take into account that:

i) Large amounts of biotinylated lipid are expected to lead to an excessive degree of adsorption to the surface, ultimately leading to vesicle collapse;
ii) Small quantities of PE-biotin molecules could be insufficient to fully immobilize the vesicles on the surface.

By studying the vesicles using confocal fluorescence microscopy, and by monitoring the degree of vesicle movement and stability at different incubation, we concluded that 1:10^6 molar ratio was the optimal molar ratio of DOPE-Cap-biotin to be

used for POPC:Chol:PSM (1:1:1) GUV immobilization. However, as we could still observe GUVs (*i.e.* vesicles that were immobile and stable for several minutes) in the presence of this biotinylated lipid at a $1{:}10^5$ molar ratio, some experiments were also carried out using this ratio.

To assess the effect of immobilization on GUVs shape, ellipticity values were determined for each imaged vesicle as previously described (section 2.6.4 and figure 14a). The results obtained for different amounts of DOPE-Cap-biotin in the presence of a surface coated with avidin are presented below. Controls without biotinylated lipid and avidin were also included in this study (figure 30).

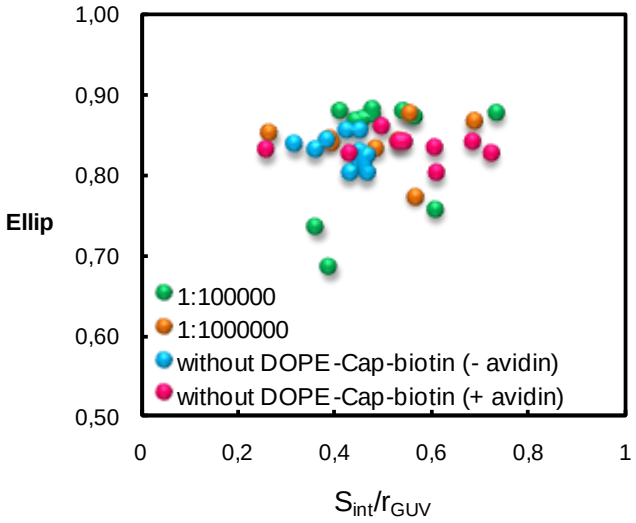

Figure 30. Ellipticity values measured for GUVs composed of POPC:Chol:PSM with a DOPE-Cap-biotin:total lipid ratio of $1{:}10^5$ (●) and $1{:}10^6$ (●), in the presence of avidin coating. Controls without DOPE-Cap-biotin were also performed, in the absence (●) and presence (●) of avidin coating.

The majority of the giant vesicles prepared with DOPE-Cap-biotin at a $1{:}10^6$ biotinylated lipid/total lipid ratio exhibited an ellipticity value around 0.8-0.9, which is very similar to the controls without the biotinylated lipid and avidin (figure 30). However, when DOPE-Cap-biotin quantity was increased 10 fold, vesicles often acquired aberrant shapes due to an extensive flattening at the interaction surface, resulting in ellipticity values more distant from the controls. Together, these results indicate that immobilization of GUVs with $1{:}10^6$ biotinylated lipid:total lipid ratio did not significantly deform GUVs.

Notwithstanding, it is relevant that in the absence of an avidin coating of the chamber, the interaction of vesicles with the surface seemed to be highly restricted,

reducing the spreading of S_{int}/r_{GUV} values. In other words, the lipid membrane does not adsorb to the surface. Also, this effect was found to be insensitive to DOPE-Cap-biotin's presence as it was expected (figure 30).

We next focused on the effect of GUV immobilization on the surface distribution of lipid domains. The obtained $f(lo)$ values for each set of experimental conditions are presented in figure 31 and resumed in table 1.

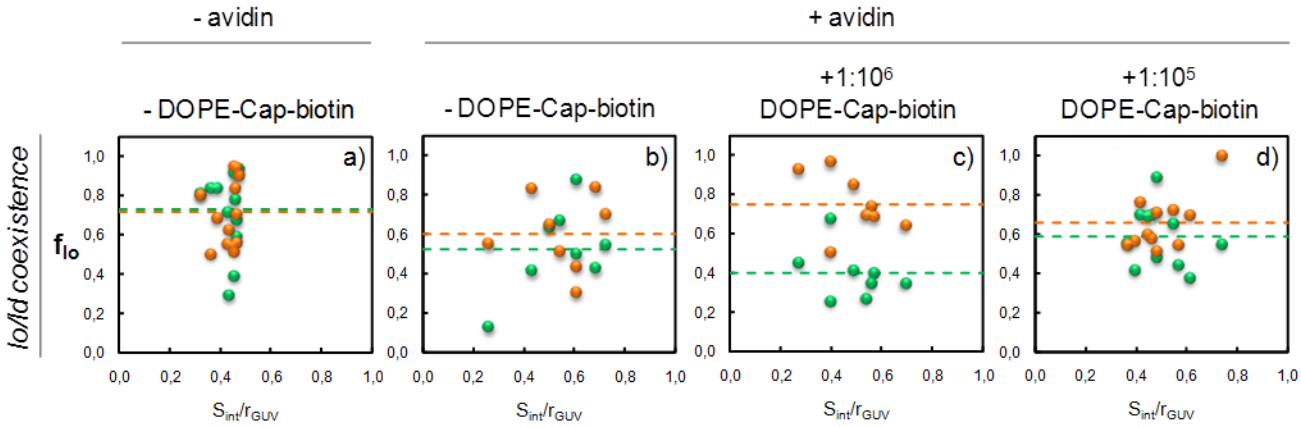

Figure 31. Comparison of liquid ordered phase fractions ($f(lo)$) between the bottom (●) and the top (●) hemispheres of each GUV. Vesicles were composed by POPC:Chol:PSM (1:1:1). Lipid mixtures were prepared without (a,b) or including a 1:10^6 (c) and 1:10^5 (d) DOPE-Cap-biotin/total lipid molar ratio. Experiments b, c and d were carried out in the presence of an avidin-coated surface. The dashed lines are just a guide to the eye and correspond to the mean fraction values obtained in each GUV hemisphere.

Table 1. Mean liquid ordered fraction values in the top hemisphere (*Top Hs*), bottom hemisphere (*Bottom Hs*) and interaction length (S_{int}) of POPC:Chol:PSM composed GUVs. Mixtures were prepared with DOPE-Cap-biotin, DPPE-Cap-biotin and DPPE-biotin at different molar ratios (1:10^7 to 1:10^5). Controls without any biotinylated lipid were also performed, in presence and absence of the avidin-coated surface. *n* is the number of GUVs measured for each set of experimental conditions.

Biotinylated lipid	PE-biotin:lipid molar ratio	avidin-coated surface	*n*	f(lo)		
				Top Hs	*Bottom Hs*	S_{int}
-	-	-	12	0,72 ± 0,17	0,73 ± 0,21	0,98 ± 0,07
-	-	+	8	0,60 ± 0,18	0,53 ± 0,27	0,49 ± 0,48
DOPE-Cap-biotin	1:10^6	+	8	0,75 ± 0,15	0,40 ± 0,13	0,08 ± 0,14
	1:10^5	+	11	0,66 ± 0,15	0,59 ± 0,15	0,57 ± 0,29
DPPE-Cap-biotin	1:10^6	+	5	0,65 ± 0,31	0,76 ± 0,26	0,86 ± 0,11
DPPE-biotin	1:10^7	+	9	0,82 ± 0,20	0,79 ± 0,17	1,00 ± 0,00
	1:10^6	+	8	0,78 ± 0,22	0,77 ± 0,20	0,56 ± 0,40

Before comparing the lo fractions present in each hemisphere, we can already observe that the standard deviation for phase fraction values are high. This is a result of the electroformation process which is known for generating very heterogeneous populations of vesicles (Morales-Penningston et al., 2010). For this reason, measurements for each condition studied included data from different electroformations, performed at different days. In this way, possible artifacts originating from one "bad experiment" are easily identified. This heterogeneity might also explain why the recovered values of f(lo) in the absence of any kind of immobilization ($f(lo)$ = 0,72/0,73; table 1) are about 10% lower than the value reported for a typical POPC:Chol:PSM 1:1:1 mixture ($f(lo)$ = 0,85) (de Almeida et al., 2003).

In addition, we can conclude from figure 31 that the obtained values for $f(lo)$ in the absence of avidin coating were generally higher than in the presence of surface coating with this protein, particularly for the bottom hemisphere in contact with the solid surface. This means that imaging GUVs over an avidin-coated surface creates a bias for vesicles with lower liquid ordered phase fractions. As it is clear from figure 31, interaction with the coated surface led to partial adsorption of the vesicle even in the absence of biotinylated lipid (larger S_{int}/r_{GUV} values).

Through analysis of figure 31a, we can immediately conclude that, if no immobilization procedure is used, the interaction with the uncoated surface did not change the domain distribution within the GUV. On the other hand, the area of the membrane interacting with the coverslip surface was always composed mostly by lo phase ($f(\delta_{lo}) =$ 0,98±0,07). Possibly, since interaction of membranes with solid surfaces is known to decrease the dynamics of the bilayer (Loose and Schwille, 2009), interaction of GUVs with the coverslip surface promotes liquid ordered domain segregation to this less dynamic area.

The effect of avidin coating alone can be perceived in figure 31b. It is clear that interaction with the coated surface led to partial adsorption of the vesicles even in the absence of biotinylated lipid (larger S_{int}/r_{GUV} values). In this case, a small difference in the mean fraction values can be observed. It is certainly possible that vesicles interacting with the avidin coated surface through areas of the membrane in the liquid ordered phase, are less stable and display higher probability of collapse. This would undoubtedly create a bias to lower lo fraction in observed GUVs. The fact that the average lo fraction in the interaction length for this system (49%) was even smaller than the average for the entire vesicles further supports this hypothesis. However, due

to the high standard deviation associated with the mean values, these differences must be compared with some caution.

Conversely, adding small quantities of DOPE-Cap-biotin (figure 31c) dramatically affects hemisphere composition. In fact, liquid ordered phase seemed to be partially excluded from the bottom hemisphere (40%, against the 75 % in the top hemisphere). These results suggest that DOPE-Cap-biotin might significantly favour partition to the liquid disordered phase. In such case, the liquid disordered domains will exhibit significantly higher affinity for the avidin coated surface. When DOPE-Cap-biotin concentration was increased to a biotinylated lipid:total lipid ratio of $1:10^5$ (figure 31d), this effect was abolished and the mean fraction values were almost identical to those obtained for the control without DOPE-Cap-biotin in the presence of avidin.

Since DOPE-Cap-biotin was apparently partitioning to more disordered phases in the membrane, we wanted to confirm that GUVs actually interacted with the avidin-coated surface through the ld phase.

In table 1, the obtained mean lo fractions in the interaction length are presented for each set of experimental conditions. Given that DOPE-Cap-biotin partitions mostly to less rigid phases of the membrane, when small quantities were added ($1:10^6$) to lo/ld vesicles, the low concentration of biotinylated lipid in the lo phase was not enough to promote an efficient interaction with the avidin surface. This explains the virtual absence of lo phase in the interaction length of the GUV (8%) which is much lower than the percentage of lo fraction in the total vesicle (around 60%). When we increased the biotinylated/total lipid molar ratio ($1:10^5$), as a consequence of the increase in concentration of biotinylated lipids in the ordered domains, the different lipid phases had more comparable affinities for interaction with the avidin coated surface. Consequently, similar distributions of lo and ld phases in the interaction length were observed ($f(\delta_{lo}) = 0{,}57 \pm 0{,}29$).

Looking at DOPE-Cap-biotin's structure (figure 28a), we can assign the observed effects to one (or both) of its following characteristics:

i) Presence of a Cap that links the acyl chain of the phospholipid to biotin. The Cap functions as a spacer that confers more flexibility to the lipid head and separates it from the GUV's membrane; this increases the distance between the vesicle and the surface, minimizing possible effect on the distribution of the lipid in the membrane;

ii) The acyl chains (oleic acid). The acyl chain composition dictates the location of the lipid within lipid domains. In this case, the presence of one oleoyl chain promotes preferentially the partition of DOPE-Cap-biotin to the fluid phases of the membrane.

To understand how these two characteristics influence the studied GUV properties, we repeated the experiments incorporating two different biotinylated lipids:

i) DPPE-Cap-biotin (Figure 28b) – it presents the same Cap spacer, but the palmitoyl acyl chains should promote partition to more rigid phases of the membrane;
ii) DPPE-biotin (Figure 28c) – also presents palmitoyl acyl chains, but does not have a Cap linker.

We started by using a biotinylated lipid:total lipid ratio of $1:10^6$, as it was determined for DOPE-Cap-biotin to correspond to a higher stability of immobilized GUVs (lower rates of collapse in the surface). However, for DPPE-biotin we still observed significant collapse of the giant vesicles on the surface. For this reason, we also used a 10x-lower molar ratio of this biotinylated lipid, since it proved to be enough for immobilization.

Images were obtained as formerly described and the analysis was also carried out as explained. Thus, meridional slice images of each GUV were used once more to adjust an ellipse to the vesicles and calculate ellipticity values. The obtained results are presented in the following figure.

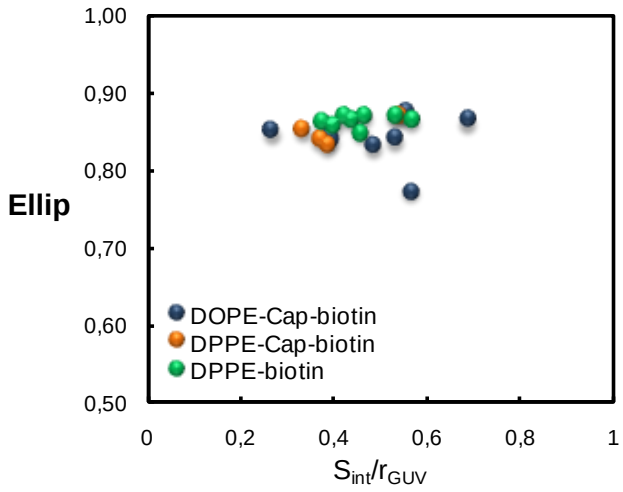

Figure 32. Ellipticity values of GUVs composed of POPC:Chol:PSM with DOPE-Cap-biotin (●), DPPE-Cap-biotin (●) or DPPE-biotin (●) at a $1:10^6$ molar ratio, in the presence of an avidin-coated surface.

In figure 32, one can see that $Ellip$ values are very close to each other (between 80 and 90%). Comparing with the values obtained for the controls without biotinylated lipid and avidin (figure 30), we can confirm that all three lipids do not affect GUVs shape.

With respect to domain distribution, the obtained fractions of liquid ordered phase are presented in table 1. Notice that, for DPPE-Cap-biotin, no significant difference of domain distribution between hemispheres was observed (figure 33). However, a larger population of GUVs must be analyzed to allow for any definitive conclusions.

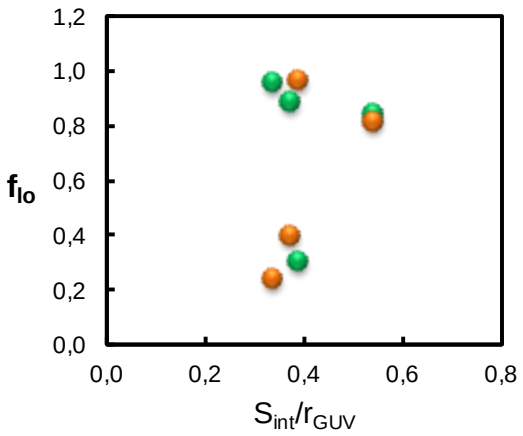

Figure 33. Comparison of liquid ordered ($f(lo)$) phase fractions between the bottom (●) and the top (●) hemispheres DPPE-Cap-biotin containing vesicles. GUVs were composed by POPC:Chol:PSM (1:1:1) including a 1:10^6 DPPE-Cap-biotin:total lipid molar ratio and the experiment was carried out in the presence of an avidin-coated surface.

Also, for DPPE-biotin, and even at lower concentrations, no difference was observed in domain distribution between the hemispheres. This indicates that differences in partition preferences of biotinylated lipids can actually induce different effects on lipid domain distribution. For both biotinylated lipids with two palmitoyl acyl-chains, fractions of lo phase for both hemispheres presented values above the control without immobilization (without biotinylated lipid). The fraction values of lo phase in the interaction length are also presented in table 1. As we can see, the use of DPPE-biotinylated lipids completely inverted the effect observed for DOPE-Cap-biotin. In GUVs with DPPE-Cap-biotin, a small preference for interaction with the surface through lo domains was observed, since the mean fraction value (86%) is slightly above the value determined for the entire GUV. In DPPE-biotin containing vesicles, this effect was more pronounced when 1:10^7 molar ratio was used, having all GUVs binding to the interaction surface through the liquid ordered phase. When a higher amount of

DPPE-biotin wass used (1:10^6), the fraction (56%) dropped to a value closer from the obtained for the control with surface coating (without biotinylated lipid) (49%), similar to the one observed for DOPE-Cap-biotin at 1:10^5 ratio.

Apparently, some enrichment of both DPPE-biotinylated lipid in the ordered lipid phase takes place. However, since liquid ordered phase in this mixture is in large majority (85%), no clear differences can be identified between GUV hemispheres for lo fractions. Still, differences can be clearly appreciated for the interaction length. The preference of DPPE-biotinylated lipids for lo is not surprising, since DPPE has been often associated with partition to ordered domains.

DOPE-Cap-biotin partition

Although this data clearly suggests that DOPE-Cap-biotin and the DPPE-biotinylated lipids have preferential partition to different lipid environments, we cannot quantify this from the domain distribution in immobilized GUVs. In order to achieve this, we designed a FRET experiment, where the donor was *trans*-parinaric acid (*t*-PnA), a membrane probe with nearly identical partition between liquid ordered and liquid disordered phases ($Kp^{lo/ld}$ = 0,88; (Silva et al., 2007)) but different quantum yields in each environment. The acceptor was extravidin-FITC, which binds to the membrane only in the presence of biotinylated lipid (see figure 34 for spectral overlap). In this way, and using analytic formalisms for FRET to a distribution of acceptors, we can quantify the concentrations of extravidin-FITC in each lipid environment from the FRET data.

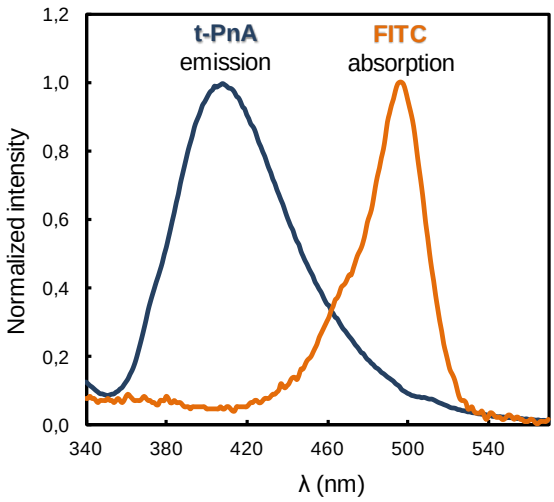

Figure 34. Spectral overlap of the spectra of *t*-PnA (blue) emission and FITC absorption (orange). Both intensities are normalized to the maximum intensity value.

As determined from a published quantum yield (Q) value and lifetime weighted quantum yields, Q_{t-PnA} = 0,04 in POPC membranes and 0,12 in liquid ordered phases (Sklar et al., 1977;Mateo et al., 1993;Mateo et al., 1995). According to equation 2, R_0 values should be different in each lipid environment, and for identical acceptor densities, FRET efficiencies are higher for liquid ordered domains. R_0 values were calculated on the basis of these quantum yields and of the spectra from figure 34. An extinction coefficient of 84 000 was used for FITC (as given by the manufacturer), and the value of k^2 =2/3 was used for the orientation factor. The latter value corresponds to completely randomized relative orientations for donors and acceptors and due to the elevated rotational freedom in this environment, is a good approximation for most fluorophores in fluid membranes. Additionally, the acceptors are found outside the membrane in the bound protein, further contributing to randomization of the orientations. R_0 values were determined to be 24 and 29 Å for liquid disordered and liquid ordered domains, respectively.

The FRET contribution from energy transfer to acceptors randomly distributed in a plane at a fixed distance to the donor plane is given by (Davenport et al., 1985) as:

$$\rho_{FRET}(t) = exp\left\{-2\sigma\pi l^2 \int_0^1 \frac{1-\exp\left(-tb^3\alpha^6\right)}{\alpha^3} d\alpha\right\} \qquad \text{Eq. 27}$$

where $b = (R_0^2/l)^2 \tau_D^{-\frac{1}{3}}$, σ is the acceptor density, l is the distance between the plane of donors and acceptors, and $\tau_D$is the donor lifetime. Donor decay in the presence of acceptors ($i_{DA}(t)$) is given by:

$$i_{DA}(t) = i_D(t) \cdot \rho_{FRET}(t) \qquad \text{Eq. 28}$$

where $i_D(t)$ is the donor decay in the absence of FRET. From the integration of simulated decays based on equations 27 and 28 it is then possible to calculate FRET efficiencies from equation 4.

In our analysis we assumed that all *t*-PnA is located at the same plane in the bilayer. *t*-PnA fluorophore is known to be buried in the membrane (Castanho et al., 1996). Since R_0 values are small, and acceptors bind only to the external leaflet, donors in the external leaflet of the liposomes will be at shorter distances to the acceptors than donors in the internal leaflet, and the contribution to FRET will arise

mainly from the outer donors. The position of the acceptor is harder to estimate since each extravidin molecule presents approximately 4 copies of FITC and these should be distributed around the protein. In order to estimate an average position for the acceptors in extravidin, we conducted a FRET experiment in POPC LUVs with 1:100 DOPE-Cap-biotin and 1:200 *t*-PnA, for different concentrations of extravidin-FITC. DOPE-Cap-biotin was always present in excess amounts (at the highest extravidin concentration the ratio of DOPE-Cap-biotin/extravidin was 12). For these conditions, DOPE-Cap-biotin is expected to have a completely homogeneous distribution in the bilayer, as so does bound extravidin-FITC. Fitting equation 27 and 28 to experimental FRET data (figure 35), while using a value of 24 Å for the R_0 and 68 Å^2 as the area of a POPC molecule (Kucerka et al., 2005), allowed us to recover a value of 23 Å for the distance between the donors in the external leaflet and acceptors in this system. FRET between donors in the internal leaflet and acceptors is not negligible and was also taken into account in the analysis by assuming that the distance of acceptors to these donors was 20 Å larger than for outer donors.

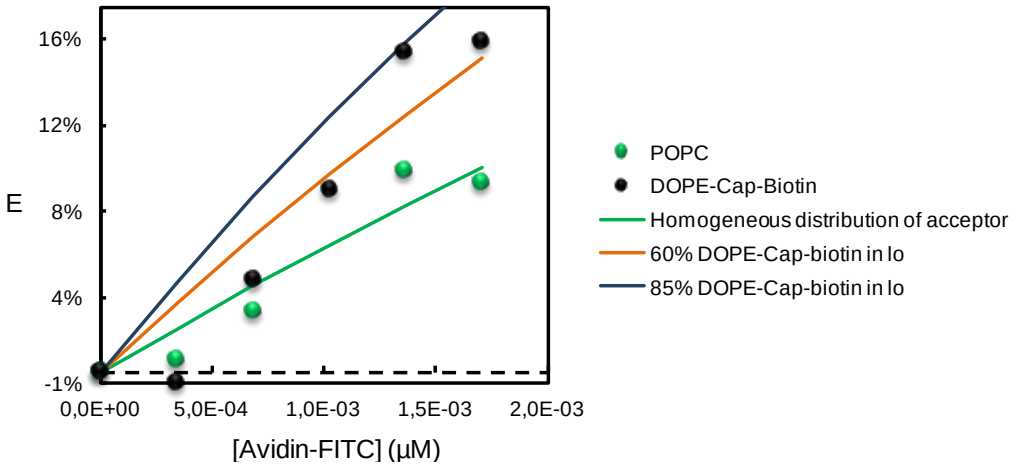

Figure 35. Fitting of different models of acceptor distribution to the experimentally obtained FRET efficiencies for the *t*-PnA/Extravidin-FITC donor/acceptor pair at different acceptor concentrations. A model based on homogeneous acceptor distribution (eq. 27) was fitted (green trace) to the data obtained in POPC bilayers (green data points). 23 Å and 43 Å were recovered as the distance between the 2 planes of donors (located in the inner and outer leaflet of the liposome) and the average acceptor plane. Using these distances, a more complex model assuming different concentrations of acceptors at different lipid phases (eq. 29) was fitted (orange trace) to the experimental data obtained in the POPC:SM:CHOL 1:1:1 mixture (dark data points). The recovered concentration of acceptors in the liquid disordered phase was 3,78 times higher than the concentration in the liquid ordered phase and the $K_p^{lo/ld}$ of DOPE-Cap-biotin/extravidin complexes was determined to be 0,26. Note that the model assuming identical concentrations for the acceptor in lo and ld domains (dark trace) does not accurately describes the experimental data.

Since we now have a better description of FRET between *t*-PnA and the labelled extravidin, we can now fit our model to the FRET results in the ternary system POPC:Chol:PSM 1:1:1. In this case, we now have:

$$i_{DA}(t) = f(lo)\, i_D^{lo}(t) \cdot \rho_{FRET}^{lo}(t) + f(ld)\, i_D^{ld}(t) \cdot \rho_{FRET}^{ld}(t) \quad \text{Eq. 29}$$

where $i_D^{lo}(t)$ and $i_D^{ld}(t)$ are the donor decays in liquid ordered and liquid disordered domains. ρ_{FRET}^{lo} and ρ_{FRET}^{ld} are the FRET contributions in each phase, and these are dependent on the protein concentration in the two environments. Since we assume equal preference of donor molecules to lo and ld domains, the fraction of donors in each phase are equal to f(lo) and f(ld). Additionally, it is assumed that domains are large enough (domain size >> R_0) so that FRET between donors in one phase to acceptors in a different phase is negligible (de Almeida et al., 2005). This is clearly true for this composition as observed in the confocal data. From the comparison of acceptor concentrations in the two phases, a partition coefficient for the DOPE-Cap-biotin/Extravidin complexes can be recovered using equation 30:

$$K_p^{lo/ld} = \frac{\frac{N_A^{lo}}{N_L^{lo}}}{\frac{N_A^{ld}}{N_L^{ld}}} \quad \text{Eq. 30}$$

where N_A^{lo} and N_A^{ld} are the number of molecules of acceptor in the liquid ordered and liquid disordered phases, and N_L^{lo} and N_L^{ld} are the number of molecules of lipids in the liquid ordered and liquid disordered phases, respectively.

Fitting this model to our data (figure 35), we recovered a $K_p^{lo/ld}$ = 0,26 for the complexes DOPE-Cap-biotin/Extravidin, demonstrating strong preference for the liquid disordered environment, as expected. It is possible that the value of $K_p^{lo/ld}$ for the biotinylated lipid alone could be somewhat smaller than this, since it is known that multiple lipid modifications in a protein has a significant effect on protein diffusion and in some cases induces partition to more ordered domains. However, the value recovered is almost identical to published values for the DOPE-Rho membrane probe ($K_p^{lo/ld}$= 0,26; (de Almeida et al., 2005)).

From these results we can conclude that the acyl chain of the biotinylated lipid dictates the lipid phase that interacts with the surface, while the presence of a linker to the biotinyl group is apparently only relevant for vesicle stability. A partition coefficient was recovered for the complex DOPE-Cap-biotin/Extravidin in a lo/ld mixture, confirming strong selectivity for liquid disordered phases. In the future, the same

methodology will be applied to the other biotinylated lipids to recover the correspondent partition coefficients.

Additionally, reorganization of lipid domain distribution was dependent on the concentration of biotinylated lipids used. Of great relevance was the observation that, even in the absence of biotinylated lipids, the nature of the solid support (coated or uncoated with avidin) had a non negligible influence on domain distribution inside GUVs.

3.3.1.2 DOPC:DPPC (1:1) – Gel/fluid phase coexistence GUVs

In order to evaluate if biotinylated lipids induce similar effects when using different types of phase coexistence in GUVs, we performed the same experiments with the DOPC:DPPC (1:1) mixture. As explained, this composition results in vesicles with gel/fluid coexistence, where gel phase is present in around 25%.

Once more, we confirmed that the 1:10^6 molar ratio of biotinylated lipid guarantees immobilization while ensuring vesicle stability. GUVs shape was once again appreciated through the comparison of ellipticity values. Vesicles with 1:10^5 DOPE-Cap-biotin, together with controls without biotinylated lipid (in absence and presence of avidin) were also analyzed and the results are presented in figure 36.

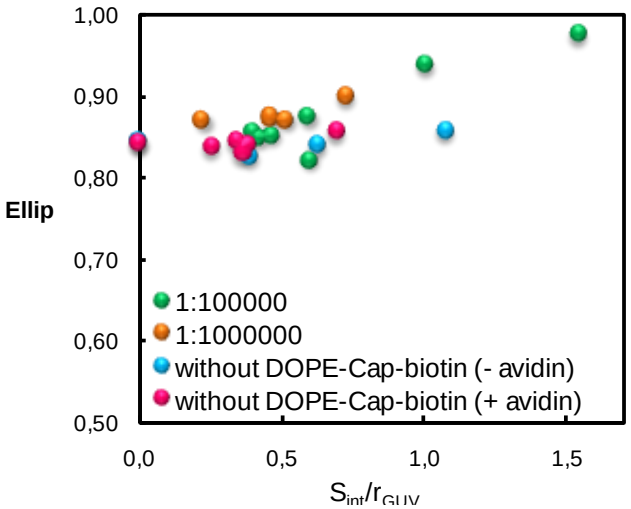

Figure 36. Ellipticity values of GUVs composed of DOPC:DPPC (1:1) with a biotinylated lipid/total lipid ratio of 1:10^5 (●) and 1:10^6 (●), in the presence of avidin coating. Controls without DOPE-Cap-biotin were also analyzed, in the absence (●) and presence (●) of avidin coating.

Like in the ternary mixture, ellipticity values were generally between 80 and 90% in both the controls and for lower concentrations of DOPE-Cap-biotin molecules (1:10^6 molar ratio). However, when this quantity was increased (1:10^5), anomalous GUVs shapes were once more observed, as a result of the flattening of the interaction surface that precedes the collapse over the surface (figure 37). Thus, g/f GUVs can be immobilized without changing their shape and stability if low amounts of biotinylated lipid are applied.

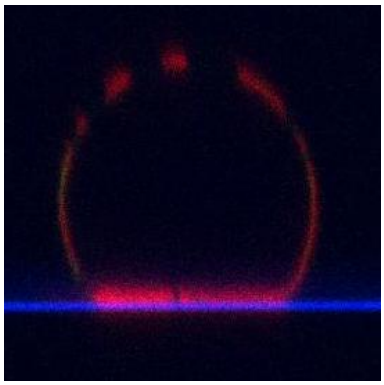

Figure 37. Meridional slice image of a DOPC:DPPC (1:1) GUV with the characteristic interaction surface flattening that precedes the collapse. 1:10^5 molar ratio of DOPE-Cap-biotin was used, and the surface was coated with avidin.

In relation to domain distribution within the hemispheres, gel fraction values were calculated and are presented in figure 38. The mean fraction values are summarized in table 2.

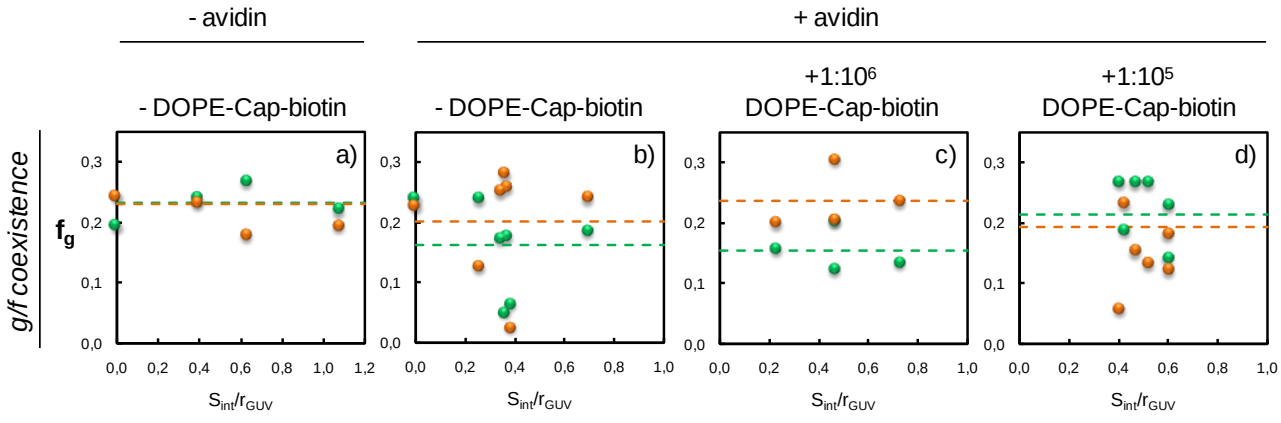

Figure 38. Comparison of gel phase fractions ($f(g)$) between the bottom (●) and the top (●) hemispheres of each GUV. Vesicles were composed by DOPC:DPPC (1:1). Lipid mixtures were prepared without (a,b) or including a 1:10^6 (c,) and 1:10^5 (d) DOPE-Cap-biotin/total lipid molar ratio. Experiments b, c and d were carried out in the presence of an avidin-coated surface. The dashed lines are just a guide to the eye and correspond to the mean fraction values obtained in each GUV hemisphere.

Table 2. Mean gel phase fraction values in the top hemisphere (*Top Hs*), bottom hemisphere (*Bottom Hs*) and interaction lentgh (S_{int}) of DOPC:DPPC composed GUVs. Mixtures were prepared with DOPE-Cap-biotin, DPPE-Cap-biotin and DPPE-biotin at different molar ratios ($1:10^6$ to $1:10^5$). Controls without any biotinylated lipid were also performed, in presence and absence of the avidin-coated surface. *n* is the number of GUVs measured for each set of experimental conditions.

Biotinylated lipid	PE-biotin:lipid molar ratio	avidin-coated surface	*n*	f(g)		
				Top Hs	*Bottom Hs*	S_{int}
-	-	-	5	0,23 ± 0,05	0,23 ± 0,03	0,58 ± 0,44
-	-	+	7	0,20 ± 0,09	0,16 ± 0,08	0,06 ± 0,11
DOPE-Cap-biotin	$1:10^6$	+	4	0,24 ± 0,05	0,16 ± 0,04	0,00 ± 0,00
	$1:10^5$	+	9	0,19 ± 0,09	0,21 ± 0,06	0,13 ± 0,21
DPPE-Cap-biotin	$1:10^6$	+	11	0,25 ± 0,10	0,31 ± 0,07	0,33 ± 0,42
DPPE-biotin	$1:10^6$	+	10	-	-	0,33 ± 0,15

Domain distribution in vesicles with small amounts of DOPE-Cap-biotin (figure 38) was clearly sensitive to the immobilization method. In this case, immobilization seems to direct larger fractions of fluid phase into the bottom hemisphere (84%, against 76% in the top hemisphere). However, since there is only 20% of gel phase in the GUVs, partition of DOPE-Cap-biotin to the fluid phase induced only minor changes in hemisphere composition. With the lipid mixture used to study effects on the lo/ld phase coexistence, changes in lipid disordered domain distribution were more significant because the lipid phase with greater concentrations of biotinylated lipid was present at a lower fraction.

When we increased DOPE-Cap-biotin's concentration up to $1:10^5$ molar ratio, redistribution of domains was no longer observed.

To better understand the observed effects, gel fractions in the interaction surface were again calculated and the mean fraction values are also presented in table 2. In the case of g/f vesicles, both DOPE-Cap-biotin concentrations seemed to promote interaction with the coated coverslip surface through fluid. It is likely that the partition of DOPE-Cap-biotin to gel domains is even lower than to lo domains, decreasing the probability of an effective contact with the solid surface through DOPE-Cap-biotin molecules located in this phase. When small amounts of DOPE-Cap-biotin were used, concentrations of the biotinylated lipid in gel domains was probably so low that no GUV observed had any fraction of gel phase in the area interacting with the coverslip surface.

Once more, in the absence of avidin coating in the coverslip surface, the fraction of the more rigid phase in the interface area ($f(\delta_g) = 58\,\%$) was highly increased relative to the rest of the vesicles (f(g) = 23%). We believe that in the same way as for the ternary mixture, this effect is induced by the decrease in dynamics associated with adsorbing to the coverslip surface. When avidin was used but no biotinylated lipid was included in the lipid mixture, the opposite effect was observed.

We also repeated the experiments with DPPE-Cap-biotin and DPPE-biotin in this mixture. A biotinylated lipid/total lipid ratio of $1{:}10^6$ was sufficient to immobilize the GUVs and no excessive collapse in the surface was detected.

Ellipticity values were then obtained as previously described and are shown in the following figure.

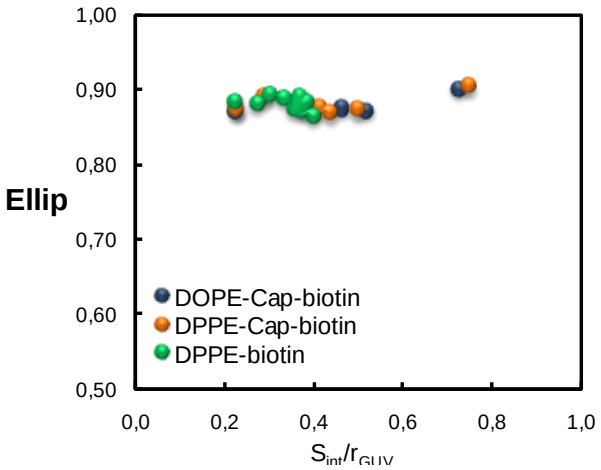

Figure 39. Ellipticity values of GUVs composed by DOPC:DPPC with DOPE-Cap-biotin (●), DPPE-Cap-biotin (●) or DPPE-biotin (●) at a $1{:}10^6$ molar ratio, in the presence of an avidin-coated surface.

Through observation of figure 39, it was clear that the presence of biotinylated lipids did not change vesicle shape. Ellipticity values of 80-90 % were very similar to those obtained for the controls without PE-biotin molecules (figure 36).

The projections constructed from the xy slices were once again used to calculate the gel fractions in the different hemispheres of each vesicle. The obtained results are exhibited in table 2. Notice, however, that $f(g)$ values for DPPE-biotin are not presented, since, in all the acquired images, gel and fluid domains were not clearly separated. Therefore, only the effect of different acyl chains from biotinylated lipids in hemisphere composition can be assessed. Considering the results obtained for GUVs immobilized with DPPE-Cap-biotin, we can conclude that there were only minor

differences between hemispheres composition. This is an indication that DPPE-Cap-biotin did not exhibit strong partition to gel domains, distributing between both phases at comparable concentrations. Still, values obtained for the gel fraction in the interaction surface, for DPPE-Cap-biotin and DPPE-biotin, were higher than the gel fraction observed for the entire vesicle, independently of the cap linker. This might reflect some preference of DPPE for more rigid lipid phases. Nevertheless, the obtained value for DPPE-Cap-biotin is associated with a high standard deviation value, which reflects the great heterogeneity in GUV population.

In summary, in gel/fluid coexistence GUVs, the effects induced by immobilization with biotinylated lipids were apparently not so dramatic as observed in the POPC:Chol:PSM ternary mixture. This was likely due to the absence of a high preference for gel domains by the DPPE-Cap-biotin and DPPE-biotin lipids, and in the case of DOPE-Cap-Biotin, due to the presence of large fractions of fluid phase.

3.3.2 Effect of calcium concentration on the membrane distribution of PI(4,5)P_2 in model membranes

LUVs composed of POPC were prepared with 0, 0.1, 0.25, 0.5, 1 and 2% of TopFluor-PI(4,5)P_2 to characterize the emission properties of the fluorescently labelled phospholipid. The TopFluor fluorophore presented a fluorescence emission maximum at 503 nm when excited at 485 nm, and its emission spectra were found to be independent of its concentration (data not shown). In figure 40, the fluorescence intensity of TopFluor-PI(4,5)P2 is plotted as a function of its effective concentration in the lipid vesicles.

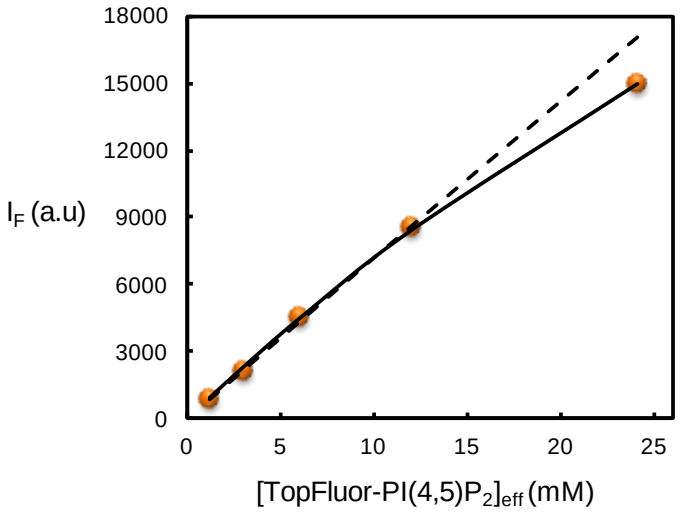

Figure 40. Fluorescence intensity values (corrected for inner filter effects) as a function of TopFluor-PI(4,5)P_2's concentration in LUVs composed of POPC. The TopFluor fluorophore was excited at 485 nm while fluorescence intensities were measured at the emission spectra maximum (505 nm). Each dot represents the mean value of three independent experiments. Error bars fall within the radius of the data points. The lines are the fits to the experimental results (●) of only the dynamic quenching model (**- - -**) and of the combination of dynamic and sphere of action quenching (**—**) models.

The effective TopFluor-PI(4,5)P_2 concentration values are given by:

$$[Top\ Fluor\ PI(4,5)P_2]_{eff} = \frac{R_{P/L}}{V_{POPC}} \qquad \text{Eq. 31}$$

where $R_{P/L}$ is the probe-to-lipid ratio and V_{POPC} is the volume of one single POPC molecule. To calculate the V_{POPC} value, an area of 68 Å and a length of 19,1 Å were used (Kucerka et al., 2005).

Intensity values were correct for inner filter effects according to (Gauthier et al., 1986).

A slight deviation from a linear relationship was detected for TopFluor-PI(4,5)P_2 concentrations higher than 10-12 mM (figure 40).

The time-resolved fluorescence properties of TopFluor-PI(4,5)P_2 incorporated in POPC LUVs were also studied (see details in Material and Methods, section 2.6.6.2). This fluorophore presented a complex fluorescence decay at all concentrations and it was necessary to use 3 exponentials to accurately fit the experimental decays, as judged from the χ^2 values (table 3). The long and intermediate lifetimes of around 6 ns and 2,5 ns are the predominant components (α_1~0,85 and α_2~0,12, respectively).

Table 3. Time-resolved fluorescence intensity decay parameters of TopFluor-PI(4,5)P_2 incorporated in 100 μM POPC LUVs as a function of its local and effective concentrations. The measurements were carried out at room temperature with λ_{ex} = 460 nm and λ_{em} = 503 nm.

[TopFluor-PI(4,5)P_2] (μM)	[TopFluor-PI(4,5)P_2]$_{eff}$ (mM)	α_1	τ_1 (ns)	α_2	τ_2 (ns)	α_3	τ_3 (ns)	$\bar{\tau}$ (ns)	<τ> (ns)	χ^2
0,1	1,3	0,83	6,11	0,12	2,49	0,05	0,52	5,42	5,88	1,03
0,3	3,2	0,85	6,12	0,12	2,53	0,03	0,59	5,50	5,90	1,04
0,5	6,4	0,83	6,06	0,12	2,29	0,05	0,33	5,32	5,85	0,98
1,0	12,8	0,76	5,92	0,15	2,33	0,10	0,33	4,87	5,64	0,95
2,0	25,6	0,69	5,58	0,20	2,22	0,10	0,36	4,34	5,19	1,03

The non-linear relationship between the fluorescence intensity of TopFluor-PI(4,5)P_2 and its concentration (figure 40) suggests that significant quenching might occur when high concentrations of the probe are present. Initially, we investigated if the non-linearity could be explained exclusively on the basis of a dynamic (or collisional) quenching model (i.e. quenching results only from the collision of diffusing molecules within the membrane). This type of quenching is characterized by a decrease in the quantum yield and lifetime of the fluorophore proportional to the molecule concentration. The contribution of collisional self-quenching to the fluorescence lifetime is given by the Stern-Volmer equation:

$$\frac{\tau_0}{\tau} = 1 + k_q \times \tau_0 \times [F] \qquad \text{Eq. 32}$$

where τ_0 and τ are the lifetimes in the absence and presence of quenching, respectively, k_q is the bimolecular diffusion rate constant and $[F]$ is the concentration of the fluorophore. k_q reflects the quenching efficiency and can be related to the diffusion coefficient (D) through Smoluchowski's equation:

$$k_q = 4\pi N_A \times (2 \times R_c) \times (2 \times D) \times \left[1 + 2 \times R_c/(2 \times \tau_0 \times D)^{1/2}\right] \qquad \text{Eq. 33}$$

where N_A is the Avogadro number and R_c is the collisional radius. The Stern-Volmer plots that correspond to our data are presented in figure 41.

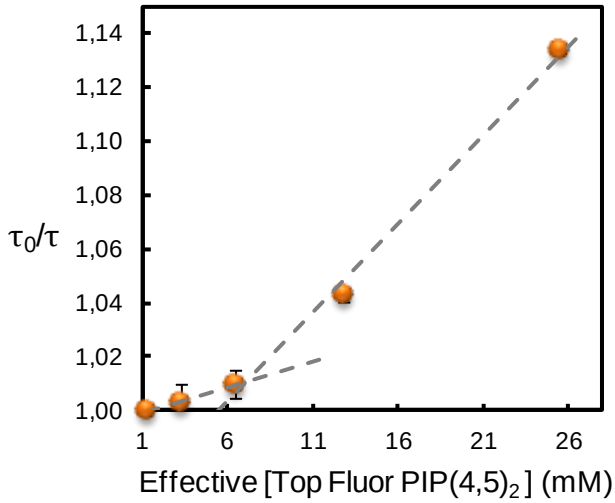

Figure 41. Stern-Volmer plots, representing fluorescence self-quenching of BODIPY at different TopFluor-PI(4,5)P_2 concentrations. Each dot represents the mean value of three independent experiments, with the respective standard deviation bars; The dashed lines are the linear regressions adjusted to both low and high ranges of TopFluor-PI(4,5)P_2 concentration.

In figure 41, we can see that the lifetime does not change linearly with the concentration. In fact, the data can be separated into two ranges presenting different k_q values and, consequently, dissimilar diffusion coefficients. For low concentrations of the fluorophore (figure 41), the lower slope reflects an also lower k_q value (3,23 x 10^8 $M^{-1}s^{-1}$). When TopFluor-PI(4,5)P_2's concentration was increased (figure 41), a higher k_q value was recovered (1,12 x 10^9 $M^{-1}s^{-1}$). Using these values in the Smoluchowski's equation (equation 33), we obtained two different diffusion coefficient values:

i) 1,64 x 10^{-8} $cm^{-1}s^{-1}$ for the lower fluorophore concentrations
ii) 5,91 x 10^{-8} $cm^{-1}s^{-1}$ in the presence of higher concentrations of labelled PI(4,5)P_2 molecules.

Both of these values are consistent with free diffusion in a fluid membrane (Korlach et al., 1999). However, the discrepancy in values for the two concentration ranges can only be explained as a significant increase in the rate of collisions at higher concentrations of the probe. In fact, the slightly higher diffusion coefficient that is observed for high probe concentrations suggests a small tendency for the formation of dimers or other small complexes. In these complexes, collision probability would be increased relative to a fully homogeneous distribution of the lipid probe.

Such type of interactions should also induce static quenching and be detectable in steady-state intensity measurements of the probe fluorescence. In complexes, the probability of occurring non-fluorescent "dark species" due to interactions between

fluorophores at the moment of excitation are dramatically increased. Because these contact pairs are non-fluorescent, static quenching results in a decrease of quantum yield but does not influence the lifetime, as no photons are emitted and the interacting species do not contribute to the fluorescence decay.

Still, even for homogeneously distributed molecules there is a statistically described probability for a fluorophore to be at very close proximity of another at the moment of excitation (statistical contact pairs). For these cases, static quenching can be described through the sphere of action model. The contributions of collisional and sphere of action self-quenching to the fluorescence intensity can be combined in the following equation:

$$I_F = \frac{C \times [F]}{\frac{1}{\tau_0} + k_q \times [F]} \times exp(-V_S \times N_A \times [F]) \quad \text{Eq. 34}$$

where C is a constant and V_s is the sphere of action volume. The sphere of action radius can be obtained by:

$$R_s = \left(V_s / \left(\frac{4}{3} \times \pi\right)\right)^{1/3} \quad \text{Eq. 35}$$

Using equation 34, we fitted both models (only dynamic quenching and the combination of dynamic and static quenching by statistical contact pairs) to the experimental results. In these fittings, we fixed the k_q value to 1,64 x 10^{-8} (obtained for low concentrations of the labelled lipid) and allowed for fluctuation of C and V_s values. The results are shown in figure 40.

Clearly, to correctly describe the intensity variation for the highest concentration of TopFluor we had to apply the model including a static quenching component. A 152 Å sphere radius was recovered, which is much higher than what would be expected for statistical contact pairs (<10 Å).

In this way, at 2% TopFluor-PI(4,5)P_2 a small fraction of the probe population apparently presents some degree of clustering. Such behaviour is not observed when using a NBD-PI(4,5)P_2 probe (Fernandes et al., 2006), possibly indicating that the TopFluor fluorophore might contribute to this self-association in the membrane. TopFluor presents significant similarities to BODIPY fluorophores, and these have been shown to form nonfluorescent dimers under certain conditions (Bergstrom et al., 2002).

Taking all these results into consideration, and to minimize the effect of TopFluor mediated interactions, we decided to use only 1:500 molar ratio of TopFluor-PI(4,5)P_2 in POPC GUVs. We also incorporated Rho-DOPE (1:500) and DOPE-Cap-biotin (1:10^6) in the lipid mixtures for imaging and immobilization purposes, respectively. DOPE-Cap-biotin was chosen as it should be homogeneously distributed in the POPC fluid phase.

Calcium (from a $CaCl_2$ stock solution) was added directly to the immobilized GUVs to achieve the desired concentrations. In this way, and as a result of the permeability barrier imposed by the lipid membrane, only TopFluor PI(4,5)P_2 molecules in the external leaflet of the vesicles might interact with Ca^{2+}. Since only small volumes of a stock solution of $CaCl_2$ with high concentration were added, no significant osmotic pressure changes occurred. Notice that in TopFluor-PI(4,5)P_2, the TopFluor fluorophore is conjugated with the acyl chain of PI(4,5)P_2 (figure 42). In this manner, we guarantee that the negative headgroup of the phosphoinositide remains available and unperturbed to freely establish interactions.

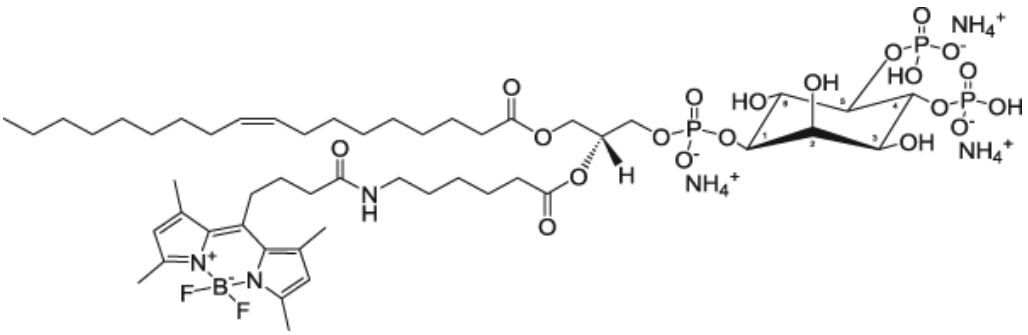

Figure 42. Structure of TopFluor-PI(4,5)P_2. PI(4,5)P_2 is labelled in an acyl chain with the fluorophore TopFluor.

Representative examples of the acquired images are presented in figure 43, with each vesicle imaged in the two channels.

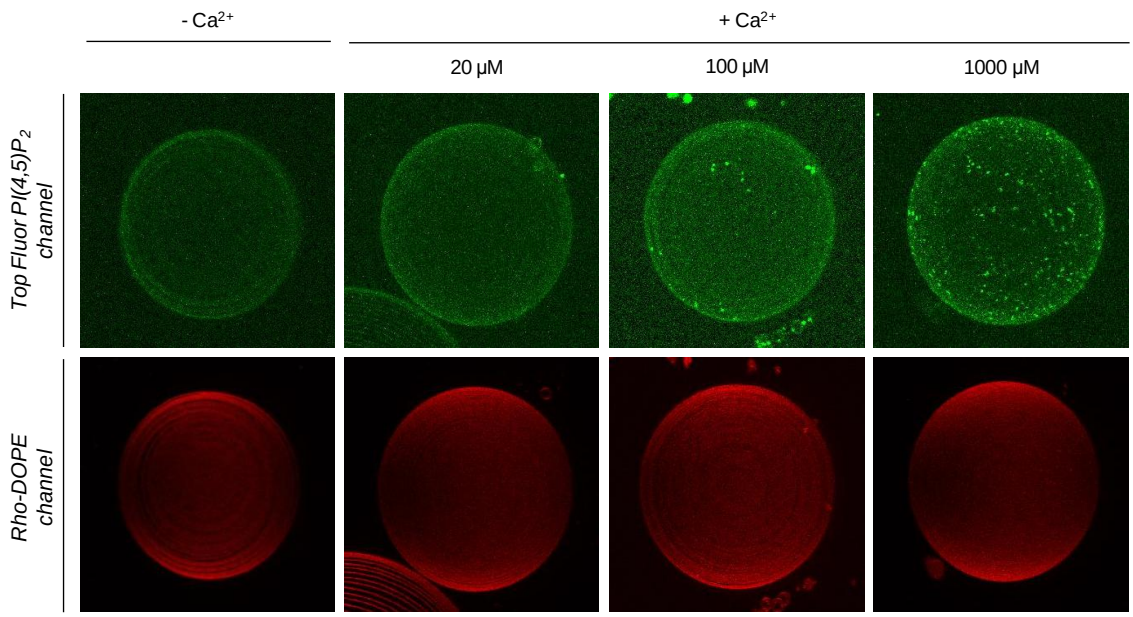

Figure 43. Representative examples of the two acquired images for each GUV, in the absence or presence of different calcium concentrations (0, 20, 100 and 1000 µM). TopFluor-PI(4,5)P_2 channel was measured by excitation at 488 nm and collecting fluorescence emission at 495-530 nm; Rho-DOPE channel measurements were performed by excitation at 514 nm and collection of fluorescence emission between 570 and 700.

From figure 43, we can see that when calcium concentration was increased, small clusters were observed in TopFluor-PI(4,5)P_2 channel images. Since these aggregates cannot be seen in Rho-DOPE images, we can rule out possible artifacts and attribute this effect uniquely to PI(4,5)P_2 clustering. Clustering of TopFluor-PI(4,5)P_2 induced by calcium is already clearly observed at 100 µM which is in the high end of the range of calcium concentrations expected to occur in the synaptic calcium nanodomains, i.e. the synaptic regions in the immediate vicinity of calcium channels (Naraghi and Neher, 1997;Parekh, 2008).

4. Conclusions and Perspectives

In an attempt to understand $PI(4,5)P_2$ distribution in the plasma membrane of cells and its relationship with the Ca^{2+}-mediated exocytosis in neurons, we focused on two distinct and complementary strategies. $PI(4,5)P_2$ organization in the plasma membrane and the effect of palmitoylation of synaptic proteins was studied in neuronal (PC12) and non-neuronal (HEK293) cell lines, while the influence of Ca^{2+} was assessed through experiments carried out in membrane model systems (GUVs).

By expressing PH-domains in HEK293 cells, we obtained FRET efficiencies that were independent from the concentration of acceptor (figure 20). This result suggests that there should be some organization of $PI(4,5)P_2$ molecules under the resolution of the microscope. When we inhibited protein palmitoylation with 2BP, differences in FRET efficiency were observed. Thus, even in non-neuronal cells, the interaction of $PI(4,5)P_2$ with palmitoylated proteins must play a role in its organization in the plasma membrane of the cells.

In PC12 cells, PH-domains fluorescence emission reported an heterogeneous distribution of $PI(4,5)P_2$. The acceptor fluorescence intensities were lower than the ones measured in HEK293 cells, but energy transfer was significantly more efficient. Thus, aggregates or high $PI(4,5)P_2$ density sites are clearly present in the plasma membrane of PC12 cells. However, the observed puncta did not present identical $PI(4,5)P_2$ density, since puncta with higher acceptor intensity presented a lower energy transfer efficiency.

The influence of protein palmitoylation in the distribution of SNAP-25 in PC12 cells was also studied. Incubating PC12 cells with 2BP, we were able to relocate part of the SNAP-25 molecules from the plasma membrane to the cytosol. However, due to the interaction of SNAP-25 with syntaxin-1, a high amount of SNAP-25 remained probably attached to the membrane. Since SNAP-25 was being overexpressed, there was probably not enough syntaxin-1 in the membrane to maintain SNAP-25 binding to the membrane, and consequently approximately around half of this protein remained outside the plasma membrane. Palmitoylation inhibition by 2BP can, in the future, be a powerful tool to study the effect of SNAP-25 palmitoylation in the distribution of $PI(4,5)P_2$ in the plasma membrane of PC12 cells.

In parallel, studies in membrane model systems, namely GUVs, were carried out. To obtain confocal data with high quality to report PI(4,5)P_2 distribution and to allow the use of single molecule techniques, complete immobilization of the vesicles during data acquisition is absolutely necessary. To achieve total immobilization, we optimized a method that makes use of biotinylated lipids and their interaction with an avidin-coated surface. Two different lipid mixtures were studied (POPC:Chol:PSM and DOPC:DPPC), since we aim to study PI(4,5)P_2 behaviour in these lipid environments. The used ternary lipid mixture presenting liquid ordered/liquid disordered phase coexistence has a special relevance, as the partition of PI(4,5)P_2 to cholesterol/sphingomyelin-enriched rafts was already reported (Tong et al., 2008).

The use of low concentrations of biotinylated lipid (1:10^6 molar ratio) does not affect GUVs shape, independently of the type of conjugated lipid or lipid mixture. When the concentration was increased, a high degree of deformation was often observed, as well as an increase in the collapse rates. It should be noticed that the electroformation method results in a highly heterogeneous population of vesicles, and it is essential that a significant population of GUVs is studied in order to observe any effect.

Imaging of GUVs over coverslips even in the absence of biotinylated lipid and avidin, induced a redistribution of lipid domains within the vesicles, with more organized lipid phases displaying more affinity for the coverslip surface. When the surface is coated with avidin, GUVs without biotinylated lipids presented instead a preference for the more disorganized lipid phase. Moreover, biotinylated lipids demonstrated different affinities for the lipid phases studied here, significantly affecting the distribution of lipid domains within the GUVs. Imaging only the top hemisphere (as it is often done) will then create a bias relatively to the total composition of the vesicles. Thus, to quantify lipid phase fractions in GUVs, it is absolutely essential to acquire data from the entire vesicle.

In POPC:Chol:PSM GUVs, DPPE-biotin was the biotinylated lipid that induced less deviations in composition between the two hemispheres. For this reason, it is probably the most appropriate biotinylated lipid to be used in studies for quantification of lo/ld phase fractions in mixtures displaying phase coexistance. However, it did induce a higher degree of vesicle collapse than the other biotinylated lipids, and the use of smaller concentrations of this lipid is advised.

From the literature, it is already established that high concentrations of calcium (1 mM) influence PI(4,5)P_2 distribution. However, its effect at physiologic concentrations is still unknown. In synapses, it is currently considered that after a stimulus, calcium

concentration in the immediate vicinity of Ca^{2+} channels (<100 nm) can increase until 100 μM (from the basal value of 100 nM). Using confocal fluorescence microscopy, we studied the effect of physiologic concentrations of this cation (20 and 100 μM) on the distribution of a fluorescently labelled $PI(4,5)P_2$ (TopFluor-$PI(4,5)P_2$). From the characterization of the behaviour of the labelled lipid in fluid membranes, it was possible to observe that, at low concentrations (<1%), TopFluor-$PI(4,5)P_2$ appeared to be freely-diffusing in a possibly monomeric form. When the concentration was increased, we observed some formation of probe complexes. These complexes should be a result of the presence of the TopFluor fluorophore, since they were not observed earlier using another fluorescent $PI(4,5)P_2$ conjugate. In the confocal fluorescence microscopy measurements, we used GUVs with a low concentration of the probe (1:500 molar ratio), in order to guarantee that we would be observing only interactions mediated by the inositol group of the PI. By analyzing the acquired confocal images, we detected the formation of large aggregates in presence of 100 μM and 1 mM of calcium. At lower concentrations, as well as in the absence of this cation, no large aggregates were observed. Nevertheless, the formation of smaller aggregates of $PI(4,5)P_2$ under the resolution of the microscope (<250 nm) might still occur. Future experiments are planned to better resolve the distribution of $PI(4,5)P_2$ molecules in this range of calcium concentrations, making use of more sensitive techniques, such as FCS.

Altogether, these results are important to the study of $PI(4,5)P_2$ function in the mechanism of exocytosis. After synaptic stimuli, the calcium influx at active zones is expected to lead to a massive reorganization of $PI(4,5)P_2$ distribution. Considering the multitude of proteins interacting specifically and non-specifically with this lipid, it is certain that such dramatic reorganization, as observed by us in membrane model systems, has the potential of not only changing charge and curvature at the plasma membrane, but also of restructuring much of the synaptic machinery. This would provide the cell with a lipidic calcium sensor in the regulation of neurotransmitter release and hormone secretion. However, it is unclear if $PI(4,5)P_2$ in active zones are free to interact with calcium ions or if they are mostly masked by protein interactions, and additional work must be carried out to fully resolve this issue.

5. References

Aoyagi,K., T.Sugaya, M.Umeda, S.Yamamoto, S.Terakawa, and M.Takahashi. 2005. The activation of exocytotic sites by the formation of phosphatidylinositol 4,5-bisphosphate microdomains at syntaxin clusters. *J Biol. Chem.* 280:17346-17352.

Balla,T. 2007. Imaging and manipulating phosphoinositides in living cells. *The Journal of physiology* 582:927-937.

Bergstrom,F., I.Mikhalyov, P.Hagglof, R.Wortmann, T.Ny, and L.B.A.Johansson. 2002. Dimers of dipyrrometheneboron difluoride (BODIPY) with light spectroscopic applications in chemistry and biology. *J. Am. Chem. Soc.* 124:196-204.

Berridge,M.J. 2009. Inositol trisphosphate and calcium signalling mechanisms. *Biochim. Biophys. Acta-Mol. Cell Res.* 1793:933-940.

Berridge,M.J. and R.F.Irvine. 1984. Inositol trisphosphate, a novel second messenger in cellular signal transduction. *Nature* 312:315-321.

Botelho,R.J., M.Teruel, R.Dierckman, R.Anderson, A.Wells, J.D.York, T.Meyer, and S.Grinstein. 2000. Localized biphasic changes in phosphatidylinositol-4,5-bisphosphate at sites of phagocytosis. *J Cell Biol.* 151:1353-1368.

Boucheny,C., G.P.Bonneau, J.Droulez, G.Thibault, and S.Ploix. 2009. A perceptive evaluation of volume rendering techniques. *ACM Trans. Appl. Percept.* 5.

Castanho,M., M.Prieto, and A.U.Acuna. 1996. The transverse location of the fluorescent probe trans-parinaric acid in lipid bilayers. *Biochim. Biophys. Acta-Biomembr.* 1279:164-168.

Chan,Y.H. and S.G.Boxer. 2007. Model membrane systems and their applications. *Curr. Opin. Chem. Biol.* 11:581-587.

Chen,H., H.L.Puhl, S.V.Koushik, S.S.Vogel, and S.R.Ikeda. 2006. Measurement of FRET efficiency and ratio of donor to acceptor concentration in living cells. *Biophys. J.* 91:L39-L41.

Chung,S.H., W.J.Song, J.Chen, R.W.Holz, K.Kim, G.D.Prestwich, and J.J.Bednarski. 1998. The C2 domains of Rabphilin3A specifically bind phosphatidylinositol 4,5-bisphosphate containing vesicles in a Ca2+-dependent manner. In vitro characteristics and possible significance. *J. Biol. Chem.* 273:10240-10248.

Clapham,D.E. 1995. Calcium signaling. *Cell* 131:1047-1058.

Cockcroft,S. and M.A.De Matteis. 2001. Inositol Lipids as Spatial Regulators of Membrane Traffic. *J. Membr. Biol.* 180:187-194.

Cremona,O., G.Di Paolo, M.R.Wenk, A.Luthi, W.T.Kim, K.Takei, L.Daniell, Y.Nemoto, S.B.Shears, R.A.Flavell, D.A.McCormick, and P.De Camilli. 1999. Essential role of phosphoinositide metabolism in synaptic vesicle recycling. *Cell* 99:179-188.

Czech,M.P. 2000. PIP2 and PIP3: complex roles at the cell surface. *Cell* 100:603-606.

Davenport,L., R.E.Dale, R.H.Bisby, and R.B.Cundall. 1985. Transverse Location of the Fluorescent-Probe 1,6-Diphenyl-1,3,5-Hexatriene in Model Lipid Bilayer-Membrane Systems by Resonance Excitation-Energy Transfer. *Biochemistry* 24:4097-4108.

de Almeida,R.F.M., J.Borst, A.Fedorov, M.Prieto, and A.J.W.G.Visser. 2007. Complexity of lipid domains and rafts in giant unilamellar vesicles revealed by combining imaging and microscopic and macroscopic time-resolved fluorescence. *Biophys. J.* 93:539-553.

de Almeida,R.F.M., A.Fedorov, and M.Prieto. 2003. Sphingomyelin/phosphatidylcholine/cholesterol phase diagram: Boundaries and composition of lipid rafts. *Biophys. J.* 85:2406-2416.

de Almeida,R.F.M., L.M.S.Loura, A.Fedorov, and M.Prieto. 2005. Lipid rafts have different sizes depending on membrane composition: A time-resolved fluorescence resonance energy transfer study. *J. Mol. Biol.* 346:1109-1120.

Draper,J.M. and C.D.Smith. 2009. Palmitoyl acyltransferase assays and inhibitors (Review). *Mol. Membr. Biol.* 26:5-13.

Dumas,F., R.D.Byrne, B.Vincent, T.M.C.Hobday, D.L.Poccia, and B.Larijani. 2010. Spatial regulation of membrane fusion controlled by modification of phosphoinositides. *PLoS ONE* 5:e12208.

Dun,A.R., C.Rickman, and R.R.Duncan. 2010. The t-SNARE complex: a close up. *Cell. Mol. Neurobiol.* 30:1321-1326.

Fasshauer,D., R.B.Sutton, A.T.Brunger, and R.Jahn. 1998. Conserved structural features of the synaptic fusion complex: SNARE proteins reclassified as Q- and R-SNAREs. *Proc. Natl. Acad. Sci. U. S. A.* 95:15781-15786.

Fernandes,F., L.M.S.Loura, A.Fedorov, and M.Prieto. 2006. Absence of clustering of phosphatidylinositol-(4,5)-bisphosphate in fluid phosphatidylcholine. *J. Lipid Res.* 47:1521-1525.

Ferrell,J.E. and W.H.Huestis. 1984. Phosphoinositide metabolism and the morphology of human-erythrocytes. *J. Cell Biol.* 98:1992-1998.

Ford,M.G., B.M.Pearse, M.K.Higgins, Y.Vallis, D.J.Owen, A.Gibson, C.R.Hopkins, P.R.Evans, and H.T.McMahon. 2001. Simultaneous binding of PtdIns(4,5)P2 and clathrin by AP180 in the nucleation of clathrin lattices on membranes. *Science (New York, N. Y.)* 291:1051-1055.

Fujita,K., P.Lazarovici, and G.Guroff. 1989. Regulation of the differentiation of PC12 pheochromocytoma cells. *Environ. Health Perspect.* 80:127-142.

Gamper,N. and M.S.Shapiro. 2007. Target-specific PIP2 signalling: how might it work? *J. Physiol. -London* 582:967-975.

Gauthier,T.D., E.C.Shane, W.F.Guerin, W.R.Seitz, and C.L.Grant. 1986. Fluorescence quenching method for determining equilibrium-constants for polycyclic aromatic-hydrocarbons Binding to Dissolved Humic Materials. *Environ. Sci. Technol.* 20:1162-1166.

Gonzalo,S. and M.E.Linder. 1998. SNAP-25 palmitoylation and plasma membrane targeting require a functional secretory pathway. *Mol. Biol. Cell* 9:585-597.

Greaves,J. and L.H.Chamberlain. 2007. Palmitoylation-dependent protein sorting. *J Cell Biol* 176:249-254.

Greene,L.A. and A.S.Tischler. 1976. Establishment of a noradrenergic clonal line of rat adrenal pheochromocytoma cells which respond to nerve growth factor. *Proc. Natl. Acad. Sci. U. S. A.* 73:2424-2428.

Greer,P.L. and M.E.Greenberg. 2008. From synapse to nucleus: calcium-dependent gene transcription in the control of synapse development and function. *Neuron* 59:846-860.

Halemani,N.D., I.Bethani, S.O.Rizzoli, and T.Lang. 2010. Structure and dynamics of a two-helix SNARE complex in live cells. *Traffic (Copenhagen, Denmark)* 11:394-404.

Halet,G. 2005. Imaging phosphoinositide dynamics using GFP-tagged protein domains. *Biol. Cell under the auspices of the European Cell Biology Organization* 97:501-518.

Haucke,V. 2005. Phosphoinositide regulation of clathrin-mediated endocytosis. *Biochem. Soc. Trans.* 33:1285-1289.

Hokin,L.E. and M.R.Hokin. 1958. Acetylcholine and the exchange of inositol and phosphate in brain phosphoinositide. *J. Biol. Chem.* 233:818-821.

Hokin,M.R. and L.E.Hokin. 1953. Enzyme secretion and the incorporation of P-82 into phospholipides of pancreas slices. *J. Biol. Chem.* 203:967-977.

Honda,A., M.Nogami, T.Yokozeki, M.Yamazaki, H.Nakamura, H.Watanabe, K.Kawamoto, K.Nakayama, A.J.Morris, M.A.Frohman, and Y.Kanaho. 1999. Phosphatidylinositol 4-phosphate 5-kinase alpha is a downstream effector of the small G protein ARF6 in membrane ruffle formation. *Cell* 99:521-532.

Hurley,J.H. and S.Misra. 2000. Signaling and subcellular targeting by membrane-binding domains. *Annu. Rev. Biophys.* 29:49-79.

James,D.J., C.Khodthong, J.A.Kowalchyk, and T.F.J.Martin. 2008. Phosphatidylinositol 4,5-bisphosphate regulates SNARE-dependent membrane fusion. *J Cell Biol.* 182:355-366.

Jennings,B.C., M.J.Nadolski, Y.P.Ling, M.B.Baker, M.L.Harrison, R.J.Deschenes, and M.E.Linder. 2009. 2-Bromopalmitate and 2-(2-hydroxy-5-nitro-benzylidene)-benzo[b]thiophen-3-one inhibit DHHC-mediated palmitoylation in vitro. *J. Lipid Res.* 50:233-242.

Jost,M., F.Simpson, J.M.Kavran, M.A.Lemmon, and S.L.Schmid. 1998. Phosphatidylinositol-4,5-bisphosphate is required for endocytic coated vesicle formation. *Curr. Biol.* 8:1399-1404.

Kahya,N. 2010. Protein-protein and protein-lipid interactions in domain-assembly: Lessons from giant unilamellar vesicles. *Biochim. Biophys. Acta-Biomembr.* 1798:1392-1398.

Korlach,J., P.Schwille, W.W.Webb, and G.W.Feigenson. 1999. Characterization of lipid bilayer phases by confocal microscopy and fluorescence correlation spectroscopy. *Proc. Natl. Acad. Sci. U. S. A.* 96:8461-8466.

Koticha,D.K., E.E.McCarthy, and G.Baldini. 2002. Plasma membrane targeting of SNAP-25 increases its local concentration and is necessary for SNARE complex formation and regulated exocytosis. *J. Cell Sci* 115:3341-3351.

Kucerka,N., S.Tristram-Nagle, and J.F.Nagle. 2005. Structure of fully hydrated fluid phase lipid bilayers with monounsaturated chains. *J. Membr. Biol.* 208:193-202.

Kwiatkowska,K. 2010. One lipid, multiple functions: how various pools of PI(4,5)P2 are created in the plasma membrane. *Cellular and molecular life sciences : CMLS*.

Lam,A.D., P.Tryoen-Toth, B.Tsai, N.Vitale, and E.L.Stuenkel. 2008. SNARE-catalyzed fusion events are regulated by Syntaxin1A-lipid interactions. *Mol. Biol. Cell* 19:485-497.

Lane,S.R. and Y.C.Liu. 1997. Characterization of the palmitoylation domain of SNAP-25. *J. Neurochem.* 69:1864-1869.

Lang,T., D.Bruns, D.Wenzel, D.Riedel, P.Holroyd, C.Thiele, and R.Jahn. 2001. SNAREs are concentrated in cholesterol-dependent clusters that define docking and fusion sites for exocytosis. *Embo J.* 20:2202-2213.

Lang,T. 2007. SNARE proteins and 'membrane rafts'. *The Journal of physiology* 585:693-698.

Lang,T., N.D.Halemani, and B.Rammner. 2008. Interplay between lipids and the proteinaceous membrane fusion machinery. *Prog. Lipid Res.* 47:461-469.

Laux,T., K.Fukami, M.Thelen, T.Golub, D.Frey, and P.Caroni. 2000. GAP43, MARCKS, and CAP23 modulate PI(4,5)P2 at plasmalemmal rafts, and regulate cell cortex actin dynamics through a common mechanism. *J. Cell Biol.* 149:1455-1471.

Lemmon,M.A. and K.M.Ferguson. 2000. Signal-dependent membrane targeting by pleckstrin homology (PH) domains. *Biochem. J.* 350 Pt 1:1-18.

Lemmon,M.A., K.M.Ferguson, and J.Schlessinger. 1996. PH domains: Diverse sequences with a common fold recruit signaling molecules to the cell surface. *Cell* 85:621-624.

Lemmon,M.A. 2003. Phosphoinositide recognition domains. *Traffic* 4:201-213.

Levental,I., D.A.Christian, Y.H.Wang, J.J.Madara, D.E.Discher, and P.A.Janmey. 2009. Calcium-dependent lateral organization in phosphatidylinositol 4,5-bisphosphate (PIP2)- and cholesterol-containing monolayers. *Biochemistry* 48:8241-8248.

Lin,R.C. and R.H.Scheller. 2000. Mechanisms of synaptic vesicle exocytosis. *Annu. Rev. Cell Dev. Biol.* 16:19-49.

Liscovitch,M., V.Chalifa, P.Pertile, C.S.Chen, and L.C.Cantley. 1994. Novel function of phosphatidylinositol 4,5-bisphosphate as a cofactor for brain membrane phospholipase-D. *J. Biol. Chem.* 269:21403-21406.

Logan,M. and C.Mandato. 2006. Regulation of the actin cytoskeleton by PIP2 in cytokinesis. *J. Cell Sci*.

Loose,M. and P.Schwille. 2009. Biomimetic membrane systems to study cellular organization. *Struct. Biol.* 168:143-151.

Marquardt,D.W. 1963. An algorithm for least-squares estimation of nonlinear parameters. *SIAM J.* 11:431-441.

Mateo,C.R., A.U.Acuna, and J.C.Brochon. 1995. Liquid-Crystalline Phases of Cholesterol Lipid Bilayers As Revealed by the Fluorescence of Trans-Parinaric Acid. *Biophys. J.* 68:978-987.

Mateo,C.R., J.C.Brochon, M.P.Lillo, and A.U.Acuna. 1993. Lipid clustering in bilayers detected by the fluorescence kinetics and anisotropy of trans-parinaric acid. *Biophys. J.* 65:2237-2247.

McLaughlin,S., J.Wang, A.Gambhir, and D.Murray. 2002. PIP(2) and proteins: interactions, organization, and information flow. *Annu. Rev. Biophys.* 31:151-175.

Morales-Penningston,N.F., J.Wu, E.R.Farkas, S.L.Goh, T.M.Konyakhina, J.Y.Zheng, W.W.Webb, and G.W.Feigenson. 2010. GUV preparation and imaging: minimizing artifacts. *BBA* 1798:1324-1332.

Murray,D.H. and L.K.Tamm. 2009. Clustering of syntaxin-1A in model membranes is modulated by phosphatidylinositol 4,5-bisphosphate and cholesterol. *Biochemistry* 48:4617-4625.

Nagai,T., K.Ibata, E.S.Park, M.Kubota, K.Mikoshiba, and A.Miyawaki. 2002. A variant of yellow fluorescent protein with fast and efficient maturation for cell-biological applications. *Nat. Biotechnol.* 20:87-90.

Naraghi,M. and E.Neher. 1997. Linearized buffered Ca2+ diffusion in microdomains and its implications for calculation of [Ca2+] at the month of a calcium channel. *JCR Abbrev. Title:* 17:6961-6973.

Neher,E. and T.Sakaba. 2008. Multiple roles of calcium ions in the regulation of neurotransmitter release. *Neuron* 59:861-872.

Nishio,M., K.I.Watanabe, J.Sasaki, C.Taya, S.Takasuga, R.Iizuka, T.Balla, M.Yamazaki, H.Watanabe, R.Itoh, S.Kuroda, Y.Horie, I.Forster, T.W.Mak, H.Yonekawa, J.M.Penninger, Y.Kanaho, A.Suzuki, and T.Sasaki. 2007. Control of cell polarity and motility by the PtdIns(3,4,5)P-3 phosphatase SHIP1. *Nat. Cell Biol.* 9:36-U40.

Pang,Z.P.P. and T.C.Sudhof. 2010. Cell biology of Ca(2+)-triggered exocytosis. *Curr. Opin. Cell Biol.* 22:496-505.

Parekh,A.B. 2008. Ca2+ microdomains near plasma membrane Ca2+ channels: impact on cell function. *J. Physiol. -London* 586:3043-3054.

Payrastre,B., K.Missy, S.Giuriato, S.Bodin, M.Plantavid, and M.Gratacap. 2001. Phosphoinositides: key players in cell signalling, in time and space. *Cell. Signal.* 13:377-387.

Peetla,C., A.Stine, and V.Labhasetwar. 2009. Biophysical interactions with model lipid membranes: applications in drug discovery and drug delivery. *Mol. Pharm.* 6:1264-1276.

Pietraszewska-Bogiel,A. and T.W.J.Gadella. 2010. FRET microscopy: from principle to routine technology in cell biology. *J. Microsc.* 241:111-118.

Pike,L.J. and L.Casey. 1996. Localization and turnover of phosphatidylinositol 4,5-bisphosphate in caveolin-enriched membrane domains. *J. Biol. Chem.* 271:26453-26456.

Pike,L.J. and J.M.Miller. 1998. Cholesterol depletion delocalizes phosphatidylinositol bisphosphate and inhibits hormone-stimulated phosphatidylinositol turnover. *J. Biol. Chem.* 273:22298-22304.

Pinto,S.N., L.C.Silva, R.F.M.de Almeida, and M.Prieto. 2008. Membrane domain formation, interdigitation, and morphological alterations induced by the very long chain asymmetric C24 : 1 ceramide. *Biophys. J.* 95:2867-2879.

Prescott,G.R., O.A.Gorleku, J.Greaves, and L.H.Chamberlain. 2009. Palmitoylation of the synaptic vesicle fusion machinery. *J. Neurochem.* 110:1135-1149.

Rauch,M.E., C.G.Ferguson, G.D.Prestwich, and D.S.Cafiso. 2002. Myristoylated alanine-rich C kinase substrate (MARCKS) sequesters spin-labeled phosphatidylinositol 4,5-bisphosphate in lipid bilayers. *J Biol. Chem.* 277:14068-14076.

Raucher,D., T.Stauffer, W.Chen, K.Shen, S.Guo, J.D.York, M.P.Sheetz, and T.Meyer. 2000. Phosphatidylinositol 4,5-bisphosphate functions as a second messenger that regulates cytoskeleton–plasma membrane adhesion. *Cell* 100:221-228.

Redfern,D.A. and A.Gericke. 2005. pH-Dependent domain formation in phosphatidylinositol polyphosphate/phosphatidylcholine mixed vesicles. *J. Lipid Res.* 46:504-515.

Rickman,C., C.N.Medine, A.R.Dun, D.J.Moulton, O.Mandula, N.D.Halemani, S.O.Rizzoli, L.H.Chamberlain, and R.R.Duncan. 2010. t-SNARE protein conformations patterned by the lipid microenvironment. *J. Biol. Chem.* 285:13535-13541.

Rizo,J. and C.Rosenmund. 2008. Synaptic vesicle fusion. *Nat. Struct. Mol. Biol.* 15:665-674.

Rizzo,M.A., G.H.Springer, B.Granada, and D.W.Piston. 2004. An improved cyan fluorescent protein variant useful for FRET. *Nat. Biotechnol.* 22:445-449.

Sackmann,E. 1996. Supported membranes: Scientific and practical applications. *Science* 271:43-48.

Schiavo,G., F.Benfenati, B.Poulain, O.Rossetto, P.Polverino de Laureto, B.R.DasGupta, and C.Montecucco. 1992. Tetanus and botulinum-B neurotoxins block neurotransmitter release by proteolytic cleavage of synaptobrevin. *Nature* 359:832-835.

Schmidt,M.L., L.Ziani, M.Boudreau, and J.H.Davis. 2009. Phase equilibria in DOPC/DPPC: Conversion from gel to subgel in two component mixtures. *J. Chem. Phys.* 131:175103-175114.

Sechi,A.S. and J.Wehland. 2000. The actin cytoskeleton and plasma membrane connection: PtdIns(4,5)P(2) influences cytoskeletal protein activity at the plasma membrane. *J. Cell Sci.* 113:3685-3695.

Shagin,D.A., E.V.Barsova, Y.G.Yanushevich, A.F.Fradkov, K.A.Lukyanov, Y.A.Labas, T.N.Semenova, J.A.Ugalde, A.Meyers, J.M.Nunez, E.A.Widder, S.A.Lukyanov, and M.V.Matz. 2004. GFP-like proteins as ubiquitous metazoan superfamily: evolution of functional features and structural complexity. *Mol. Biol. Evol.* 21:841-850.

Silva,L.C., R.F.M.de Almeida, B.M.Castro, A.Fedorov, and M.Prieto. 2007. Ceramide-domain formation and collapse in lipid rafts: Membrane reorganization by an apoptotic lipid. *Biophys. J.* 92:502-516.

Sklar,L.A., B.S.Hudson, M.Petersen, and J.Diamond. 1977. Conjugated polyene fatty-acids on fluorescent-probes - spectroscopic characterization. *Biochemistry* 16:813-819.

Sun,Y., H.Wallrabe, S.A.Seo, and A.Periasamy. 2011. FRET microscopy in 2010: the legacy of Theodor Forster on the 100th anniversary of his birth. *ChemPhysChem* 12:462-474.

Sutton,R.B., D.Fasshauer, R.Jahn, and A.T.Brunger. 1998. Crystal structure of a SNARE complex involved in synaptic exocytosis at 2.4 A resolution. *Nature* 395:347-353.

Toker,A. 1998. The synthesis and cellular roles of phosphatidylinositol 4,5-bisphosphate. *Curr. Opin. Cell Biol.* 10:254-261.

Toner,M., G.Vaio, A.Mclaughlin, and S.Mclaughlin. 1988. Adsorption of cations to phosphatidylinositol 4,5-bisphosphate. *Biochemistry* 27:7435-7443.

Tong,J., L.Nguyen, A.Vidal, S.A.Simon, J.H.P.Skene, and T.J.McIntosh. 2008. Role of GAP-43 in sequestering phosphatidylinositol 4,5-bisphosphate to raft bilayers. *Biophys. J.* 94:125-133.

Truong,K. and M.Ikura. 2001. The use of FRET imaging microscopy to detect protein–protein interactions and protein conformational changes in vivo. *Curr. Opin. Struct. Biol.* 11:573-578.

van Paridon,P.A., B.de Kruijff, R.Ouwerkerk, and K.W.Wirtz. 1986. Polyphosphoinositides undergo charge neutralization in the physiological pH range: a 31P-NMR study. *BBA* 877:216-219.

Vancha,A.R., S.Govindaraju, K.V.L.Parsa, M.Jasti, M.González-García, and R.P.Ballestero. 2004. Use of polyethyleneimine polymer in cell culture as attachment factor and lipofection enhancer. *BMC Biotechnol.* 4:23-35.

Vogel,K., J.P.Cabaniols, and P.A.Roche. 2000. Targeting of SNAP-25 to membranes is mediated by its association with the target SNARE syntaxin. *J. Biol. Chem.* 275:2959-2965.

Vogel,S.S., C.Thaler, and S.V.Koushik. 2006. Fanciful FRET. *Science's STKE : signal transduction knowledge environment* 2006:re2.

Wagner,M.L. and L.K.Tamm. 2000. Tethered polymer-supported planar lipid bilayers for reconstitution of integral membrane proteins: Silane-polyethyleneglycol-lipid as a cushion and covalent linker. *Biophys. J.* 79:1400-1414.

Walde,P., K.Cosentino, H.Engel, and P.Stano. 2010. Giant vesicles: preparations and applications. *Chembiochem* 11:848-865.

Wallrabe,H. and A.Periasamy. 2005. Imaging protein molecules using FRET and FLIM microscopy. *Curr. Opin. Biotechnol.* 16:19-27.

Wang,J., A.Arbuzova, G.Hangyás-Mihályné, and S.Mclaughlin. 2001. The effector domain of myristoylated alanine-rich C kinase substrate binds strongly to phosphatidylinositol 4,5-bisphosphate. *J Biol. Chem.* 276:5012-5019.

Webb,Y., L.Hermida-Matsumoto, and M.D.Resh. 2000. Inhibition of protein palmitoylation, raft localization, and T cell signaling by 2-bromopalmitate and polyunsaturated fatty acids. *J. Biol. Chem.* 275:261-270.

Weber,T., B.V.Zemelman, J.A.Mcnew, B.Westermann, M.Gmachl, F.Parlati, T.H.Sollner, and J.E.Rothman. 1998. SNAREpins: Minimal machinery for membrane fusion. *Cell* 92:759-772.

Westerink,R.H.S. and a.G.Ewing. 2008. The PC12 cell as model for neurosecretion. *Acta Physiol.* 192:273-285.

Zal,T. and N.R.J.Gascoigne. 2004. Photobleaching-corrected FRET efficiency imaging of live cells. *Biophys. J.* 86:3923-3939.

Zhang,H.L., L.C.Craciun, T.Mirshahi, T.Rohacs, C.M.B.Lopes, T.H.Jin, and D.E.Logothetis. 2003. PIP2 activates KCNQ channels, and its hydrolysis underlies receptor-mediated inhibition of M currents. *Neuron* 37:963-975.